The Pennsylvania State University

The Graduate School

MODELING OF SMALL SCALE RADIO-FREQUENCY INDUCTIVE DISCHARGES FOR ELECTRIC PROPULSION APPLICATIONS

A Dissertation in

Electrical Engineering

by

Valérie F. M. Mistoco

Submitted in Partial Fulfillment

of the Requirements

for the Degree of

Doctor of Philosophy

August 2011

The dissertation of Valérie F. M. Mistoco was reviewed and approved* by the following:

Sven G. Bilén
Associate Professor of Engineering Design, Electrical Engineering, and Aerospace Engineering
Dissertation Advisor, Chair of Committee

Victor Pasko
Professor of Electrical Engineering

Stewart K. Kurtz
Professor Emeritus of Electrical Engineering

Michael M. Micci
Professor of Aerospace Engineering

Kultegin Aydin
Professor of Electrical Engineering
Interim Department Head of Electrical Engineering

*Signatures are on file in the Graduate School.

Abstract

This work is motivated by the increasing interest in small-scale radio-frequency ion thrusters for micro- and nanosatellite applications, in particular for station-keeping. This specific type of thruster relies on an inductive discharge to produce positive ions that are accelerated by an external electric field in order to produce thrust. Analyzing the particle dynamics within the discharge vessel is critical for determining the performance of these thrusters, particularly as scaling down the size and thrust level of ion thrusters remains a major challenge. Until now the application of this type of propulsion system has been limited to large satellites and space platforms.

The approach taken in this work was, first, to perform a simple analysis of the inductive discharge using a transformer model. However, the dimensions of the thruster and the pressure ranges at which it operates called for a different approach than those used in larger thrusters and reactors as the collisional domain and non-locality effects differ significantly. After estimating the non-locality effects by calculating the non-locality parameter, a kinetic description of the discharge was developed. From the input power, mass flow rate, and the properties of the gas used in the discharge, the density numbers, temperatures of the particles, and thrust are calculated. Simulation values are compared with experimental values obtained with the Miniature Radio-frequency Ion Thruster being developed at The Pennsylvania State University.

The approach employed to model this small scale inductive discharge can be summarized as follows. First, conditions of operation and the various plasma parameters of the discharge were derived. Then, a one-dimensional kinetic model of an inductive discharge, using a Maxwellian electron distribution, was built. Results from this model were validated on data available in the literature. Finally, from the beam current derived from the 1-D model, using a two-grid ion optics

configuration, thrust was calculated.

In addition, an existing model of transition between capacitive and inductive modes was applied to the Miniature Radio-frequency Ion Thruster geometry and its electrical properties. A description of the different types of capacitively coupled radio-frequency initiation mechanisms is also given.

Table of Contents

List of Figures

List of Tables

List of Symbols

a radius (m)

a acceleration (m/s^2)

A area (m^2); A, oscillation amplitude; A_{eff} effective area for particle loss (m^2)

c velocity of light in vacuum (3×10^8 m/s)

e unsigned charge of an electron (1.602×10^{-19} C)

E electric field (V/m)

$\mathcal{E}$ voltage equivalent of energy (V), i.e., energy (J) = $e\mathcal{E}$ (V); $\mathcal{E}_T$, total energy lost per electron–ion pair created (V); $\mathcal{E}_i$, ion kinetic energy lost at a surface (V); $\mathcal{E}_e$, mean kinetic energy lost per electron lost (V)

f frequency (Hz); distribution function ($m^{-6}s^3$); f_m, Maxwellian distribution; f_{pe}, electron plasma frequency (Hz); f_{pi}, ion plasma frequency (Hz)

f_c collisional force per unit volume (N/m^3)

F force (N)

h center-to-edge ratio; h_l, axial ratio; h_R, radial ratio; height (m)

H magnetic field (A/m)

I electrical current (A); differential scattering cross section (m^2/Sr)

j $\sqrt{-1}$

J electrical current density (A/m^2)

J Bessel function of the first kind

K electron loss rate constant ($m^3 \cdot s^{-1}$); K_{iz}, ionization electron loss rate constant ($m^3 \cdot s^{-1}$); K_{ex}, excitation electron loss rate constant ($m^3 \cdot s^{-1}$); K_m, elastic electron loss rate constant ($m^3 \cdot s^{-1}$)

k Boltzmann's constant (1.3807×10^{-23} J/K); wave number or wave vector (m^{-1})

l discharge length (m); antenna length (m)

L inductance (H)

m mass (m); m_e, electron mass (9.11×10^{-31} kg)

M ion mass (kg)

n particle density (m^{-3}); n_i, ion density (m^{-3}); n_e, electron density (m^{-3}); n_g, neutral gas density (m^{-3}); n_s, sheath density (m^{-3})

$\mathcal{N}$ number of turns of coil

p pressure (N/m^2)

P power (W)

q electric charge (C)

r radial position (m)

R cylinder radius (m); R_0, gas constant ($8.314\ J \cdot K^{-1} \cdot mol^{-1}$); R_p, plasma resistance (Ω)

$\overline{S}$ time average power flux (W/m^2); $\overline{S}_{\text{stoc}}$, time-average stochastic power flux (W/m^2)

s sheath thickness (m)

t time (s)

T temperature (K); T_0, standard temperature (298 K); T_r, temperature ratio

T temperature in units of electron volts (eV)

u average velocity (m/s); u_e, electron average velocity (m/s); u_i, ion average velocity(m/s); u_B, Bohm velocity (m/s)

v velocity (m/s); $\overline{v}$, average speed; v_{th}, thermal velocity (m/s); v_R, relative velocity (m/s); v_{ph}, phase velocity (m/s)

V volume (m^3)

x rectangular coordinate (m)

X reactance (Ω)

y rectangular coordinate (m)

Y admittance (S)

z rectangular or axial cylindrical coordinate (m)

Z relative charge of an ion; impedance (Ω); $Z(\xi)$, plasma dielectric function; $Z_{s,l}^{\text{gen}}(\xi)$, generalized plasma dielectric function

α spatial rate of variation (m^{-1}); spatial attenuation of decay constant (m^{-1}); first Townsend coefficient (m^{-1}); thrust correction factor

γ_{se} secondary electron emission coefficient

Γ Gamma function

δ Dirac delta function; layer thickness (m); δ_p, collisionless skin depth (m); δ_c, collisional skin depth (m); δ_e, anomalous skin depth (m)

ϵ dielectric constant (F/m); ϵ_0, vacuum permittivity (8.854×10^{-12} F/m); ϵ_p, plasma dielectric constant (F/m)

ζ_L fractional energy loss for elastic collision

θ angle (rad)

κ relative dielectric constant; κ_p, relative plasma dielectric constant; κ_T, relative thermal conductivity

λ mean free path (m); λ_c, collisional mean free path (m); λ_e, electron mean free path (m); λ_i, ion mean free path (m); λ_{De}, Debye length (m); λ_E electron energy relaxation length (m)

μ mobility ($\text{m}^2/\text{V}\cdot\text{s}$); μ_0, vacuum permeability ($4\pi \times 10^{-7}$ H/m)

ν collision or interaction frequency (s^{-1} or Hz); ν_c, collision frequency (s^{-1} or Hz); ν_{iz}, ionization collision frequency (s^{-1} or Hz); ν_m, elastic collision frequency (s^{-1} or Hz); ν_{ex}, excitation collision frequency (s^{-1} or Hz)

π 3.14159265...

ρ volume charge density (C/m^3); ρ_S, surface charge density (C/m^2)

σ cross section (m^2); σ_{rf}, rf electrical conductivity ($\Omega^{-1} \cdot m^{-1}$)

τ mean free time (s); τ_c, collision time (s)

Φ angle (rad); spherical azimuthal angle (rad); electric potential (V); Φ_p, plasma potential (V); Φ_w, wall potential (V)

ϕ magnetic flux ($T \cdot m^2$)

ω radian frequency (rad/s); ω_{pe}, electron plasma frequency (rad/s)

∇, ∇_r vector spatial derivative; ∇_v, vector velocity derivative

Acknowledgments

I would like to express my sincere gratitude to my advisor, Dr. Sven Bilén, for his constant support and encouragement. Thank you specially for your patience and standing by me as I was certainly not the traditional graduate student. I would like to thank my committee members Drs. Kurtz, Micci, and Pasko for their advice and critical review of my research. Thank you Dr. Kurtz for your help during the initial experimental part of my work. Your inputs, support, critical questioning were invaluable to me.

Thank you to Dr. Vladimir Getman for his help and support setting up the experimental apparatus and, in particular, for sharing some his knowledge of vacuum systems with me.

I would also like to thank Prof. Anthony Ferraro for his help with the theoretical as well as experimental part of my project.

Thank you to my former fellow LionSat student members, Brendan Surrusco, Erica Mendoza, and Rob Siegel, only mentioning a few.

Thank you to the Electrical Engineering secretary office, especially to MaryAnn Henderson, and SherryDawn Jackson.

My fellow Penn State grad students Azin Neishaboori, Eftihia Vlahos, Ymène Fouli, Sophia Vlahos, Brian Zellers, Benoît Petitjean, made the adventure all more bearable, especially with the coffee breaks. Thank you all.

I would like to thank my husband Keith Josten for his unconditional patience, understanding, support and love. Thank you for making time for me to work on this thesis and for being always there for me, picking me up when I needed to be and keeping me in touch with reality at times.

A special thank you to my family, especially my mom, Alice Mistoco, who has always been by my side; my aunts, Anne-Marie, Marianne, Line, and Gladys; my uncles Philippe M. and Philippe B.; and my grand-mother Sophie. Merci à vous

tous pour votre soutien, vos encouragements et le fait de toujours croire en moi, même dans mes moments de doute.

Thank you to my in-laws Norbert and Nona Josten and to the entire Josten clan. Thank you as well to Lisa, Tony, and Daniele Demunda for being such great neighbors and countless hours of free baby-sitting.

I would like to thank AFOSR for funding in part from grant F49620-03-0137, the donors to the Student Space Programs Laboratory, and the EE Department for granting me teaching assistantships.

Dedication

To my husband Keith Josten and our children, Simon, Sophie, and William.
To my mother Alice Mistoco.
To the memory of my grand-father Marie-Émile Mistoco (Papa Tav) and my grand-mother Marie-Eugénie (Sophie) Mistoco.

It is not the critic who counts; not the man who points out how the strong man stumbles, or where the doer of deeds could have done them better. The credit belongs to the man who is actually in the arena, whose face is marred by dust and sweat and blood, who strives valiantly; who errs and comes short again and again; because there is not effort without error and shortcomings; but who does actually strive to do the deed; who knows the great enthusiasm, the great devotion, who spends himself in a worthy cause, who at the best knows in the end the triumph of high achievement and who at the worst, if he fails, at least he fails while daring greatly. So that his place shall never be with those cold and timid souls who know neither victory nor defeat.

—Theodore Roosevelt

Chapter 1

Research Description

1.1 Objectives

This work analyzes the electrical properties of a small scale, radio-frequency, cylindrical, inductively coupled plasma (ICP) discharge and presents a model for a miniature rf ion thruster (MRIT). The MRIT is taken as a practical application and its dimensions and shape are used for validation of this research.

The objectives are to obtain a detailed description of the discharge within a minituarized ICP discharge. This description includes models of the plasma inside the discharge chamber for different collisional regimes. For its application to propulsion systems, this work also examines the thrust-to-input-power ratio in order to evaluate the influence that reduction in size has on thruster performance.

1.2 Motivation

Scaling down the size and thrust level of ion thrusters remains a major challenge for the electric propulsion field. One of the practical applications of these miniature

devices is for station-keeping of small satellites with a total mass on the order of a few to tens of kilograms. The increasing demand from the small satellite community for reliable, small-scale attitude control devices also motivates this research [2, 3].

1.3 Contributions

This work models the plasma behavior within a miniature rf ion thruster (MRIT) for different pressure ranges and, therefore, collisional domains. Research on ICPs was first focused on large-scale cylindrical geometries. Because of the industrial applications, particularly in the semiconductor processing industry, focus shifted towards flat ICPs, progressively increasing the scale of study. New interest was shown towards smaller scale cylindrical ICPs (below 10-cm radii) for satellite propulsion applications [1]. However, these efforts have so far been confined to experimental studies and a gap exists in the study of smaller scale cylindrical ICPs. This work contributes to the knowledge of this latter type of discharge, in particular for its potential application in satellite propulsion systems.

The specific contributions of this dissertation are as follows:

- An analysis of the initiation of the discharge as well as a study of the transition between the capacitive and inductive modes of the discharge;
- Results from a plasma transformer model provide direction for experimental studies, in particular the design of a matching network to sustain the discharge;
- Establishment of the different collisional modes found in a small-scale cylindrical ICP;

- A non-local 1-D kinetic model of a miniature rf inductive discharge;
- For its applications to satellite propulsion, thrust calculations validated by experimental results and empirical estimates (for the smallest scale considered). This model offers a reliable platform to determine the potential thrust output of small scale rf thrusters.

Figure 1.1 provides a general overview of the model developed in this work as well as the location of each element within the thesis. From the given inputs (geometry, gas properties, rf power, etc.), we first derive several electrical properties of the inductive discharge such as mean free path and electron temperature. The knowledge of these entities allows the determination of the collisional regimes encountered by the MRIT (detailed in Sections 3.3.1 and 5.1.3). It is shown that this small scale discharge falls within the three possible collisional domains depending on the pressure of operation. However, the main domain of operation remains the collisionless domain. After calculation of the non-locality parameter, Λ, a non-local kinetic approach was chosen as explained in Section 2.3.3.4. From the results of the kinetic model, thrust calculations were performed for the application to satellite propulsion. This model is the most important contribution of this work.

In parallel, a transformer model was developed, which provides guidance in the design of a matching network to support the discharge. Also, a simple model of the plasma initiation was derived as well as an analysis of the transition between capacitive (E) and inductive (H) modes and vice versa.

1.4 Dissertation Overview

The remainder of the dissertation is organized as follows:

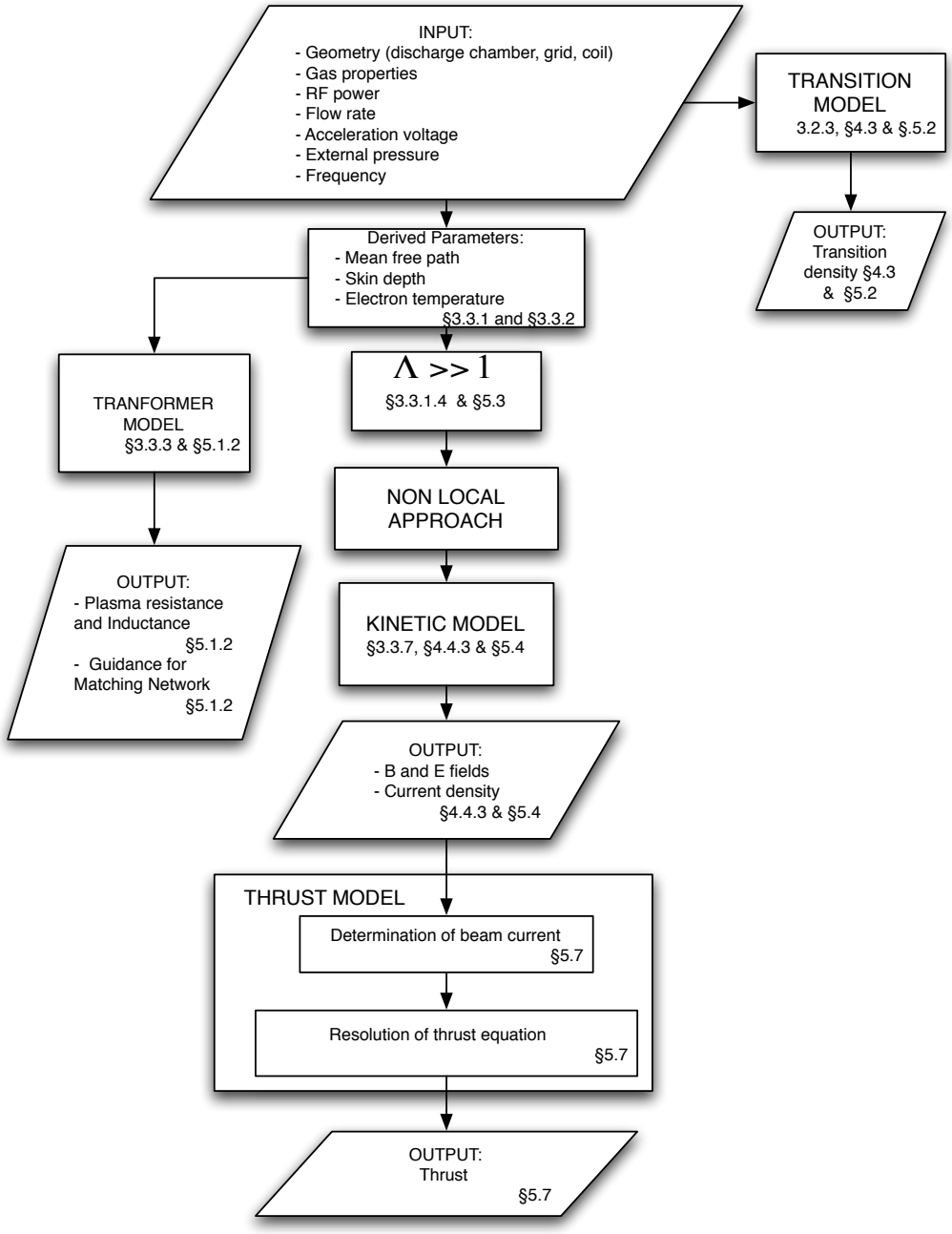

Figure 1.1. Diagram of the computational models developed in this work and where they are discussed in this dissertation.

- Chapter 2 presents the approach, giving an assessment of the background and technical needs as well as a description of the tools used;
- Chapter 3 describes the various physical phenomena occurring within the ionization chamber—including an analysis of the different collisional regimes possibly encountered—as well as the thrust production process;
- Chapter 4 provides the different collisional regimes seen by the MRIT, the types of initiation possible, as well as a validation of the transition and kinetic models using published data;
- In Chapter 5, the various submodels (transformer model, transition model, kinetic model) are applied to the MRIT geometry and thrust is derived, the results are presented as well as a comparisons with experimental data and discussion of those results; and
- Chapter 6 concludes and presents some recommendations for future work.

Chapter 2

Approach to the Study of Small Scale Radio-Frequency Inductive Discharges for Electric Propulsion Applications

This chapter presents the approach taken to study small scale inductive discharges, giving an assessment of the background and technical needs as well as a description of the numerical and experimental studies.

2.1 General Background

This section outlines some essential notions of propulsion systems and plasma physics necessary for the general understanding of this work. It presents as well a state-of-the-art review of electric propulsion systems to situate the rf ion thruster. The review of numerical simulations and studies done on radio frequency inductive

discharges grounds our work and explains the general approach taken here.

2.1.1 Some Principles of Rocket Propulsion

2.1.1.1 Definition and description of thrust and I_{sp}

Thrust is the forward-directed force developed on a rocket engine as a result of the rearward propellant mass ejected from it. It is equal to the opposite of the time rate of change of the momentum of the propellant and is given by the product of the exhaust velocity of the propellant by the time rate of change of the propellant mass, i.e.,

$$T = -\dot{m}u_e, \tag{2.1}$$

where $\dot{m}$ is the mass flow rate of the propellant and u_e is the exhaust velocity relative to the rocket. The ejection of an increment Δm of mass from the rocket leads to an increment Δv of the velocity given by

$$\Delta v = u_e \ln \frac{m_0}{m_0 - \Delta m}, \tag{2.2}$$

where m_0 is the initial mass of the rocket. The specific impulse is defined as the ratio of the thrust to the consumption rate of propellant at sea level, i.e.,

$$I_{\text{sp}} = \frac{\dot{m}u_e}{\dot{m}g_0}, \tag{2.3}$$

where g_0 is Earth's gravitational acceleration [9]. Higher I_{sp} means more efficient thrusters and higher exhaust velocities improve the I_{sp}.

2.1.1.2 Limitations to attainable chemical propulsion exhaust velocity

Exhaust velocities attainable by traditional chemical rockets are limited by the intrinsic energy carried within the propellants. Different types of propellants have different intrinsic energies and different thuster designs utilize these propellants at different efficiencies. Therefore, they yield different values for the exhaust velocity. Exhaust velocities for few types of propellants are given in Table 2.1.

Table 2.1. Exhaust velocities of different propellants [10].

Propellant Type	**Exhaust Velocity ($\mathbf{m \cdot s^{-1}}$)**
Liquid monopropellant	1700–2900
Solid propellant	2100–3200
Liquid bipropellant	2900–4500

The main losses in propulsion systems that result in limited exhaust velocities are

1. Heat loss to chamber walls, the rate of which is determined by the material used in the combustion chamber and the nozzle. The material has to withstand the thermal stresses generated during the thruster operation.

2. Some energy deposition in the gas that is unrecoverable since it is deposited in internal modes of the gas, as in the case of frozen flow losses and radiation losses from the exhaust jet [9].

3. Radiation.

All of these processes absorb energy, which reduces exhaust velocity.

2.1.2 Electric Propulsion

2.1.2.1 History

The first informal expression of electric propulsion (EP) was made by Goddard in 1906 as recorded in his notebook. Figure 2.1 shows an excerpt of his first handwritten thoughts on the subject.

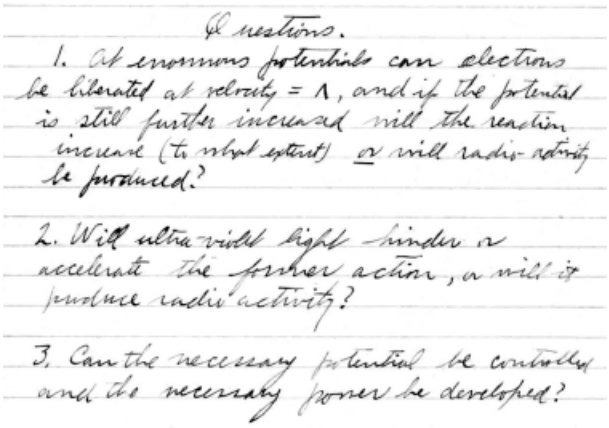
Questions.
1. At enormous potentials can electrons be liberated at velocity = 1, and if the potential is still further increased will the reaction increase (to what extent) or will radio-activity be produced?
2. Will ultra-violet light hinder or accelerate the former action, or will it produce radio activity?
3. Can the necessary potential be controlled and the necessary power be developed?

Figure 2.1. Excerpt of the entry dated September 6, 1906 in Goddard's notebook where he ponders the feasibility of electric propulsion through qualitative questions [11].

Another informal expression of the concept is to be found in the last chapter of Oberths' book *Wege zur Raumschiffahrt* (Ways to Spaceflight) published in 1929. In this chapter titled "*Das elektrische Raumschiff*" ("The Electric Spaceship"), Oberths specifically discussed spacecraft power and EP, predicting its future role in propulsion and attitude control outside the atmosphere [11]. However, research on EP devices remained limited for many years. In 1948, the first feasibility study on integrated spacecraft employing EP was conducted. Ernst Stuhlinger later performed a series of surveys on the use of EP for spacecraft. In the late 1950s, actual experiments involving EP devices started on a small scale in a few government laboratories. These experiments involved the application of thermal arcjets for

propulsion systems, experiments on ion production, beam neutralization studies, electrode design, and construction of small ion thrusters [9].

Later came electromagnetic acceleration experiments derived from T-tubes, button guns, and laboratory-scale plasma generators [6]. In 1958, the lengthy study of magnetohydrodynamic channel flow was applied to the design of propulsion devices [9]. These different efforts resulted in the development of several models of each class of thruster in the 1960s. July 20, 1964 saw the first successful test of an electric thruster in space during a 25-min ballistic flight [9].

2.1.2.2 Chemical vs. electric propulsion

EP devices are of particular interest for a number of different reasons. Worldwide research on a variety of EP devices has shown their advantages over chemical thrusters for various applications. For example, the high specific impulse of EP systems makes them highly desirable for north–south station keeping (NSSK) applications since they provide a valuable increase in propellant efficiency for satellites on which mass is limited. The specific impulse of a typical chemical thruster is on the order of 300 s, whereas ion thrusters can achieve specific impulses on the order of 3000 s or higher [3]. In particular, radio-frequency thrusters, on which research began in the 1960s, have demonstrated several additional benefits including the ability to trade thrust for I_{sp}, operate without a hot cathode, and ionize the propellant using electromagnetic fields. Table 2.2 gives examples of typical specific impulses for different types of thrusters.

2.1.2.3 Classical challenges of EP

The available electric power that was once a limiting factor in the use of ion thrusters onboard spacecraft is now less of an issue. Solar cells with higher per-

Table 2.2. Typical specific impulse and propellants of chemical and electric thrusters with flight heritage [12].

Thruster Types	**Specific Impulse (I_{sp})**	**Propellant**
Cold Gas	50–75	various
Chemical (monopropellant)	150–225	N_2H_4 H_2O_2
Chemical (bipropellant)	300–450	various
Resistojet	300	N_2H_4 monopropellant
Arcjet	500–600	N_2H_4 monopropellant
Ion Truster	2500–3600	xenon
Hall Thruster	1500–2000	xenon
Pulsed Plasma Thruster	850–1200	Teflon

formance can provide more power necessary for the ionization and acceleration processes and, thus, have revived interest in ion propulsion for space applications.

2.1.3 Radio-Frequency Inductive Discharges

2.1.3.1 Radio-frequency ion thruster history

The first rf inductive discharge recorded was in 1884, when Hittorf wrapped a coil, excited with a Leyden Jar, around an evacuated tube. The validity of this experiment was recognized after 50 years of controversy. The first ion sources were later developed in the 1940s by Getting *et al.* and Thonemann *et al.* In the 1950s, rf sources were widely used in Van-der-Graf generators, Cockcrofts–Walton accelerators, and Newton generators due to their high proton content, simplicity of construction, long life, etc.

In the 1960s, the first rf ion thruster was designed: a 10-cm diameter rf ion thruster, called the RIT-10, running at an ionization frequency of 1 MHz with a cylindrical ionization vessel using mercury for the propellant. It was developed and tested at Giessen University, Germany. A picture of this thruster is shown in

Figure 2.2.

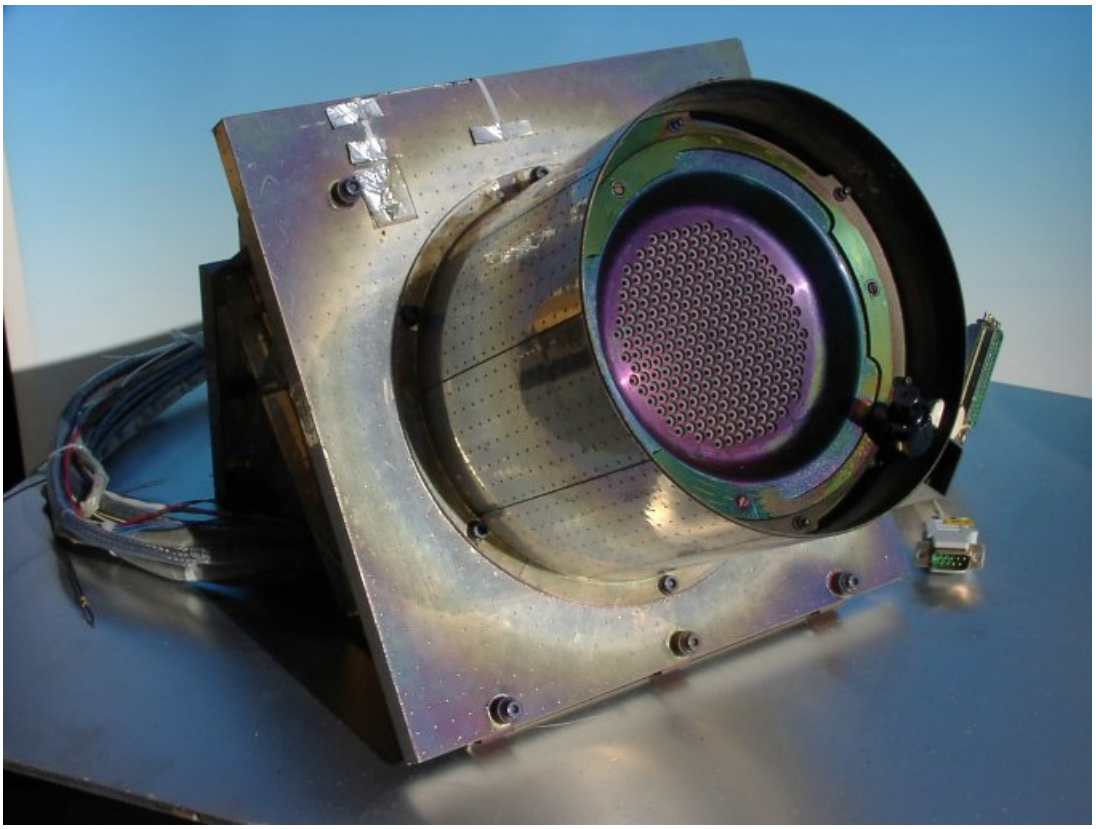

Figure 2.2. Picture of the RIT-10 [13].

This rf-ion device differentiated itself from other EP devices in the manner in which the propellant ionization was achieved. An ionization chamber, made of a dielectric material, was surrounded by an rf coil through which rf power was provided. An rf electric field was induced across the coil, which sustained the plasma discharge in the chamber. All rf ion thrusters subsequently designed followed these basic design principles.

In general, the functioning of an rf ion thruster can be subdivided into two main processes: first, ionization of the propellant and, second, acceleration of the ionized propellant using electrostatic forces through exit grids. These two

steps, being independent in nature, allow the beam velocity to be controlled by varying the grid voltage. Further description of the ionization process is provided in Chapter 3. General schematics of the RIT series model are shown in Figure 2.3.

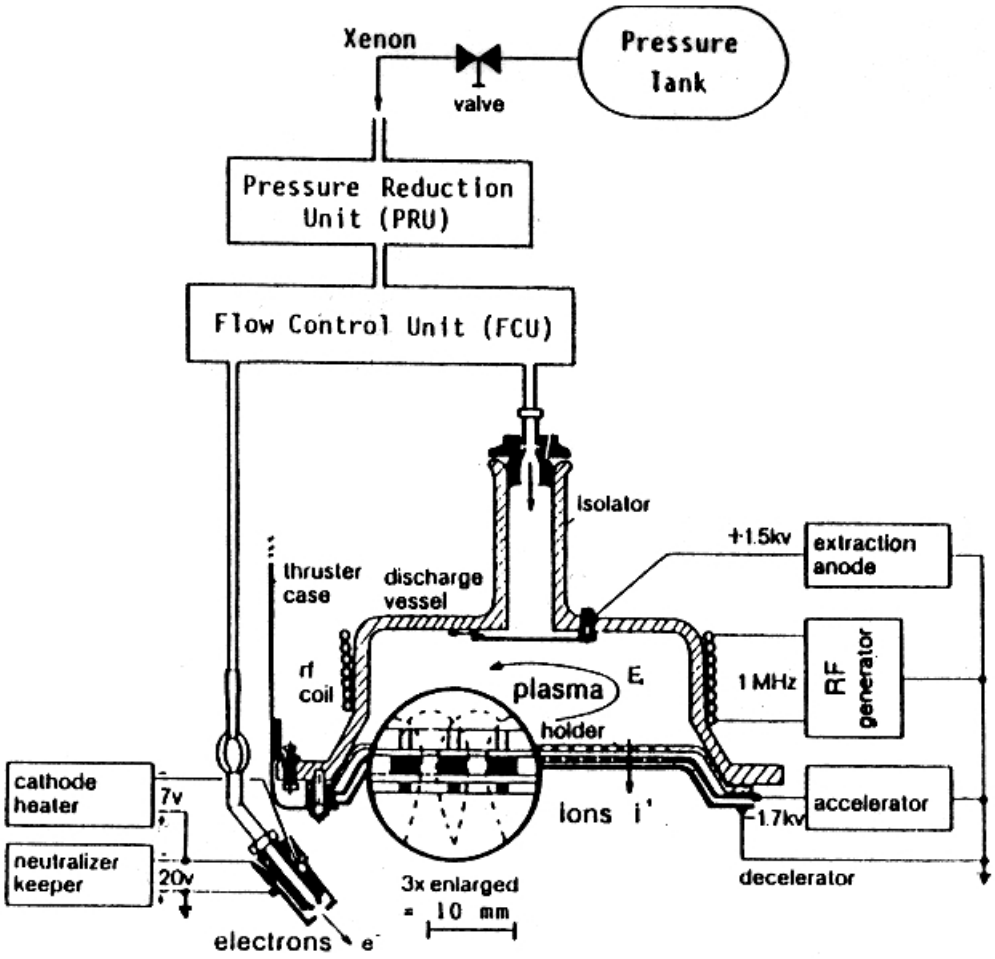

Figure 2.3. RIT schematics [14].

The RIT-10 research focused on the performance of this thruster at different power levels, which were set to produce different specific impulses. The initial version of the RIT-10 was adapted to replace the mercury propellant with xenon gas. The adapted version was tested onboard the retrievable carrier *Eureca* that was launched in 1992. It was designed to operate at an altitude of approximately

500 km for a one-year mission with a thrust varying between 5 and 10 mN. Post-recovery inspection of the system revealed that the thruster worked for about 240 of the 1000 hours for which it was designed. The shortened life was apparently due to a failure of a soldering connection [15]. The power-to-thrust ratio achieved was between 25 to 30 W/mN at specific impulses varying from 3000 to 4000 s.

2.1.3.2 Scaling up of rf ion thrusters

In an effort to scale up the RIT-10, the RIT-15 and RIT-35 were successively developed with diameters of 15 and 35 cm, respectively. The thrust delivered by these thrusters was on the order of 20 and 250 mN, respectively [16]. The operational frequency of the RIT-15 was reduced to 0.76 MHz.

Performance studies were conducted on both the RIT-15 and RIT-35 thrusters in an attempt to increase the ionization efficiency and to lower the power-to-thrust ratio to the range achieved by Kauffman and Hall-effect electrostatic thrusters. The performance tests for the RIT-15 showed that a thrust of 35 mN for xenon and 28 mN for krypton were achievable. Using xenon for propellant, the RIT-35 thrust performance was between 50 to 200 mN.

The earlier designs of the RIT evolved from a cylindrical ionization vessel to a (hemi) spherical vessel in order to reduce the area for wall recombinations without lowering ionization probabilities. This new configuration yielded an ionization production cost of 275 eV/ion with an optimum specific power consumption of 25.5 W/mN and a propellant utilization efficiency of 92%. Another shape of interest for the ionization chamber that reduces the occurrence of collisional recombination by minimizing the surface area of the walls is conical. A new engine, called the RIT-XT, was designed based on this concept to produce a thrust level between 100–200 mN. Tests results showed that, using this configuration, the ion production cost was

reduced to 191–232 W/A for specific impulses from 2987–4600 s. The propellant utilization efficiency was between 80 and 96%. The conical ionization chamber provided the additional advantage of increased shock and vibration capability [15, 17, 18].

While the first rf ion thrusters were designed to use mercury as the propellant, they were adapted to use xenon—the RIT-10 in 1982 for its flight onboard *Eureca* in 1992, and the RIT-35 in 1988. This change was made because xenon's high atomic mass maintains thruster efficiency while eliminating the environmental concerns and potential spacecraft contamination with mercury [15].

2.1.3.3 Scaling down of rf ion thrusters

Until now the application of this type of propulsion system has been limited to large satellites and space platforms such as *Eureca*. Giessen University developed a small scale system (RIT-4), but this remained an isolated attempt since the main focus was the development of large scale systems.

After focusing for many years on larger size rf thrusters, recent efforts have been made by the Giessen group to continue the development of the RIT-4. A series of rf microthrusters are being designed to be experimentally investigated [1]. The goal of our present research is to develop a miniature rf ion thruster (MRIT), which uses a small amount of propellant. This type of thruster would especially benefit the small satellite community, where the total mass of a satellite is limited to a few kilograms.

2.1.4 Some Principles of Plasma Physics

2.1.4.1 Plasma and sheaths

Plasma generally is referred to as "the fourth state" of matter. Lieberman and Lichtenberg [6] define it as:

> "a collection of free charged particles moving in random direction that is, on average, electrically neutral."

Over 99% of the universe is assumed to be in plasma state as the stars and most of the insterstellar matter are themselves plasma. Figure 2.4 shows different kinds of space plasma, as well as laboratory plasma, and their domain of existence.

All known plasma can be roughly classified into two main pressure domains: low-pressure discharges and high-pressure discharges. Table 2.3 summarizes the characteristics of these two domains.

Table 2.3. Plasma pressure domains.

	Low-pressure discharges	**High-pressure**
Pressure, p	1 mTorr–1 Torr	$\gg 1$ Torr
Electron temperature, T_e	1–10 eV	0.1–2 eV
Density, n	10^8–10^{13} cm^{-3}	10^{14}–10^{19} cm^{-3}
Temperature comparison	$T_i \ll T_e$	$T_i \leqslant T_e$

The interface of the plasma with the wall surface is made through a thin positively charged layer called "sheath". Within these positive space charge sheaths exist high electromagnetic fields, which lead to dynamics described by various ion space charge sheath laws, including low voltage sheaths and various high voltage sheath models, such as the collisionless and collisional Child's laws and their modifications.

In order to study plasma effectively, plasma dynamics and sheath dynamics must be joined at the plasma–sheath interface. This is ususally done by requiring the mean velocity at the plasma–sheath interface to be equal to the ion sound (Bohm) velocity, $u_B = (eT_e/M)^{1/2}$, where e is the ion charge, M is the mass of the ion, and T_e is the electron temperature.

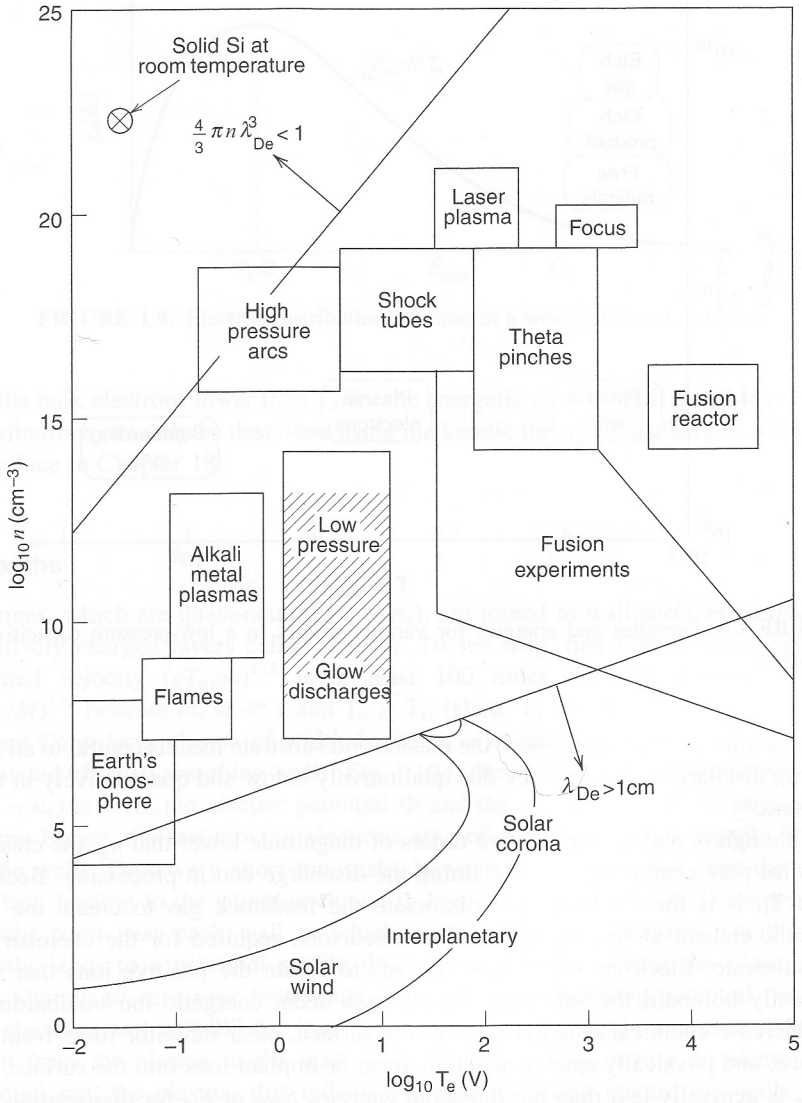

Figure 2.4. Different types of plasma and their domains of existence [6].

2.1.4.2 Basic plasma equations

The charged particles within a plasma interact with (i.e., are modifed by and themselves affect) any external electric and magnetic fields. This makes for a self-consistent system. Some simplifying approximations can be made in order to facilitate the understanding of such a system. First, interparticle collisions are treated separately from larger scale fields when determining the equilibrium distribution of charged particle velocities. This can be assumed since these collisions occur on a much shorter spatial and temporal scale than those caused by applied fields or the fields resulting from the average motion of the particles. A second approximation consists of averaging the velocity distribution over all velocities to obtain a macroscopic description of motion. With these two approximations, the following macroscopic equations can be used to describe a plasma:

- Continuity equation

$$\nabla \cdot (nu) = \nu_{iz} n_e \tag{2.4}$$

- Force equation

$$mn \left[\frac{\partial u}{\partial t} + u \nabla u \right] = qnE - \nabla p - mn\nu_m u \tag{2.5}$$

- Isothermal equation of state

$$p = nkT \tag{2.6}$$

- Energy conservation equation

$$\nabla \left(\frac{3}{2} pu \right) = \frac{\partial}{\partial t} \left(\frac{3}{2} p \right) \tag{2.7}$$

Another important characteristic is quasi-neutrality. The potential variation accross a plasma of length $l \gg \lambda_{\mathrm{De}}$ can be estimated from Poisson's equation, i.e.,

$$\nabla^2 \Phi \sim \frac{\Phi}{l^2} \sim \left| \frac{e}{\epsilon_0} \left(Z n_i - n_e \right) \right|. \tag{2.8}$$

Since $\Phi \leqslant \mathrm{T}_e = \frac{e}{\epsilon_0} n_e \lambda_{\mathrm{De}}^2$, for $\lambda_{\mathrm{De}}^2 / l^2 \ll 1$, $|Z n_i - n_e| \ll n_e$, which is the basic statement of quasi-neutrality of plasma and is called the "plasma approximation". This approximation is not valid within the plasma sheath in close proximity to a material wall [6].

2.1.4.3 Atomic collisions

In any given plasma, several types of particle collisions can be considered between positive ions and neutral gas atoms. Electron collisions with atoms generally result in both elastic scattering (in which the electron momentum is changed) and inelastic scattering such as excitation and ionization. In all these collisions, it is assumed that the momentum and energy of the interacting particles are conserved. On the one hand, the electrons and fully stripped ions only have kinetic energy. On the other hand, atoms and partially stripped ions possess internal energy level structures and can be excited, de-excited, or ionized, which result in changes in their potential energy [6].

Figure 2.5 shows a flux $\Gamma = nv$ of particles having a mass m, density n, and fixed velocity v incident on a half-space $x > 0$ of stationary, infinite massive target particles having a density n_0. The incident number of particles dn is proportional to n, n_0, and the differential distance dx as

$$dn = -\sigma n n_0 dx. \tag{2.9}$$

The constant of proportionality σ is called the cross section for interaction and is the fundamental quantity characterizing a collision.

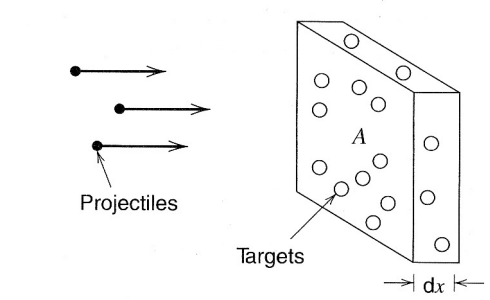

Figure 2.5. Flux of particles arriving on target particles [6]

In the case of hard sphere collisions, taking the angle of incidence equal to the angle of reflection, as shown in Figure 2.6, the cross section is then equal to

$$\sigma_{90} = \frac{\pi a_{12}^2}{2}. \tag{2.10}$$

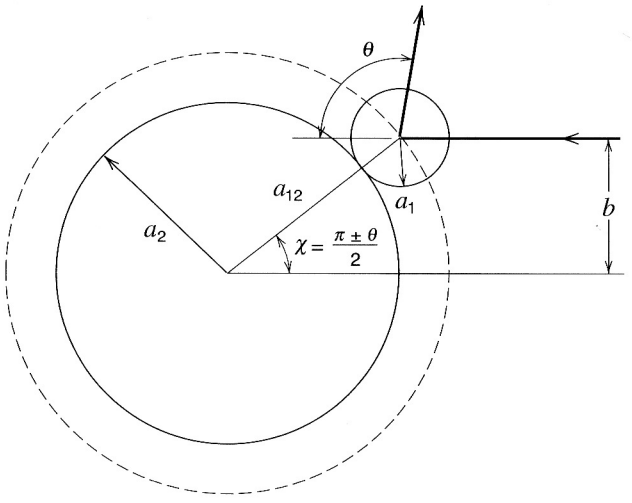

Figure 2.6. Hard sphere collision [6]

Figure 2.7 illustrates that a particle incident at a distance b off-center from

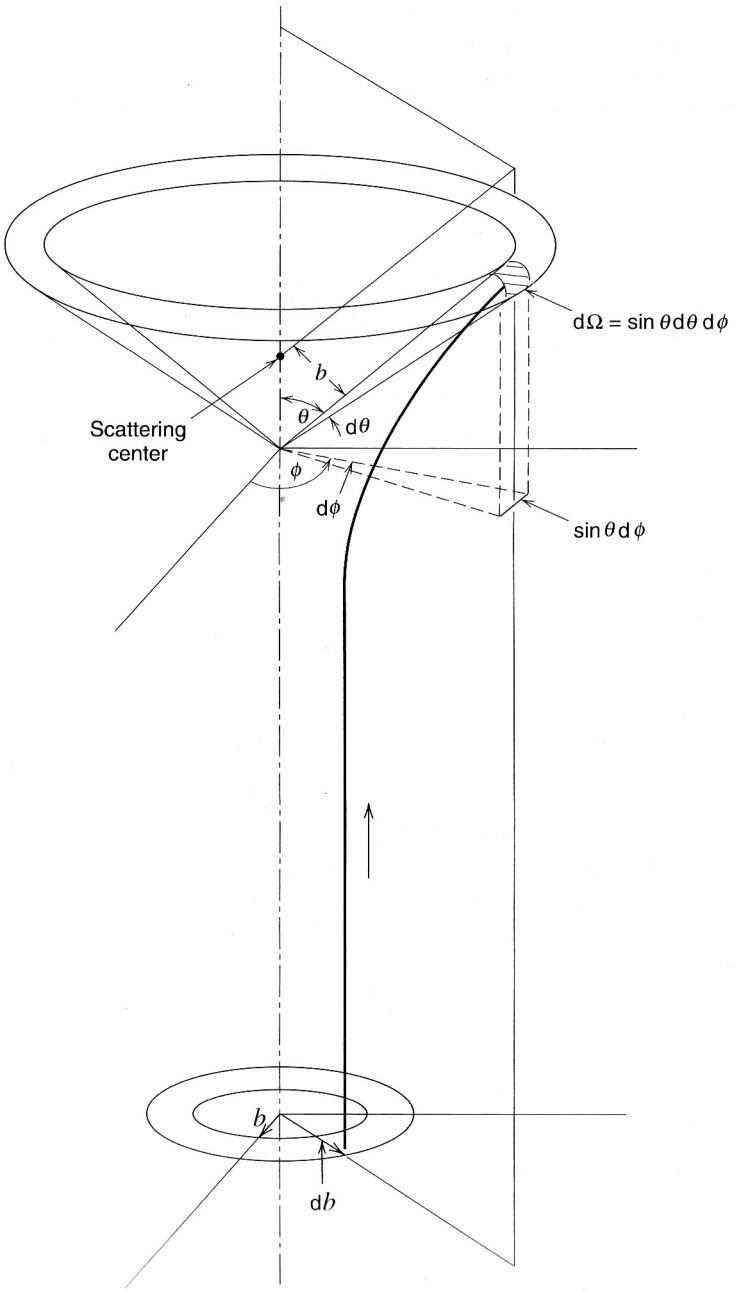

Figure 2.7. Collision scattering cone [6]

the target partcle is scattered through an angle θ. The parameter b is called the *impact parameter* and θ the *scattering angle*. The total scattering cross section is given by

$$\sigma_{sc} = 2\pi \int_0^{\pi} \frac{b}{\sin\theta} \left| \frac{db}{d\theta} \right|, \tag{2.11}$$

which for hard-sphere collisions becomes [6]

$$\sigma_{sc} = \pi a_{12}^2. \tag{2.12}$$

2.2 Plasma Modeling

2.2.1 Experimentally-based vs. Self-consistent Models

Experimentally-based models based use experimental measurements—i.e., voltage, current (total, ion, electron), impedance, electron density, electron temperature, ion flux, excited or ground-state species density, consumption of gas precursors, deposition rate, etc.—as model inputs. These models further explain experimental measurements allowing us to determine values for quantities not directly measurable. They have the advantage of very short computational times while being able to achieve very good estimates of measurable quantities. On the other hand, generalization of their results are hard to achieve since they only can be used in systems for which the experimental results are available.

Self-consistent models have the advantage that they can be applied to any system if a specific geometry is given and that they handle all sub-processes with very few inputs. One of their major disadvantage is the length of the computational time, which can lead to models that are not practical. In addition, the assumptions often adopted in order to decrease the computational time lead to significant errors

and results that lead to discrepancies from experimental measurements.

2.2.2 Analytical Modeling

The number of assumptions used in the analytical model is usually quite large. They are used mostly for one-dimensional simulations and almost exclusively for the modeling of the plasma electrical properties. The most common approach in these models is to separate the discharges into three regions (two sheaths and the bulk plasma). Analytical models are the easiest and the fastest to implement and have provided in many case good results for the simulation of electrical properties of discharges [6]. Due to the level of complexity associated with the larger number of assumptions, the use of such models is limited to simulation of noble gas discharges.

2.2.3 Numerical Modeling

2.2.3.1 Kinetic description

Kinetic models are temporally and spatially dependent solutions of the Boltzmann equations, which produces electron and ion velocity distributions either by direct integration of the equation or by applying statistical techniques (Particle in Cell–Monte Carlo method). The kinetic approach, although it is computationally intensive, is the least dependent on *a priori* assumptions leading to more accurate results.

2.2.3.2 Fluid description

Fluid models solve moments of the Boltzmann equation in time and space, while the electron energy distribution function (EEDF) is calculated off-line and coupled to the fluid model, providing the electron transport coefficients and the rate of

electron molecule reactions. Due to the shorter computational times, the fluid approach, although it is not as accurate compared to kinetic methods, allows for higher dimensionality (2-D, 3-D) and for the introduction of more detailed physics to the models. However, these models are limited to gas pressures above 200 mTorr, as they assume a local equilibrium between electrons and the electric field.

2.2.3.3 Hybrid kinetic/fluid description

Hybrid models use the kinetic approach to handle the non-local transport of electrons and ions in the discharge and to derive the transport coefficients of charged species. The fluid approach is simultaneously applied in order to provide the density of the charged species and the electric field distribution. Hybrid models have been developed in order to simulate rather complex chemistries of gas discharges. The transport coefficients and the rates of reaction of electrons with molecules are derived kinetically, while the density of species and the temporal and spatial variation of the electric field are calculated using the fluid flow approach.

2.2.4 Non-Local Electron Kinetics and Electrodynamics

Non-local coupling of the EEDF and its scalar integrals with the rf electric field (non-local electron kinetics) is well recognized as an underlying feature of low pressure discharges, independent of the electron heating mechanism, i.e., dc, rf, or microwave discharge [9–11]. When the electron thermal conductivity is large (little change in electron energy due to collisions with heavy atoms), the electron energy relaxation length λ_E is larger than the plasma size, L, or the characteristic length of the rf field localization (skin depth) δ, $\lambda_E \gg L, \delta$.

In the mTorr pressure range corresponding to nearly collisionless electron mo-

tion, when an electron crosses a skin depth without collision in a small fraction of the rf field period, $v_{\rm th}/\delta(\omega^2 + \nu_{en}^2)^{1/2}$, non-local electrodynamics effects due to electron thermal motion may play an essential role in ICP operation [12,13]. Here, $v_{\rm th}$ is the electron thermal velocity (δ the characteristic scale of the electromagnetic field skin depth), ω the driving frequency, and ν_{en} the electron–neutral collision frequency. Under such conditions, the rf current in the ICP is not locally coupled with the rf field (anomalous skin effect); thus, the cold plasma conductivity formula is not applicable. In this regime, one can observe a non-monotonic space distribution of the rf field and rf current, collisionless electron heating, and negative power absorption. Many of these effects have been found recently in experiments with low pressure ICP using rf magnetic probes [14–17].

2.2.5 Previous Modeling Efforts and Experimental Studies

2.2.5.1 General ICP models and experiments

Thompson was the first to describe an inductive discharge in 1929. Several other descriptions of this *electrodeless ring discharge* experiment followed [19, 20, 21].

A one-dimensional model was developed by Lister and Cox for studying the electromagnetic properties of inductively coupled discharges [22]. In this model, the coil was assumed to be sufficiently long relative to the radial dimensions of the discharge, allowing end effects to be considered negligible so that physical variables depend only on the radial position r. The electromagnetic field was found through the use of Hankel and Bessel functions [22].

Another modeling approach consisted of considering an inductive discharge to be a one-turn secondary of an air-core transformer [6]. In this scenario, expressions for spatially averaged quantities representing the different discharge parameters

such as the voltage, current, and electric field are then determined as functions of measured electrical parameters of the primary circuit. Further description of the transformer model is provided in Chapter 3.

Most of the descriptions, models, and experiments available for ICPs are for flat coil geometries due to the high interest in their practical applications in material processing [23]. Yin, in particular, addressed the challenges involved in the miniaturization of flat ICPs [28].

2.2.5.2 Capacitive–inductive discharge transition

Chandrakar, in 1978, was the first to provide a description for the transition between the first (capacitive) stage and the second (inductive) stage of the electrodeless ring discharge [29]. Refinements to this description came in particular with the works of Turner and Kortshagen, among others, with the support of more experimental evidence [7, 30, 32, 33, 34, 35, 36, 37, 48].

Kolobov and Godyak were the first to discover nonlinear effects in inductively coupled sources, highlighting collisionless power absorption [49]. Based on this discovery, several descriptions of the phenomena were attempted [8, 50, 52]. The density jump and hysteresis, which are part of the transition from E–to–H mode, were shown to be caused by the nonlinearity of either or both the power transfer and power dissipation [7].

In the case of low-pressure discharges, the domain in which the MRIT falls, Kaganovich *et al.* have established a set of self-consistent equations to describe inductive discharges. Their formalism, valid for both flat and cylindrical ICPs, takes into account the collisionless heating mechanism that becomes predominant in such low pressure discharges [8].

2.2.5.3 Extraction and acceleration grids

Ion thrusters are characterized by the electrostatic acceleration of ions extracted from the plasma generator [1]. The ion accelerator consists of electrically biased multi-aperture grids, and this assembly is often called the ion optics. The design of the grids is critical to the ion thruster operation and is a trade between performance, lifetime, and size. Since ion thrusters need to operate for years in most applications, lifetime is often a major design driver. However, performance and size are always important in order to satisfy the mission requirements for thrust and specific impulse (I_{sp}) and to provide a thruster size and shape that fits onto the spacecraft.

A number of computer simulation codes have been developed [38, 39, 46] to more accurately evaluate the ion trajectories produced by thruster grids. Ion optics codes solve in two or three dimensions the combined ion charge density and Poissons equations for the given grid geometry and beamlet parameters. These codes have been used for the design and analysis of two- and three-grid systems, and were extended to four-grid systems [42] to examine two-stage ion optics performance for very high voltage, high I_{sp} applications. Also, an extensive analysis of ion optics behavior in thrusters was completed by Farnell [41]. Displacement of the acceleration grid aperture relative to the screen grid centerline causes an off-axis deflection of the ion trajectories, commonly called beam steering. The effect of aperture displacement on the beamlet steering has been investigated for many years in both ion sources and ion thrusters [45].

The most important wear mechanism in modern ion thrusters is accelerator grid erosion. Current from secondary ions generated downstream of the discharge chamber impacts the accelerator grid. These secondary ions are generated by

resonant charge exchange (CEX) between beam ions and neutral propellant gas escaping from the discharge chamber. This process results in a fast neutral atom in the beam and a slow thermal ion. These slow ions are attracted to the negatively charged accelerator grid, and most hit with sufficient energy to sputter material from the grid. Eventually, the accelerator grid apertures become too large to prevent electron backstreaming or enough material is sputtered away that the grids fail structurally.

The second region of grid erosion is caused by charge exchange ions generated downstream of the accelerator. The ions are then attracted back to the accelerator grid by its large negative potential. On impact, these ions sputter away material from the downstream surface of the accelerator grid. Sputter erosion by these backstreaming ions results in a hexagonal pits-and-grooves erosion pattern on the downstream grid surface, which can lead to structural failure of the grids if the erosion penetrates all the way through the grid. Erosion of the acceleration grid aperture edge by backstreaming ions can also effectively enlarge the accel grid aperture diameter, leading to the onset of electron backstreaming [12, 38].

2.3 Research Description

2.3.1 Preliminary Experimental Work and Modeling Approach

2.3.1.1 Proof-of-concept experiments

The initial experimental proof-of-concept version of the Miniature Radio-Frequency Ion Thruster (MRIT) followed the general design rules for rf thrusters. It includes an ionization chamber, made of quartz, surrounded by an 11-turn, 18-

gauge (AWG), rf-inductance coil. Xenon (or often argon is substituted due to cost) gas flows into the chamber where it is ionized using the energy contained in the fields created by the rf coil. A set of two molybdenum grids are located downstream.

A -1000-V dc voltage is applied between the grids creating an electric field that accelerates the ionized propellant, thus creating thrust. The chamber was initially made of quartz tubing for ease of fabrication and an rf-ionization coil was wrapped around it. Subsequently, another version of the ionization chamber was made out of Macor ceramic.

For the proof of concept, the 11-turn MRIT was placed horizontally in a vacuum chamber and tested at different input power levels and grid discharge voltages. It was shown that a discharge could be self initiated at very low rf power (~ 10 W) when a potential of -1000 V was applied to the grids. The proof-of-concept MRIT is shown firing in Figure 2.8. The rf power supply used to initiate and sustain the discharge was connected to the rf coil through a capacitive matching network described in Chapter 3. These proof-of-concept tests showed that generating a discharge on this small scale and at low power was indeed feasible. Subsequent development of the MRIT has been reported by Trudel *et al.* [58].

2.3.1.2 Modeling approach

First, the different possible types of initiation of the discharge possible were established and an analysis of the transition between the capacitive and the inductive mode was performed. Also general properties of the discharge were derived using the transformer model described in Chapter 3.

In order to refine the approach, the determination of the collisional modes was needed. From there a non-local, self-consistent kinetic model of the bulk plasma

Figure 2.8. MRIT firing inside the vacuum chamber.

was chosen.

A 1-D kinetic model, assuming a Maxwellian distribution for the electron velocity distribution function (EVDF) was derived. The radius of the thruster was taken as 0.6 cm (radius of the MRIT [58]) and an infinite length was assumed. This model was benchmarked to simulations available in literature. From the E and B fields calculated, the current density and thrust were derived for the MRIT. A comparison between the current density calculated and the one measured experimentally is available in Chapter 5. Finally, a model for thrust was developed and is also detailed in Chapter 5.

2.3.2 Models Employed

2.3.2.1 Transition model

In order to characterize the transition between the E-mode and the H-mode, the total power transferred to the plasma by capacitive and inductive discharge is

calculated from Maxwell's equations. Conditions required for stable operation in either mode are also derived. The underlying theory is presented in Section 3.2.3 and the results of the transition model are found in Section 4.2.

2.3.2.2 Transformer model

The electrical properties of an inductive low pressure rf discharge have been analyzed by considering the discharge to be a one-turn secondary of an air-core transformer. Expressions for spatially averaged quantities representing familiar discharge parameters such as the voltage, current, and electric field have been determined as functions of measured electrical parameters of the primary circuit. Based on an analytical expression relating the coupling between the electrical characteristics of the primary coil and the plasma load, scaling laws for plasma parameters and the rf power distribution between the inductor coil and the discharge have been determined. A detailed description of the transformer model is provided in Chapter 3.

2.3.2.3 Non-local self-consitent kinetic model

In the present study, a self-consistent system of equations for the kinetic description of non-local, nonuniform, nearly collisionless plasmas of low-pressure discharges derived by Kaganovich *et al.* [8] is used. It consists of the non-local conductivity operator and the averaged kinetic equation for calculation of the non-Maxwellian EEDF. A detailed presentation of the theory is available in Chapter 3. Results from this model are found in Chapter 5.

2.3.2.4 Thrust derivation

For its application to the performance analysis of the MRIT, a model of the two-grid acceleration system is developed. Figure 2.9 depicts the classic two-grid configuration. It consists of an acceleration grid and a screen placed upstream and aligned with the acceleration grid to block the ions missing the aperture.

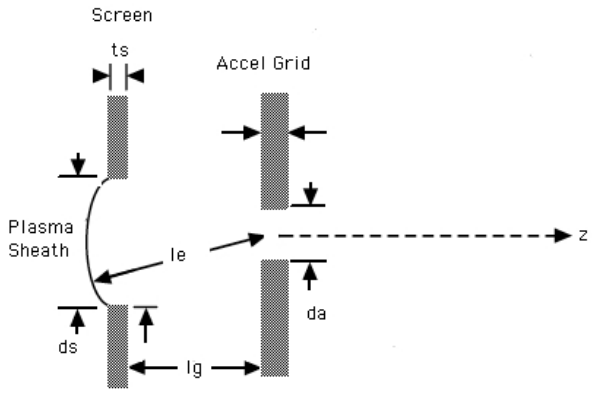

Figure 2.9. Two-grid configuration.

Thrust is then calculated from equations presented in Section 3.6 and results of these calculations are available in Chapter 5. A performance analysis model was then derived and a comparison between experimental results from the MRIT is performed (*cf.* Chapter 5).

2.3.3 Model Validation

2.3.3.1 Proof-of-concept experiments

From the proof-of-concept version, the design of the MRIT has evolved from an 11-turn to a 3-turn discharge as it has been shown that the thickness of the plasma sheath is proportional to the cube of the number of turns [6]. Too many turns increases the collisional losses occurring in the plasma sheath, thereby eroding

the efficiency of the thruster. Also, sets of extraction grids with different number of extraction holes, were tested. The number of holes were varied from 3 to 16, in order to develop an empirical correlation between grid geometry and thruster performance.

The latest thruster model is the smallest iteration to date with a conical plasma chamber that is 1 cm in both diameter and length. The total thruster diameter and length are each just over 2 cm. The thruster has been tested in a cylindrical vacuum chamber at pressures on the order of 10^{-6} Torr. This MRIT produces a maximum calculated thrust and specific impulse of 59.0 µN and 5480 s, respectively [58]. The overall performance of this thruster iteration was characterized by a series of tests conducted at The Pennsylvania State University from 2008–2010 and reported in Trudel [57].

2.3.3.2 Current MRIT iteration

As reported in Trudel [58], the MRIT successfully sustained operation with flow rates ranging to as low as 0.02–0.1 sccm. Maximum propellant efficiency occurred at the lowest functional flow rates. The two sets of tests conducted were for a total exit grid potential of 1200 V. The screen grid was set to +1000 V and the acceleration grid was set to −200 V. Arcing occurred between the grids at total voltages above 1700 V and thruster operation would become unstable at total voltages below 500 V. In the experimental study, the steady-state operating conditions for the MRIT were: +1000 V and −200 V screen and acceleration grid potential, respectively, 0.035-sccm propellant flow rate, and a delivered rf power level of 15 W. Figure 2.10 shows the MRIT firing in the vacuum chamber [58].

A Hewlett Packard 33120A Arbitrary Waveform Generator is used to produce the generate the rf field at a frequency of 1.5 MHz. It was then amplified by

Figure 2.10. MRIT firing in the vacuum chamber [58].

an RF Power Labs Model ML50 rf amplifier to provide the necessary range of rf power levels. This frequency was shown to be more efficient than the 13.56 MHz used in previous thruster iterations and proof-of-concept experiments reported in Section 2.3.3.1 above. Langmuir probe and Faraday cup measurements of the beam current provide experimental values of the electron densities and temperature to benchmark the model [58]. Figure 2.11 shows a diagram of the experimental setup.

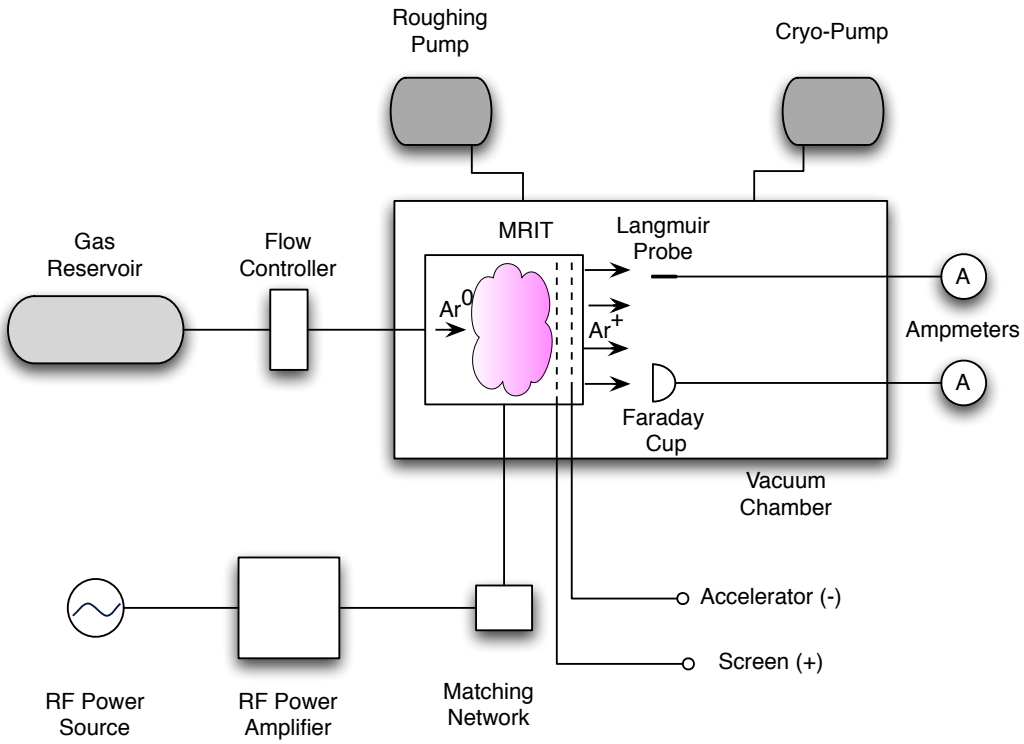

Figure 2.11. Schematic of the experimental setup for MRIT tests.

Chapter 3

Theoretical Description of Miniature Rf Discharges and Their Propulsion Applications

This chapter overviews the theory for some of the physical phenomena occurring in inductive plasma discharges and that are used in our models. It first gives an overall description of the plasma discharge within the MRIT. Employing a generalized description of an inductive discharge, we look into the initiation, transition, and thrust derivation for the different collisional domains seen by the MRIT.

3.1 Overall Description of a Cylindrical Inductive Discharge

An analysis of the plasma discharge, confined within a cylindrical region with radius R and length l, for a two-grid MRIT is presented. First, the operational modes are derived; then, conditions for initiation, discharge maintenance, and heating

mode transition for the different collisional domains are calculated. A transformer equivalent model of the discharge is used to analyze different experimental conditions encountered by the MRIT during testing. Then, a more elaborate model is built using a kinetic description to describe in particular the low pressure discharge regime. The overall performance of the thruster is evaluated with respect to the thrust efficiency.

3.1.1 Modeling Steps

The modeling steps chosen stemmed from initial questioning about the plasma behavior inside the thruster, and include questions such as:

- What type of collisional and pressure domains are seen in the thruster?
- Can it be considered an inductive discharge given the scale of the discharge?
- How is the discharge initiated?
- What are the necessary operational conditions for such a discharge in our configuration?
- What is the current produced in the discharge?
- What is the thrust range and performance of the MRIT?

From this line of questioning, two main approaches were selected to model the plasma discharge: first, a first-order look at the discharge, assessing the different parameters and establishing functioning modes, presented in Chapter 4; second, a more detailed model of the discharge kinetics, presented in Chapters 4 and 5. The various steps in the modeling of the discharge can be summarized as follows:

- Defining the collisional domains;

- Specifying the types of initiation;
- Determining the transition model;
- Developing the transformer model;
- Creating a 1-D kinetic model; and, finally,
- Investigating propulsion system applications.

3.1.2 General Description of an Rf Inductive Discharge

In the case of higher pressure discharges, a general description of the plasma discharge is given here. When an rf coil surrounding an ionization chamber is energized by an rf power source, an axial (z-directed) magnetic field is induced, which can be represented as

$$B_z = \mu_0 \frac{\mathcal{N}}{l} I_{\mathrm{rf}} e^{j\omega t}, \tag{3.1}$$

where μ_0 is the permeability of free space, $\mathcal{N}$ is the number of turns, l is the length of the discharge assumed to be equal to the length of the chamber, I_{rf} is the current in the coil, and ω is the angular frequency of excitation. A corresponding time-varying azimuthal (θ-directed) electric field is then generated and given by

$$E_\theta(r) = \frac{j\omega r}{2} \mu_0 \frac{\mathcal{N}}{l} I_{\mathrm{rf}} e^{j\omega t}, \tag{3.2}$$

where r is the radial distance from the center axis. The electric field generates an azimuthal current in the plasma that accelerates the electrons, thus increasing their temperature and sustaining the plasma during the ionization process. A schematic of this type of discharge is shown in Figure 3.1.

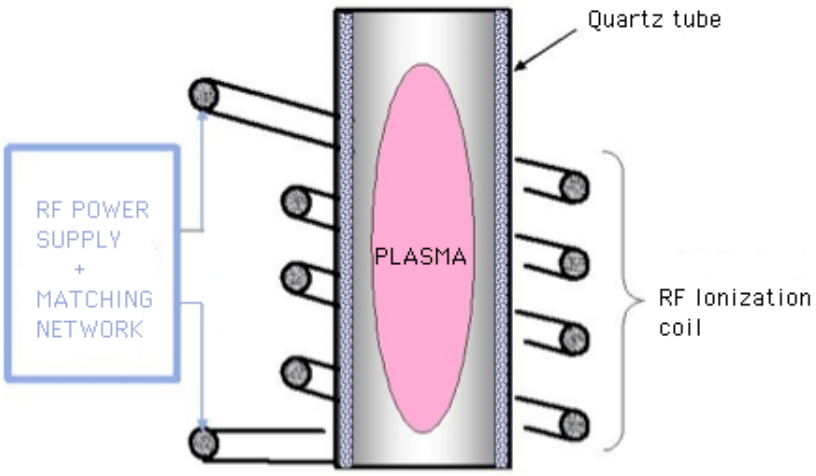

Figure 3.1. Cut-away schematic view of an rf cylindrical inductive discharge.

3.2 Initiation of Plasma Discharge

After more than 50 years of debate, it was established that an rf discharge is capacitive (i.e., E-mode) at lower densities with a transition to a mainly inductive mode (H-mode) at high densities [6, 20]. MacKinnon, in particular, was the first to notice the transition from the E-mode to the H-mode by observing the light emitted from the plasma discharge [59]. The E-mode is characterized by a faint light emission, whereas the light emission coming from the H-mode discharge is more intense [36].

3.2.1 Capacitive Discharge

Since there is no plasma before the initiation, the power dissipation from the coil to the gas is essentially zero. Thus, the stored reactive power of the coil is much higher before initiation. The voltage across the coil then is increased and, with an appropriate matching network, some of the voltage is capacitively coupled to the

inner wall of the chamber creating an electric field strong enough to break down the gas. The starting mechanism operates essentially through secondary electrons emitted by the impact of primary electrons on inner surface of the discharge vessel.

When a high frequency current passes through a coil, the electric field produced has two components: E_z in the axial direction and E_θ in the azimuthal direction [21]. Before initiation, E_z is larger than E_θ. The voltage necessary to initiate a discharge is roughly a function of the product of the spacing between electrodes (i.e., the two ends of the coil) and the pressure. At higher pressures, the required discharge voltage increases, making it difficult to start the plasma discharge if the electrode spacing is large. At very low pressures (or, more properly, pressure–distance product), there are too few collisions and electrons traverse the chamber and strike the walls without ionizing. For typical chamber geometries, it is very difficult to initiate a capacitive discharge at pressures less than 10–20 mTorr, though it is often possible to strike the discharge at higher pressure and then operate at only a few mTorr [21].

3.2.2 Characteristics of Capacitive Breakdown

The characteristics of this breakdown can be classified by comparing the characteristic lengths of the discharge (discharge length, l, electron mean free path, λ_e, oscillation amplitude, A, of free electrons, or of drift electrons):

- When the electron oscillation amplitude is small, i.e., when $A \ll l$ and $\lambda_e \ll l$, a minimum in the breakdown voltage is observed for $\nu_m \approx \omega$ (this is true at high frequencies with pressures not too low) [82];

- When the oscillation amplitude is comparable to length of discharge, sometimes two minima can be observed in the breakdown curve and the discharge

breakdown then is similar to microwave breakdown [82];

- When the discharge environment becomes that of a highly rarefied gas, the discharge initiation becomes equivalent to the breakdown of "vacuum" described in Raizer [82]. The few electron collisions already occurring are multiplied by secondary electron emission from the walls.

3.2.3 Discharge Transition from Capacitive to Inductive

At low power, it is generally assumed that the discharge is sustained by the electrostatic field generated by the capacitive coupling between the coil and the plasma (E-mode discharge). As the power is increased, there is a sudden transition to the electromagnetic mode (H-mode discharge) [6, 20, 36]. The dynamics of this transition have been analyzed for different geometric configurations and low pressure discharges. One can determine the minimum current necessary to sustain the H-mode discharge by applying an overall power balance to the discharge [6]. The power absorbed per ion–electron pair lost from the plasma is given by the equation

$$P_{\text{loss}} = e n_0 u_B A_{\text{eff}} \mathcal{E}_T, \tag{3.3}$$

with u_B being the Bohm velocity given by

$$u_B = \sqrt{\frac{e}{M}}, \tag{3.4}$$

and the effective area per particle loss, A_{eff}, given by

$$A_{\text{eff}} = 2\pi R^2 h_l + 2\pi R l h_R, \tag{3.5}$$

where h_l is the ratio of the axial sheath density to the center plasma density and h_R is the ratio of the radial sheath density to the center plasma density. In low pressure discharges, $n_s/n_0 \approx 0.5$ for $R \gg l$ (planar geometry) and $n_s/n_0 \approx 0.4$ for $l \gg R$ (infinite cylinder geometry). In intermediate pressures [6], $(R, l) \gtrsim \lambda_i \gtrsim (T_i/T_e)(R, l)$,

$$h_l \approx 0.86 \left(3 + \frac{l}{2\lambda_i}\right)^{-1/2}, \tag{3.6}$$

and

$$h_R \approx 0.80 \left(4 + \frac{R}{\lambda_i}\right)^{-1/2}. \tag{3.7}$$

The power delivered to the plasma through the inductive coupling is

$$P_{\text{abs}} = I_{\text{rf}}^2 R_1, \tag{3.8}$$

where R_1 is the plasma resistance seen in the primary inductive coil. For stable operation we require $P_{\text{abs}} = P_{\text{loss}}$, from which we obtain

$$I_{\text{rf}} = \left(\frac{n_0 u_B A_{\text{eff}} \mathcal{E}_T}{R_1}\right)^{1/2}. \tag{3.9}$$

Transition between the E and H modes does not occur at a well defined current; rather, the E-to-H transition occurs at much larger coil current than does the transition from H-to-E. Either an H- or E-mode can exist then between these two current values. This hysteresis behavior is due to the multiple solutions in the power balance equation and arises from nonlinear effects [36]. In low density regimes where $\delta_p \gg R$, the electromagnetic fields entirely penetrate the plasma. Applying Faraday's law, the electric field within the coil can be derived, i.e.,

$$E_\theta(r) = \frac{1}{2}\frac{j\omega r\mu_0 \mathcal{N} I_{\rm rf}}{l}. \tag{3.10}$$

For $\nu_m \ll \omega$, the power absorbed by the plasma can be evaluated as

$$P_{\rm abs} = \frac{\pi r l}{\sigma_{\rm eff}} \int J_\theta^2(r) dr = \frac{1}{16} I_{\rm rf}^2 \frac{\pi e^2 n_0 \nu_{\rm eff} \mu_0^2 N^2 R^4}{ml} \tag{3.11}$$

Taking into consideration electron–neutral collisions, the effective collision frequency is approximately the sum of the ohmic and stochastic collision frequencies:

$$\nu_{\rm eff} \approx \nu_m + \nu_{\rm stoc}, \tag{3.12}$$

with $\nu_{\rm stoc}$ given by

$$\nu_{\rm stoc} \approx \frac{\bar{v}_e}{4\delta}\left(\frac{1}{I(\alpha) + \alpha/4}\right), \tag{3.13}$$

where $I(\alpha)$ is the limit of the exponential integral $E_1(\alpha) = \int \frac{e^{-\zeta}}{\zeta} d\zeta$ with $\alpha = 4\omega^2\delta^2/\pi\bar{v}_e^2$. In our case, since $\alpha \ll 1$, $I(\alpha)$ is given by

$$I(\alpha) = -\frac{1}{\pi}(\ln\alpha + 1.58). \tag{3.14}$$

In an inductively coupled plasma discharge, the rf coil does not have to be in resonance to produce a plasma. This considerably simplifies the design and implementation of rf inductive-discharge devices. The 13.56-MHz frequency that was first chosen as an experimental discharge frequency is commonly used in inductive discharges since it is an unregulated industrial frequency. However, it was shown experimentally and herein that a lower frequency produces higher beam currents for thrusters of the size of the MRIT.

In inductive discharge processes, there are two main types of power transmis-

sion from the electric fields to the plasma electrons: collisional dissipation and collisionless heating. Both occur within a skin depth layer of thickness δ near the plasma surface. In the latter case (collisionless heating), there is a collision of the bulk plasma electrons with the oscillating inductive electric fields. The electrons are accelerated and consequently thermalized. This process is very similar to the one of stochastic heating in capacitive rf sheaths, in which case the electrons are reflected from the large fields of the moving high voltage sheath. The stochastic electron power in the current term is then given by

$$\overline{S}_{\text{stoc}} = \frac{1}{2}\frac{m_e \overline{v}_e}{e^2 n} J^2, \tag{3.15}$$

where J is the current density, n is the constant particle density, $\overline{v}_e$ is the average electron velocity, and m_e is the electron mass.

The collisional dissipation process, or ohmic heating, can be subdivided into two different regimes depending on the relative value of the electron–neutral momentum transfer frequency compared to the angular frequency. For $\nu_m \ll \omega$, the skin depth thickness, δ_p, is given by

$$\delta_p = \left(\frac{m}{e^2 \mu_0 n_s}\right)^{1/2}. \tag{3.16}$$

For $\nu_m \gg \omega$, the collisional skin depth is given by

$$\delta_c = \left(\frac{2}{\omega \mu_0 \sigma_{\text{dc}}}\right)^{1/2}. \tag{3.17}$$

For the case in which the average speed of the electrons contained within a skin depth of thickness δ_e satisfies the condition

$$\frac{\overline{v_e}}{2\delta_e} \gg \omega, \nu_m, \tag{3.18}$$

the interaction time between the electron and the skin depth layer is short compared to the rf period or the collision time [6]. The anomalous skin depth, δ_e, is then given by

$$\delta_e = \left(\frac{C_e \overline{v}_e}{2\omega\delta_p}\right)^{1/3} \delta_p, \tag{3.19}$$

where $C_e = 1/I(\alpha)$ is a quantity of order unity that depends weakly on v_e, δ_e, and ω. Typically, for low pressure discharges, the skin depth is approximately equal to δ_p. In inductive discharges, the energy loss is considerably lower than in a capacitive discharge since only a small amount of the coil rf voltage appears across the sheath even though the sheath thickness is much smaller than in a capacitive discharge [6].

3.3 Plasma in the Discharge Vessel

3.3.1 Determination of the Operating Regime

One can identify two main regimes depending on the electron mean free path relative to the dimensions of the ionization chamber. In the case of an electron mean free path that is smaller than the size of the discharge (or size of the chamber), the collision processes within the discharge include elastic and quasielastic collisions [50]. In the elastic range, where the kinetic energy is less than the first excitation energy, the problem can be resolved using one variable, the total electron energy, by performing a spatial average on the set of equations. Berstein and Holstein [64] and Tsendin [65] introduced this approach under the name of non-local approach. For the case where the mean free path is on the order of or larger than the size of the discharge chamber, the electron energy distribution function (EEDF) deviates greatly from a Maxwellian [8].

3.3.1.1 Determination of the pressure regime

The pressure seen within the discharge chamber of an rf ion thruster falls typically in the range from 10^{-4} to 10^{-2} Torr [1, 12]. Low pressure discharges are defined as when the ion–neutral mean free path, λ_i, is greater than or equal to the dimensions R and l of the thruster. The MRIT falls in this discharge regime for pressure less than 3×10^{-3} Torr. Intermediate pressures are defined when $(R, l) \gtrsim \lambda_i \gtrsim (T_i/T_e)(R, l)$. This occurs when the thruster operates between 3×10^{-3} Torr and 10^{-2} Torr.

3.3.1.2 Estimation of the initial pressure in the discharge chamber

The pressure through a cylindrical tube follows Poiseuille's law modified for compressible gas [12]. The rate, N_m, at which compressible gas flows through a tube of length l and radius a is

$$N_m = \frac{\pi}{8\zeta}\frac{a^4}{l}\frac{P_a(P_1 - P_2)}{R_0 T} \tag{3.20}$$

$$= \frac{\pi}{16\zeta}\frac{a^4}{l}\frac{P_1^2 - P_2^2}{R_0 T}, \tag{3.21}$$

where a is the tube radius, l is the tube length, P_a is the average pressure in the tube given by $(P_1 + P_2)/2$, ζ is the viscosity, P_1 is the upstream tube pressure, P_2 is the downstream tube pressure, R_0 is the universal gas constant, and T is the temperature of the gas. The pressure P_1 can be determined using

$$P_1 = \left(P_2^2 + \frac{0.78 Q \zeta T_r l}{d^4}\right)^{1/2}, \tag{3.22}$$

where Q is the flow in sccm, $T_r = T(\mathrm{K})/T_c$, T_c being the critical temperature of the gas [68], d and l are given in centimeters, and the pressures are in Torr. When

$T_r \leqslant 1.5$, the viscosity, ζ, in Poise is given by

$$\zeta = \frac{0.34}{A} T_r^{0.94}, \tag{3.23}$$

where $A = T_c^{1/6}/M^{1/2}P_c^{2/3}$, P_c being the critical pressure [68]. Otherwise, ζ is calculated from the following expression:

$$\zeta = \frac{0.1778}{A} \left(4.58T_r - 1.67\right)^{5/8} \times 10^{-7}[\text{Poise}]. \tag{3.24}$$

For argon, $A = 0.0276$ and $T_c = 151.2$ K. For xenon, $A = 0.0151$ and $T_c = 289.8$ K [68].

For a discharge of length l equal to 1 cm and radius a of 0.5 cm, and assuming that $P_2 \ll P_1$ and a neutral gas temperature close to 290 K, the estimated pressure P_1 is about 3.26×10^{-3} Torr for a flow rate of 0.0595 sccm, which matches the calculation from Loeb *et al.* for the RIT-1 ($\sim$3.2 $\times 10^{-3}$ Torr expected at the same neutral gas flow rate) [1].

3.3.1.3 Determination of the electron mean free path

The electron mean free path in the discharge is given by

$$\lambda = \frac{1}{n_g \sigma}, \tag{3.25}$$

where n_g is the neutral gas density and σ is the elastic scattering cross section in the gas considered (in our case: argon and xenon).

3.3.1.4 Implications of collisional regime and non-locality parameter

In the collisional regime, where the electron–neutral momentum transfer frequency, ν_m, is much greater than the angular coil excitation frequency, ω, the relationship between the electric field and the current density is local and can be derived from Ohm's law,

$$J = \sigma E. \tag{3.26}$$

This collisional regime exists at high gas pressures where electron collisions with neutrals are responsible for the heat transfer [51].

In low pressure discharges where collisionless heating occurs, there is a non-local coupling between the EEDF and its scalar integrals with the heating electric field. This applies regardless of the kind of electron heating mechanism (e.g., microwave, dc, rf) [49]. Berstein and Holstein [64] and Tsendin [65] were the first to introduce the terminology "non-local approach". This approach uses the electron energy as an independent variable in the spatially inhomogeneous Boltzmann equation, i.e., everything is non-coupled [51]. One result of the field being non-local is the fact that charged particles change energy in a round-trip through the field region regardless of whether collisions occurred [51].

In low pressure discharges, it is shown that the energy relaxation length is large compared to the plasma width and that the main part of the electron velocity distribution is a function only of the total energy [8]. The local rf electric field no longer determines the electron current by means of Ohm's law. The electron current is a function of the whole profile of the rf electric field for distances on the order of the electron mean free path. In the case where the mean free path is on the order of or larger than the size of the discharge chamber, the EEDF deviates greatly from a Maxwellian [8, 49, 24]. The EVDF, *f*, is mostly isotropic [8] and

can be derived as a sum of a main isotropic part, f_0, which is a function of the total energy only, and a small anisotropic part, f_1.

Between the collisional and collisionless regimes can be found a third mode: a hybrid regime where both types of electron heating coexist. The electron behavior in this regime is governed by three frequencies:

- angular frequency of the rf field, ω,
- collision frequency, ν, and
- the bounce frequency, Ω.

The heating process occurs through electron interaction with the fields, reflections from the plasma boundaries, and collisions with neutral gas particles. This heating is non-local in the sense that the place where the electron interaction with the field and the place where the phase randomization collisions occur are spatially separated. Electron collisions with plasma boundaries (i.e., bouncing off of them) are more frequent than collisions with gas species [51].

A practical way to estimate the effects of non-locality in the discharge is to calculate the non-locality parameter, Λ, which is equal to the square of the ratio of the effective mean free path, λ_{eff}, to the classical (local) skin depth, δ. Λ is given by

$$\Lambda = \left(\frac{\omega_p v_T}{c}\right)^2 \frac{\omega}{\left(\omega^2 + \nu^2\right)^{3/2}}, \tag{3.27}$$

where ω_p is the plasma frequency, v_T is the mean velocity of the electron in the bounce motion, ω is the discharge frequency, and ν is the electron–neutral collision frequency. If $\Lambda \gg 1$, the non-local effects are pronounced, otherwise they can be neglected [51].

3.3.2 Collisions in Xenon and Argon Gases

Xenon electron cross sections are interpolated from values available in the literature. Below 0.05 eV, elastic cross section values are taken from Frost and Phelps [60]. Between 0.05 eV and 10 eV these values come from Koizumi *et al.* [61]. Values of the elastic, ionization, and excitation cross sections from 10 eV to about a 1000 eV are from the compilation made by Hayashi [62]. Argon electron cross sections are interpolated from values taken from Vahedi [63].

The ionization, excitation, and elastic cross sections are shown in Figure 3.2 and Figure 3.3 for xenon and argon, respectively. The elastic scattering cross section shows a low energy dependence due to a quantum mechanical resonance, the Ramsauer minimum. The total ionization cross section roughly follows the ionization cross section.

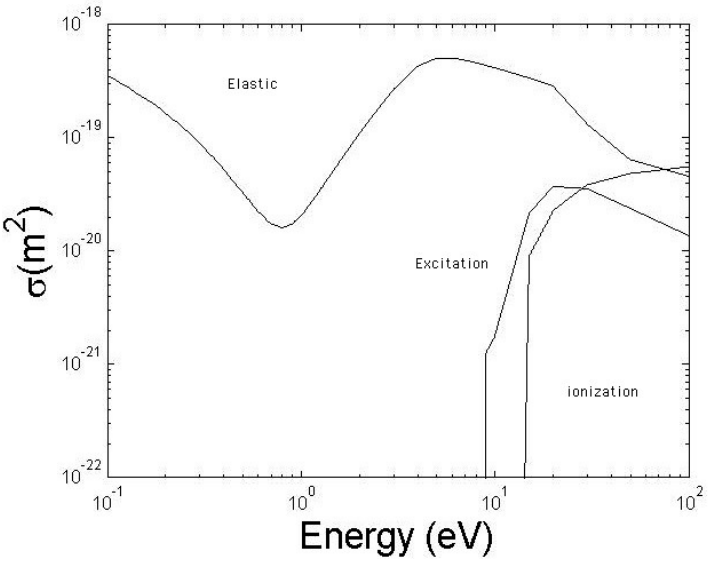

Figure 3.2. Ionization, excitation, and elastic cross sections for electrons in xenon gas.

An integration over the velocity distribution is performed in order to obtain the collision quantities in the plasma. Considering a collision between two groups

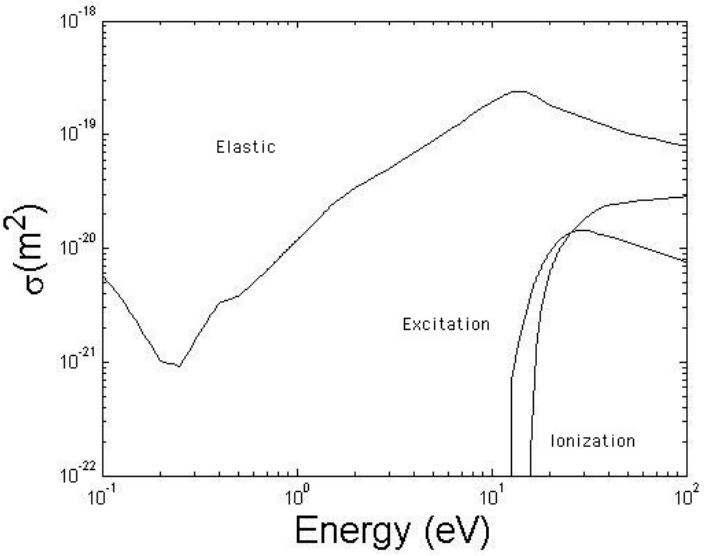

Figure 3.3. Ionization, excitation, and elastic cross sections for electrons in argon gas.

of particles, i.e., incident particles, indicated by subscript 1, and target particles by subscript 2, with respective velocities v_1 and v_2, the collision frequency and rate constant are given by

$$\nu = n_g K = n_g \langle \sigma(v_R) v_R \rangle_{v_1, v_2} \tag{3.28}$$

$$= n_g \int d^3 v_1 d^3 v_2 f_1(v_1) f_2(v_2) \sigma(v_R) v_R, \tag{3.29}$$

where K is the rate constant and the incident distribution is assumed to be Maxwellian [6]. Their associated distribution functions, f_1 and f_2, are normalized to unity. Assuming that the characteristic velocities of the target particles are negligible compared to those of the incident ones, the rate constant is given by

$$K(\mathrm{T}) = \langle \sigma(v) v \rangle_v \tag{3.30}$$

$$= \left(\frac{m}{2\pi k \mathrm{T}} \right)^{3/2} \int_0^\infty \sigma(v) v \exp\left(-\frac{m v^2}{2k\mathrm{T}} \right) 4\pi v^2 dv, \tag{3.31}$$

where m and T are the incident particle mass and temperature. For ionization, the Thompson cross section can be expanded near $\mathcal{E}_{\rm iz}$ as follows

$$\sigma_{\rm iz}(\mathcal{E}) = \sigma_0 \frac{\mathcal{E} - \mathcal{E}_{\rm iz}}{\mathcal{E}_{\rm iz}} \qquad \mathcal{E} > \mathcal{E}_{\rm iz}, \tag{3.32}$$

$$= 0 \qquad \mathcal{E} \leq \mathcal{E}_{\rm iz}, \tag{3.33}$$

where $\sigma_0 = \pi(4\pi\mathcal{E}_0\mathcal{E}_{\rm iz})$ and $\mathcal{E} = \frac{1}{2}mv^2/e$. The ionization collision rate can then be integrated to yield

$$K_{\rm iz}(\mathrm{T}_e) = \sigma_0 \bar{v}_e \left(1 + \frac{2\mathrm{T}_e}{\mathcal{E}_{\rm iz}}\right) e^{-\mathcal{E}_{\rm iz}/\mathrm{T}_e}. \tag{3.34}$$

Using the interpolated ionization, excitation, and elastic cross sections for xenon and argon given in Figure 3.2 and Figure 3.3, we obtain the rate constant $K(\mathrm{T}_e)$ shown in Figure 3.4 and Figure 3.5.

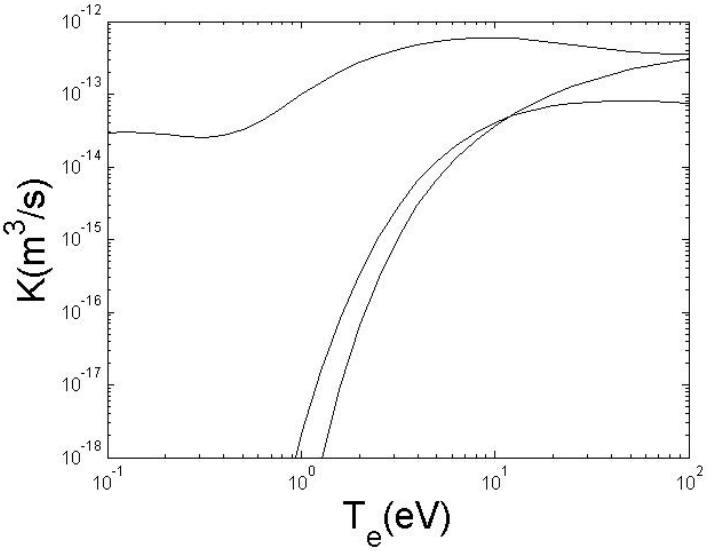

Figure 3.4. Ionization, excitation, and elastic rate constants for electrons in xenon gas.

The collisional energy loss per electron created can then be deduced from the

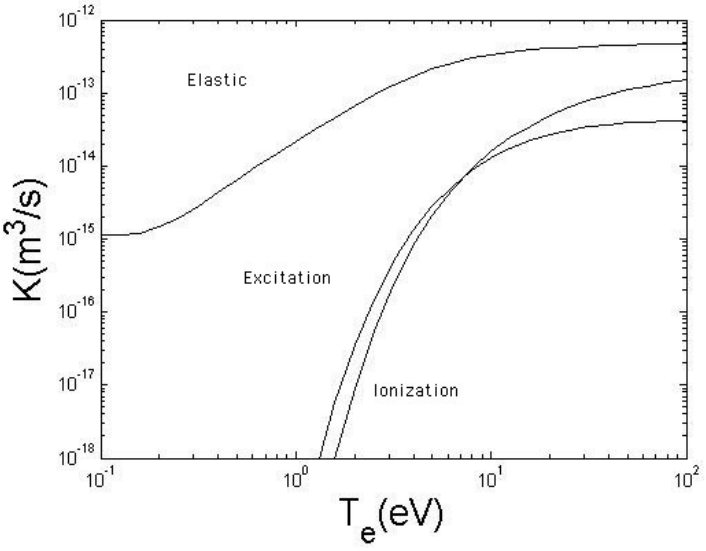

Figure 3.5. Ionization, excitation, and elastic rate constants for electrons for electrons in argon gas.

following expression

$$K_{\rm iz}\mathcal{E}_c = K_{\rm iz}\mathcal{E}_{\rm iz} + K_{\rm ex}\mathcal{E}_{\rm ex} + K_{\rm el}\frac{3m}{M}\mathrm{T}_e. \tag{3.35}$$

The resultant collisional energy loss per electron for xenon and argon are shown in Figure 3.6 and Figure 3.7.

Assuming a near-uniform cylindrical plasma and Maxwellian electrons absorbing an electrical power $P_{\rm abs}$, we can determine the electron temperature, T_e, of the plasma by equating the total surface particle loss to the volume ionization, i.e.,

$$n_0 u_B(2\pi R^2 h_l + 2\pi R l h_R) = K_{\rm iz} n_g n_0 \pi R^2 l. \tag{3.36}$$

This equality can be rewritten as

$$\frac{K_{\rm iz}(\mathrm{T}_e)}{u_B(\mathrm{T}_e)} = \frac{1}{n_g d_{\rm eff}}, \tag{3.37}$$

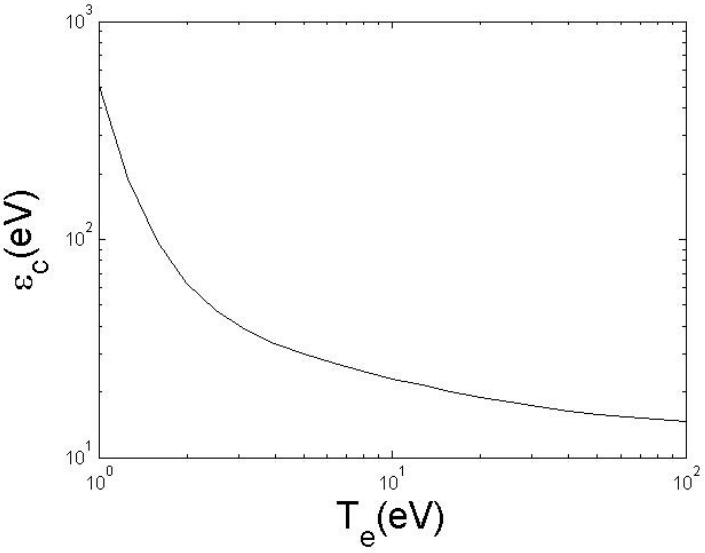

Figure 3.6. Collisional energy loss per electron–ion pair created, $\mathcal{E}_c$, versus T_e in xenon.

where

$$d_{\text{eff}} = \frac{1}{2}\frac{Rl}{Rh_l + lh_R} \tag{3.38}$$

is an effective plasma size for particle loss. The values of h_l and h_R, the axial and radial density ratio, respectively, are given by

$$h_l = \frac{n_{s,l}}{n_0} \approx 0.86\left(3 + \frac{l}{2\lambda_i}\right)^{-1/2}, \tag{3.39}$$

$$h_R = \frac{n_{s,R}}{n_0} \approx 0.80\left(4 + \frac{R}{\lambda_i}\right)^{-1/2}. \tag{3.40}$$

From our previously calculated values of $K_{\text{iz}}(T_e)$ and u_B, we obtain Figure 3.8 and Figure 3.9, the electron temperature distribution versus the product $n_g d_{\text{eff}}$.

The effective plasma size, d_{eff}, is given by Equation 3.38. At a given gas density, the electron temperature can be interpolated from Figure 3.8 and Figure 3.9 for

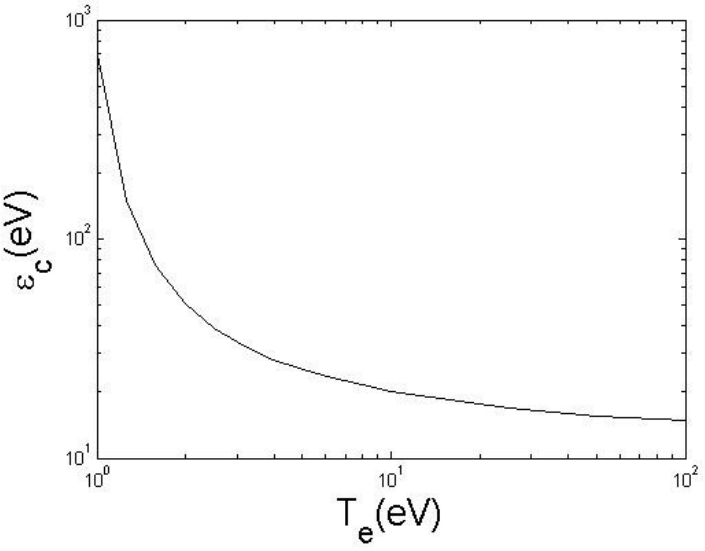

Figure 3.7. Collisional energy loss per electron–ion pair created, $\mathcal{E}_c$, versus T_e in argon.

xenon and argon, respectively. The collisional energy, $\mathcal{E}_c$, is then determined from Figure 3.6 for xenon and Figure 3.7 for argon. The ion kinetic energy loss at the surface is

$$\mathcal{E}_i = V_s + \frac{1}{2}T_e, \tag{3.41}$$

with V_s, the sheath voltage, given by

$$V_s = T_e \ln\left(\frac{M}{2\pi m}\right)^{1/2}. \tag{3.42}$$

The total energy loss per electron–ion pair created is

$$\mathcal{E}_T = \mathcal{E}_c + \mathcal{E}_e + \mathcal{E}_i. \tag{3.43}$$

The density at the center of the discharge then can be calculated as a function of

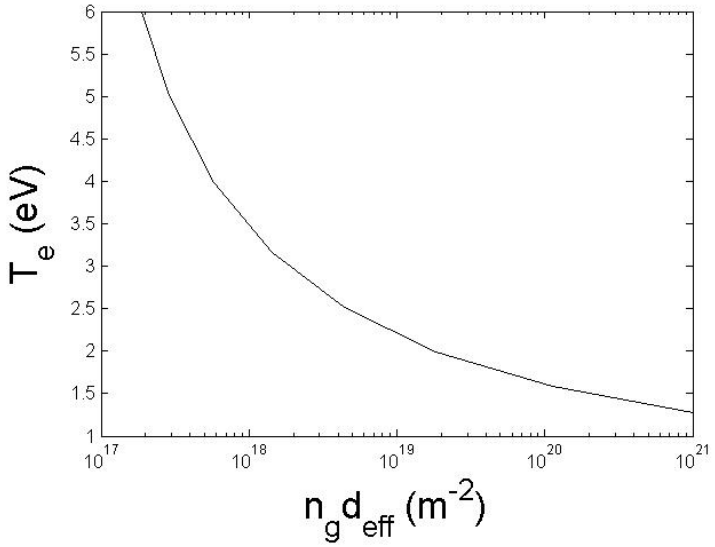

Figure 3.8. T_e versus $n_g d_{\text{eff}}$ for Maxwellian electrons in xenon.

the absorbed power P_{abs}, i.e.,

$$n_0 = \frac{P_{\text{abs}}}{e u_B A_{\text{eff}} \mathcal{E}_T}. \tag{3.44}$$

3.3.3 Coil–Plasma Coupling: Transformer Model

It has been established that an inductive discharge can be described as a transformer with the discharge as the one-turn secondary of an air-core transformer [6]. Gudmundsson and Lieberman applied this model to a cylindrical discharge with the inductive coil taken as the primary circuit and the plasma as the secondary circuit [24]. The magnetic field produced by a current flowing in the primary coil, composed of $\mathcal{N}$ turns with an inductance L_{11}, couples to the secondary coil. The plasma is considered as an electrically conductive fluid that can be viewed as a one-turn secondary winding core transformer with inductance $L_{22} + L_p$ and resistance

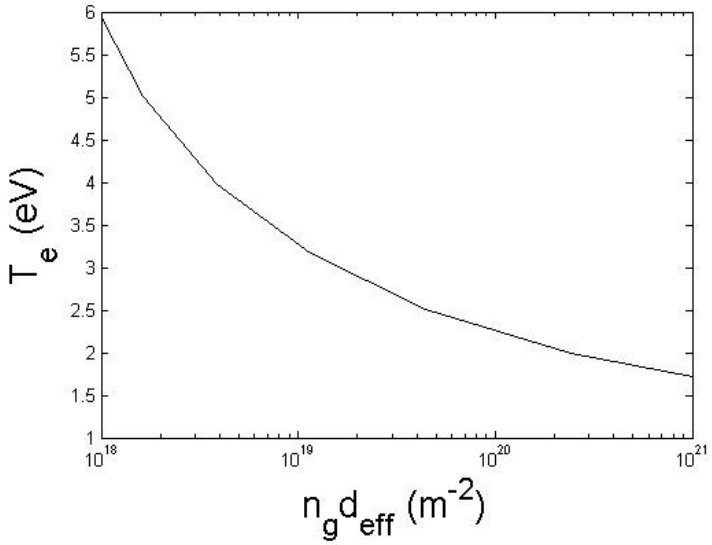

Figure 3.9. T_e versus $n_g d_{\text{eff}}$ for Maxwellian electrons in argon.

R_p. L_{22} is the magnetic energy storage inductance given by

$$L_{22} = \frac{\mu_0 \pi R^2}{l} \tag{3.45}$$

and L_p, which is the plasma inductance that accounts for the phase lag between rf electric field and the rf conduction current, and is given by

$$L_p = \frac{R_p}{\nu_{\text{eff}}}. \tag{3.46}$$

R_p is the plasma resistance given by

$$R_p = \frac{2\pi R}{\sigma l \delta_p}, \tag{3.47}$$

and $\nu_{\text{eff}} = \nu_m + \nu_{\text{stoc}}$, is a sum of the collisional and stochastic frequencies. The effective conductivity can be calculated as follows

$$\sigma_{\text{eff}} = \frac{e^2 n_s}{m\nu_{\text{eff}}}. \tag{3.48}$$

Figure 3.10 describes the electrical coupling of the inductive discharge. The inductance matrix written below

$$\tilde{V}_{\text{rf}} = j\omega L_{11}\tilde{I}_{\text{rf}} + j\omega L_{12}\tilde{I}_p \tag{3.49}$$

$$\tilde{V}_p = j\omega L_{21}\tilde{I}_{\text{rf}} + j\omega L_{22}\tilde{I}_p \tag{3.50}$$

is solved to find the primary coil inductance, L_{11}, as well as the mutual inductance $L_{12} = L_{21}$, to yield

$$L_{11} = \frac{\mu_0 \pi b^2 \mathcal{N}^2}{l}, \tag{3.51}$$

$$L_{12} = L_{21} = \frac{\mu_0 \pi R^2 \mathcal{N}}{l}. \tag{3.52}$$

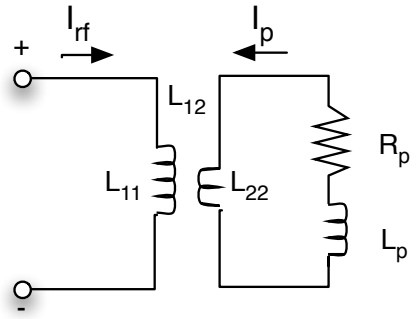

Figure 3.10. Transformer circuit model of inductive plasma discharge.

The impedance seen at the coil terminals is given by

$$Z_s = \frac{\tilde{V}_{\rm rf}}{\tilde{I}_{\rm rf}} \tag{3.53}$$

$$= j\omega L_{11} + \frac{\omega^2 L_{12}^2}{R_p + j\omega(L_{22} + L_p)}. \tag{3.54}$$

If $\delta_p \sim \delta_c \ll R$, then $R_p^2 + \omega^2 L_p^2 \ll \omega^2 L_{22}^2$, and

$$L_s \approx \frac{\mu_0 \pi R^2 \mathcal{N}^2}{l}\left(\frac{b^2}{R^2} - 1\right), \tag{3.55}$$

$$R_s \approx \mathcal{N}^2 \frac{\pi R}{\sigma_{\rm eff} l \delta_p}. \tag{3.56}$$

The absorbed power is then given by

$$P_{\rm abs} = \frac{1}{2}|\tilde{I}_{\rm rf}|^2 R_s. \tag{3.57}$$

3.3.4 Power Transfer Efficiency

The power transfer efficiency, ξ, is given by the ratio of the discharge power, P_d, which is the power transferred to the discharge and the total rf power, $P_{\rm rf}$, as follows

$$\xi = \frac{P_d}{P_{\rm rf}}. \tag{3.58}$$

Given that

$$P_{\rm rf} = P_d + P_{\rm lost}, \tag{3.59}$$

where P_{lost} is the power dissipated in the primary coil in the transformer equivalent model of the discharge, the power efficiency can be written as

$$\xi = \frac{1}{1 + P_{\text{lost}}/P_d}. \tag{3.60}$$

The ratio P_{lost}/P_d can be calculated from [24]

$$\begin{aligned} P_{\text{lost}}/P_d &= R_1/(R - R_1) \\ &= n^2 P_d (\omega k Q L_{11} V_p^2)^{-1} \left[\left(\frac{\omega L_{11}}{k n^2} + \frac{\omega}{\nu} \frac{V_p^2}{P_d} \right)^2 + \frac{V_p^4}{P_d^2} \right], \end{aligned} \tag{3.61}$$

where R is given by

$$R = R_{11} + \omega^2 k^2 \frac{L_{11} L_{22} R_{22}}{Z_s^2}, \tag{3.62}$$

with $k^2 = L_{12}^2/(L_{11}L_{22})$ being the coupling coefficient.

The minimum power loss needed in the primary coil to power a steady-state inductive discharge is given by

$$P_{\text{min}} = \frac{\mathcal{N}^2 V_p^2 (1 + \omega^2/\nu^2)}{\omega k Q L_{11}}. \tag{3.63}$$

From the expression of L_{11} given in Equation 3.52, this equation becomes

$$P_{\text{min}} = \frac{V_p^2 (1 + \omega^2/\nu^2) h}{\omega k Q \mu_0 \pi b^2}. \tag{3.64}$$

A modified expression of the inductance of a cylindrical coil with length l given by Piejak *et al.* [24] is

$$L_{11} = \frac{\mathcal{N}^2 \pi b^2 \mu_0}{l(1 + 0.88 b/l)}, \tag{3.65}$$

which gives

$$P_{\min} = \frac{V_p^2(1+\omega^2/\nu^2)h(1+0.88b/l)}{\omega k Q \mu_0 \pi b^2}. \tag{3.66}$$

Similarly, an upper limit for the discharge power, beyond which power transfer to the discharge becomes inefficient, can derived [24]. This maximum power, $P_{\max}$, is given by

$$P_{\max} = \frac{\omega P_d^2 L_0}{k^3 \mathcal{N}^2 Q V_p^2}. \tag{3.67}$$

The maximum power transfer is achieved when the reactance of the secondary circuit, X_{22}, is equal to the plasma impedance $|Z_p|$ as follows

$$X_{22} = \frac{\omega L_{11}}{k\mathcal{N}^2} = \frac{V_p^2(1+\omega^2/\nu^2)^{1/2}}{P_d} = |Z_p|. \tag{3.68}$$

This maximum power transfer coresponds to a mimimum of the ratio P_{loss}/P_d.

3.3.5 Matching Network

If the discharge is driven directly by an rf power source, then power is not transferred efficiently from the source to the discharge due to the impedance mismatch. Therefore, in order to operate more efficiently, a matching network, such as the one shown in Figure 3.11, between the source and the ionization coil is required. The admittance, Y_A, of the circuit is given by

$$Y_A = G_A + jB_A = \frac{1}{R_s + j(X_1 + X_s)}, \tag{3.69}$$

where the conductance, G_A, is given by

$$G_A = \frac{R_s}{R_s^2 + (X_1 + X_s)^2} \tag{3.70}$$

and the susceptance, B_A is given by

$$B_A = -\frac{X_1 + X_s}{R_s^2 + (X_1 + X_s)^2}, \tag{3.71}$$

where L_s and R_s are given by Equation 3.55 and Equation 3.56, respectively, and $X_1 = -1/(\omega C_1)$. For maximum power transfer, $G_A = 1/R_T$, where R_T is the Thévenin equivalent source resistance. C_2 is chosen then to cancel the susceptance B_A, which yields

$$C_2 = -\frac{B_A}{\omega}. \tag{3.72}$$

From the power absorption, $P_{\text{abs}} = \frac{1}{2} I_T^2 R_T^2$, I_T is determined [13].

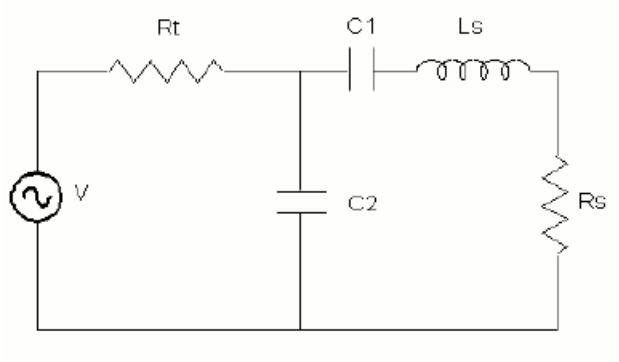

Figure 3.11. Matching network.

3.3.6 Total Power Transferred

The average power transferred by the inductive coupling and capacitive coupling, P_{ind} and P_{cap}, are calculated by integrating the Poynting vector over the surface

area of the plasma interface with the walls of the ionization chamber as follows

$$P = \mathrm{Re}\left[\frac{1}{2}\int(\mathbf{E}\times\mathbf{H^*})\right]\cdot d\mathbf{A}. \tag{3.73}$$

The average power transferred by inductive coupling, P_{ind}, is then given by

$$P_{\mathrm{ind}} = \mathrm{Re}\left[-j\frac{\omega\pi R\mu_0\mathcal{N}^2I^2}{l\alpha}\frac{J_1(\alpha R)}{J_0(\alpha R)}\right]. \tag{3.74}$$

The average power transferred by capacitive coupling, P_{cap}, is

$$P_{\mathrm{cap}} = \mathrm{Re}\left[-j\frac{\pi R}{\mu_0}\frac{\omega V_c^2\lambda\kappa_d^2}{lc^2\lambda'\kappa_p}\frac{J_0(\lambda R)J_1^2(\lambda' R)}{J_1(\lambda R)J_0^2(\lambda'(R+d))}\right]. \tag{3.75}$$

The total transferred power is then equal to the sum of the power transferred by capacitive coupling and the power transferred by inductive coupling as follows

$$\begin{aligned} P_{\mathrm{trans}} = -\,\mathrm{Re}\Bigg[j\Bigg(&\frac{\pi R}{\mu_0}\frac{\omega V_c^2\lambda\kappa_d^2}{lc^2\lambda'\kappa_p}\frac{J_0(\lambda R)J_1^2(\lambda R)}{J_1(\lambda R)J_0^2(\lambda'(R+d))} \\ &+\ \frac{\pi R\omega\mu_0\mathcal{N}^2I^2}{l\alpha}\frac{J_1(\alpha R)}{J_0(\alpha R)}\Bigg)\Bigg]. \end{aligned} \tag{3.76}$$

3.3.7 Kinetic Modeling in the Non-Local Domain

3.3.7.1 General description

In low-pressure discharges, the electron current does not follow Ohm's Law and, therefore, cannot be derived from the local rf field. It is a function of the profile of the rf field on distances of order λ. This generally also implies a non-Maxwellian electron energy distribution function (EEDF) in this type of discharge. A self consistent system of equations for the kinetic description of low pressure discharges can be derived from the semianalytic solution of the Boltzmann equation [8]. This

self-consistent set of equations comprises:

- the averaged kinetic energy for the isotropic portion of the electron velocity distribution function (EVDF);
- the reduced Maxwell's equations followed by the rf electric field;
- the quasineutrality condition for the electrostatic potential; and
- the ion density profile given by the fluid conservation equations for ion density and ion momemtum [67].

The EVDF, f, can be written as a sum of an isotropic, f_0, and an anisotropic function, f_1, i.e., $f = f_0 + f_1$ with f_0 being a function of a total energy. The Boltzmann equation for the electron velocity distribution can be written as

$$\frac{\partial f_1}{\partial t} + v_x \frac{\partial f_1}{\partial x} - \frac{eE_{sc}(x)}{m}\frac{\partial f_1}{\partial v_x} - \frac{eE_y(x,t)}{m}\frac{\partial \left(f_0 + f_1\right)}{\partial v_y} = C\left(f_1 + f_0\right), \tag{3.77}$$

where E_{sc} is the space-charge stationary electric field and $C(f)$ is the collisional integral [8]. The rf electric field E_y and the anisotropic part of the EVDF are harmonic functions. Applying quasilinear theory to Equation 3.77, f_1 follows the linear equation

$$\frac{\partial f_1}{\partial t} + v_x \frac{\partial f_1}{\partial x} - \frac{eE_{sc}(x)}{m}\frac{\partial f_1}{\partial v_x} - \frac{eE_y(x,t)}{m}\frac{\partial f_0}{\partial v_y} = C\left(f_1\right). \tag{3.78}$$

The symmetric part of the EVDF, $f_{1s} = 1/2\left(f_{1^+} + f_{1^-}\right)$ then is calculated using

$$f_{1s}(v,x) = -mv_y V_y^{\mathrm{rf}}\left(x, \epsilon_x\right)\frac{\partial f_0}{\partial \epsilon}, \tag{3.79}$$

where V_y^{rf} is the symmetric part of the oscillatory velocity of an electron [8]. Once the EVDF is known, we can calculate the current density from

$$j = -\frac{em^{3/2}}{4\pi\sqrt{2}} \int f_{1s} v_y d^3 v. \tag{3.80}$$

The rf electric field then follows from

$$\frac{d^2 E_y}{dx^2} + \frac{\omega^2}{c^2} E_y = -\frac{4\pi j \omega}{c^2} \left[j(x) + I\delta(x) - I\delta(x - L) \right], \tag{3.81}$$

where I is the current in the coil at $x = 0$.

The electric field equation, the equation for the electron current and the equation for the temporal Fourier transform of $\cos(k_1 x)$ in the bounce motion of the electron well make a complete system for determining the profile of the rf electric field [8]. In order to solve this system of equations, Fourier series expansions are used.

3.4 Thruster Performance Evaluation

3.4.1 Thrust Determination

In an ion thruster, a potential difference is applied between two acceleration grids, which results in an electrostatic force applied between the grids. Figure 3.12 shows the applied forces found in a two-grid acceleration system. The thrust, which is the force supplied by the engine to the spacecraft, is equal to the sum of the forces on the screen and accelerating grids. This net force on the grids is equal to and

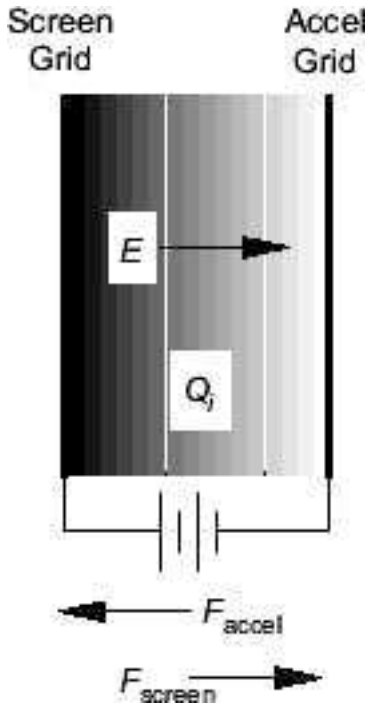

Figure 3.12. Forces on a two-grid acceleration system

opposite from the electrostatic forces, F_{ion}, on an ion between the grids, i.e.,

$$F_{\text{ion}} = \frac{1}{2}\epsilon_0 \left(E_{\text{accel}}^2 - E_{\text{screen}}^2\right), \tag{3.82}$$

where E_{accel} is the electric field at the acceleration grid and E_{screen} is the electric field at the screen.

Thrust is a function of the ion beam current, I_b, and the ion beam voltage, V_b, given by

$$T = \gamma\sqrt{\frac{2M}{q}} I_b \sqrt{V_b}. \tag{3.83}$$

The ion beam current can be derived from

$$I_b = T_g I_i, \tag{3.84}$$

where T_g is the screen transparency and I_i is the Bohm current given by [12]

$$I_i = \frac{1}{2} n_i e \nu_a A_g, \tag{3.85}$$

where n_i is the central ion density, ν_a is the ion acoustic velocity, and A_g is the total ion area loss taken as the grid area. The ion acoustic velocity can be derived from

$$\nu_a = \sqrt{\left(\frac{\gamma_i k}{M}\right)}. \tag{3.86}$$

If both singly and doubly charged ions are present in the beam, the beam current is then the sum of the currents induced by both types of charges, i.e., $I_b = I^+ + I^{++}$ and q is the mean ion charge, which, assuming 1% of the ionized ions are Xe^{++} ions [1], is equal to $1.02e$. The total thrust correction, γ, is the product of the beam divergence factor and correction factor for multiply charged species [12] given by

$$\gamma = \alpha_T F_T. \tag{3.87}$$

The parameter α_T is the thrust correction factor for thrust in the presence of doubly ionized atoms, given by

$$\alpha_T = \frac{I^+ + \frac{1}{\sqrt{2}} I^{++}}{I^+ + I^{++}}. \tag{3.88}$$

F_T is the force correction due to the effective thrust-vector angle. For a thruster with a constant ion current density profile accelerated by a uniform electric field, $F_T = \cos\theta$. For the case of a non-uniform beam current, F_T is given by

$$F_T = \frac{\int_0^r 2\pi r J(r) \cos[\theta(r)] dr}{I_b}, \tag{3.89}$$

where $J(r)$ is the ion current density as a function of the radius r. Figure 3.13

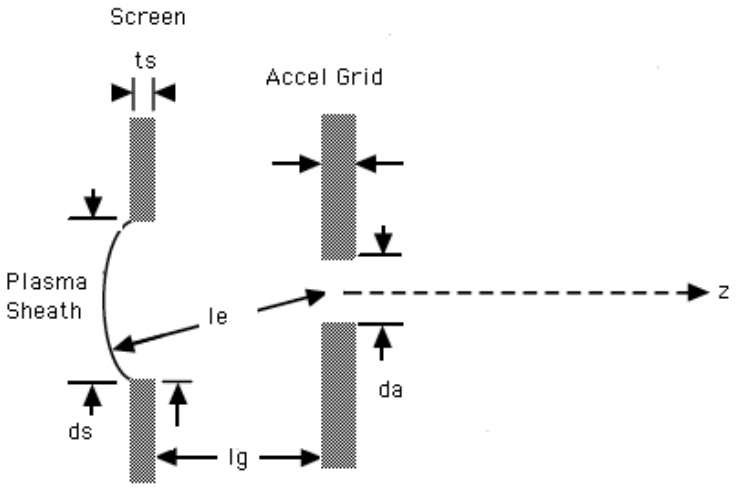

Figure 3.13. Two-grid acceleration system

shows a diagram of the two-grid acceleration system. The maximum beam current per hole, derived from Child–Langmuir theory, is given by

$$J_{B,\max} = \frac{4\epsilon_0}{9}\sqrt{\frac{2e}{M}}\frac{V_T^{3/2}}{l_e^2}, \tag{3.90}$$

where V_T is the total voltage between the two grids and l_e is given by

$$l_e = \sqrt{(l_g + t_s)^2 + \frac{d_s^2}{4}}. \tag{3.91}$$

The effective electric field in the acceleration gap is

$$E = \frac{V_T}{l_e}. \tag{3.92}$$

The maximum thrust can be calculated using the equation

$$T = \frac{8}{9}\epsilon_0 \gamma T_s \sqrt{R_n} E^2 A_g, \tag{3.93}$$

where A_g is the active grid area, T_s is the grid transparency, and the net-to-total voltage ratio, R_n, given by

$$R_n = \frac{V_b}{V_T}. \tag{3.94}$$

3.4.2 Thruster Performance

Thruster efficiency, η_T, is defined as the ratio of the thrust power, given by thrust multiplied by the exhaust velocity, to the total input power as follows

$$\eta_T = \frac{T v_{\text{ex}}}{P_{\text{in}}}. \tag{3.95}$$

Since the exhaust velocity is given by

$$v_{\text{ex}} = \frac{1}{2} T \dot{m}_p, \tag{3.96}$$

where $\dot{m}_p$ is the propellant mass flow rate, the thruster total efficiency can then be calculated from

$$\eta_T = \frac{T^2}{2\dot{m}_p P_{\text{in}}}. \tag{3.97}$$

Chapter 4

MRIT Operating Domains and Modeling Approach Validation

First, this chapter focuses on establishing the various operating domains encountered by the MRIT. Then, after a description of the modeling approach, validation of the codes are performed on available published data.

4.1 MRIT Collisional Regimes

In order to describe accurately the discharge within the MRIT, a mapping, as a function of pressure, of the various collisional regimes encountered is necessary.

4.1.1 Pressure Regimes

Low pressure discharges occur when the ion–neutral mean free path, λ_i, is greater than or equal to the dimensions R and l of the discharge chamber. The MRIT falls in this discharge regime for pressures less than 6×10^{-3} Torr. Intermediate pressures are defined when $(R, l) \gtrsim \lambda_i \gtrsim (T_i/T_e)(R, l)$, which corresponds to pres-

sures between 6×10^{-3} Torr and 2×10^{-1} Torr. Above this, pressure falls in the high pressure discharge range. Figure 4.1 shows the ion-neutral mean free path as a function of pressure with the various pressure regimes for the MRIT indicated.

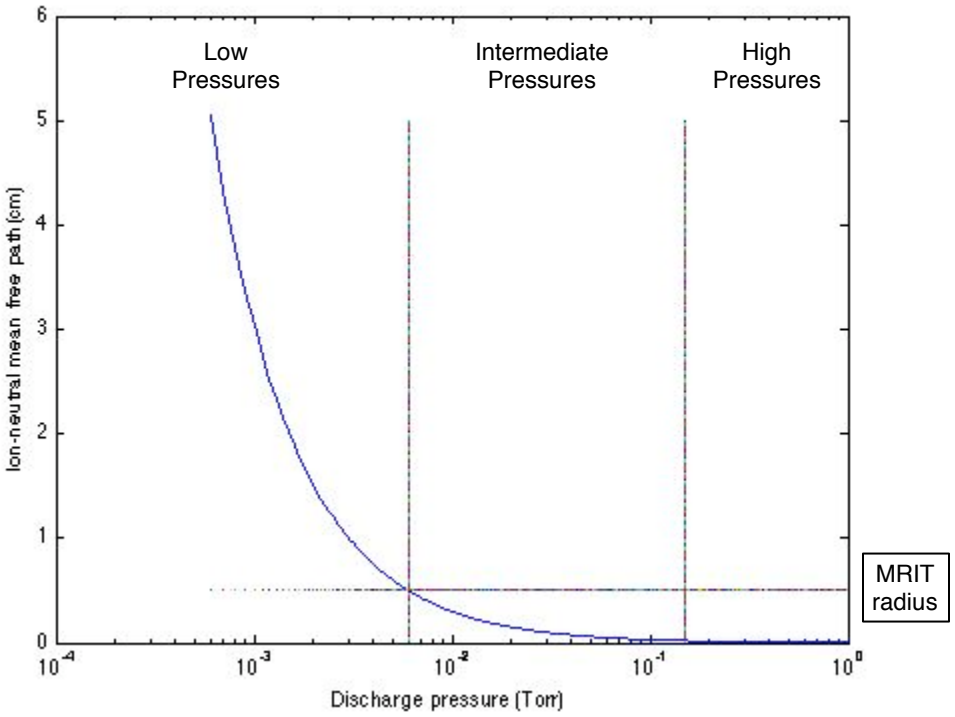

Figure 4.1. Ion–neutral mean free path as a function of pressure in the MRIT.

The pressure inside the discharge chamber, P_1, is derived from Poiseuille's equation modified for compressible flow (Equation 3.22). Assuming a vacuum chamber background pressure of 10^{-6} Torr and a temperature of 290 K, the pressure inside the discharge chamber is shown in Figure 4.2 as a function of the mass flow rate at the inlet of the tube.

For a discharge of length l equal to 1 cm and radius R of 0.5 cm, and assuming

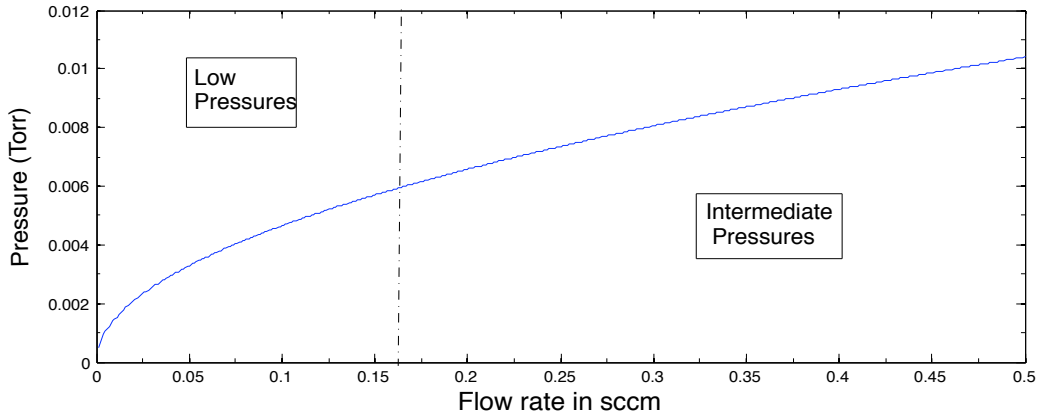

Figure 4.2. Pressure inside discharge chamber for a given flow rate.

that $P_2 \ll P_1$ and a neutral gas temperature close to 290 K, the estimated pressure P_1 is about 3.26×10^{-3} Torr for a flow rate of 0.0595 sccm, which matches calculations in Loeb *et al.* [1] for the RIT-1 (about 3.2×10^{-3} Torr expected at the same neutral gas flow rate). The pressure seen within the discharge chamber of a rf ion thruster typically varies from 10^{-4} to 10^{-2} Torr [1, 12].

4.1.2 Collisional Regimes

In order to determine the different collisional regimes experimented by the MRIT, calculation of the electron–neutral momentum transfer frequency is performed. As detailed in Chapter 3, three collisional domains can be established through comparison of ν_m and the operation frequency, ω:

1. For $\nu_m \ll \omega$, the discharge is collisionless;

2. For $\nu_m \gg \omega$, the discharge is collisional;

3. For $\frac{\overline{v}_e}{2\delta_e} \gg \omega, \nu_m$, the discharge is in a stochastic mode.

In order to determine ν_m, the electron temperature was derived for the pressure range from 10^{-3} Torr to 2×10^{-1} Torr, which includes two different pressure regimes experienced by the MRIT (low pressures and intermediate pressures) as calculated above for its specific dimensions. In the intermediate pressure range, the ratio of the sheath density to the center density is given by Equation 3.39 at the axial sheath edge and Equation 3.40 at the radial sheath edge.

For pressures below 6×10^{-3} Torr (low pressures), the chamber geometry is grossly approximated as an infinite cylinder geometry ($l \gg R$) where the ratio n_s/n_0 is known to be approximately 0.4 [6]. From the calculation of the effective plasma size, d_{eff}, given by Equation 3.38, the electron temperature as a function of pressure is derived from Figure 3.9, and the electron elastic collision rate constant, K_m, is determined from Figure 3.5. The derived electron–neutral momentum transfer frequency in argon as a function of pressure is shown in Figure 4.3. As an example, the neutral gas density for a 3.2 mTorr discharge at 298 K is equal to 1.03×10^{20} m^{-3}. The electron temperature can then be derived from the product $n_g d_{\text{eff}}$ as explained in 3.3.2. It is found to be approximately 7 eV, which is a high temperature for a low-pressure rf discharge [8]. For this value of T_e, the elastic electron–neutral collision rate constant is approximately equal to 3×10^{-13} m^3/s as seen in in Figure 3.5. The electron–neutral elastic collision frequency is then approximately equal to 3×10^7 s^{-1} ($\nu_m = n_g K_m$).

When operating at 13.56 MHz, the discharge is collisionless for pressures much less than 25 mTorr, and when operating at about 1.5 MHz, the collisionless pressure range occurs for pressures much lower than 1 mTorr.

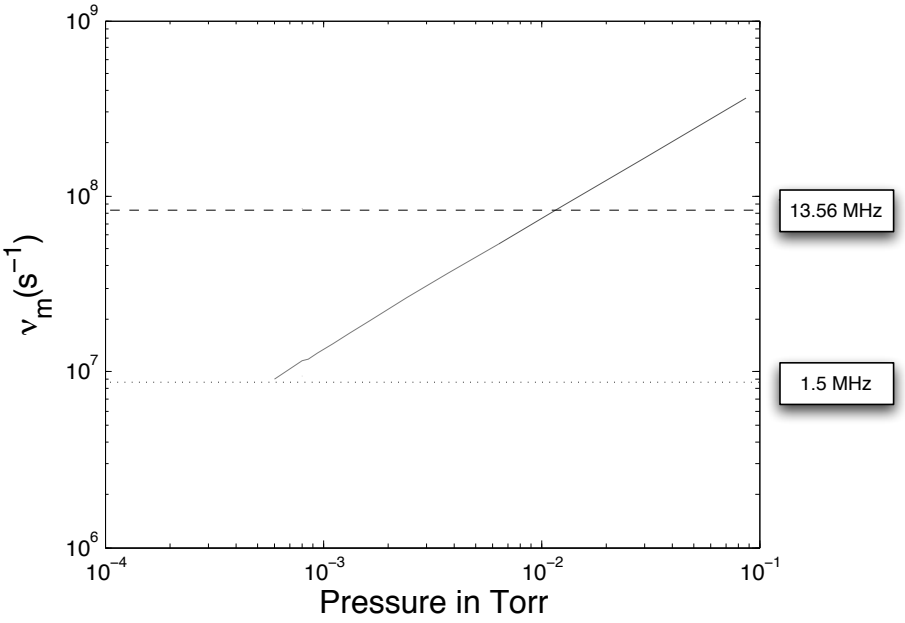

Figure 4.3. Electron–neutral momentum transfer frequency in argon as a function of pressure.

4.2 Initiation

An rf inductive discharge initially starts as a capacitive breakdown [6]. The characteristics of this breakdown can be classified by comparing the characteristic lengths of the discharge (discharge length, electron mean free path, oscillation amplitude of free electron or of drift electron) as detailed in Chapter 3.

The cylindrical MRIT was started at a miminum flow rate of 0.38 sccm, which corresponds to a chamber pressure of approximately 9×10^{-3} Torr, placing the MRIT in the intermediate pressure domain (*cf.* Figure 4.2). The MRIT was first tested at a frequency of 13.56 MHz, which falls in the collisionless regime. In this regime, the initiation is best described by a vacuum breakdown.

Decreasing the frequency of the discharge to about 1.5 MHz had the effect of

keeping the discharge in the collisional regime since, as shown in Figure 4.3, ν_m is always much greater than the operating frequency for the pressures considered. Maintaining the discharge in the collisional domain increases the discharge current and, therefore, the discharge efficiency. Experimental results confirm this result, as it was observed that, at frequencies close to 1.5 MHz, the discharge efficiency was increased compared to a similar discharge operated at 13.56 MHz [58].

4.3 E-to-H and H-to-E Transitions

4.3.1 Transferred Power

The total transferred power to the discharge is equal to the sum of the power transferred by the capacitive component of the discharge and the inductive component of the discharge, as described in Chapter 3. The expression of the total transferred power is given by Equation 3.76.

Figure 4.4 shows the total calculated transferred power as a function of the electron density at 50 mTorr and with a 0.3-A coil current with the dimensions: $R = 4.3$ cm, $d = 5$ mm, $l = 6$ cm, $H = 20$ cm, and $\mathcal{N} = 3$ turns. These values were taken to match the ones from Lee *et al.* [66]. Since the dielectric constant was not given, an average value for quartz was taken. Figure 4.5 shows the results derived by Lee *et al.* [66].

4.3.2 H-to-E transition

The H-to-E mode transition occurs at the local maximum of the inductively coupled power [66], i.e., for $\partial P_{\text{ind}}/\partial n_e = 0$. The transition density is then inversely

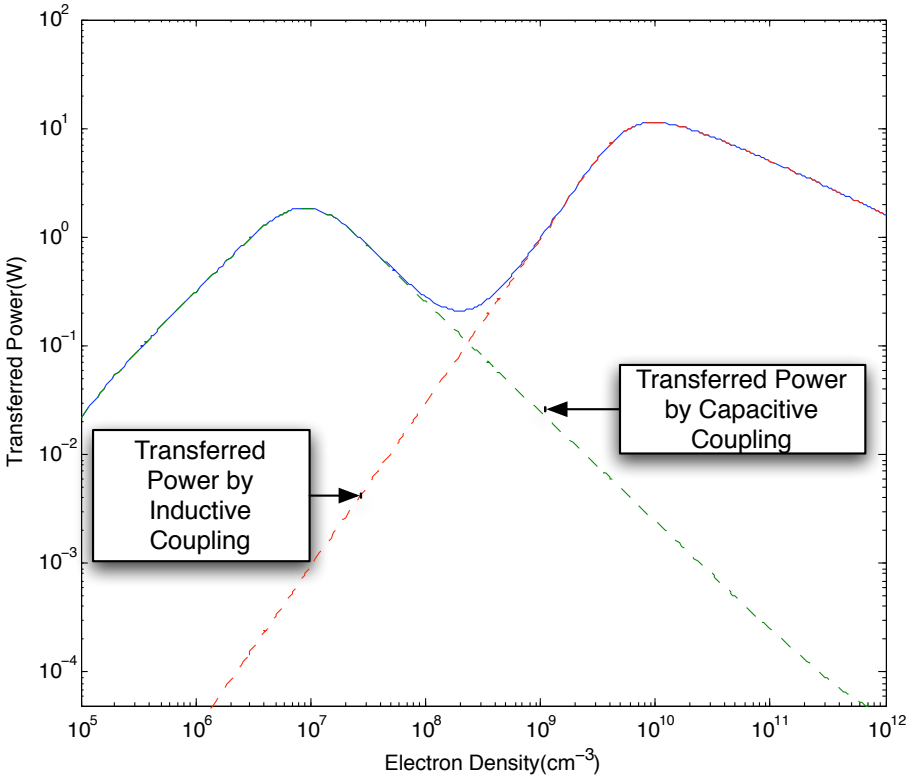

Figure 4.4. Calculated transferred power by capacitive and inductive coupling.

proportional to the square of the chamber radius and equal to

$$n_e = \frac{3}{2R^2}\frac{m}{e^2\mu_0}\left(1+\frac{\nu^2}{\omega^2}\right). \tag{4.1}$$

Our results for the transition density, shown in Figure 4.6 as a funciton of pressure and in Figure 4.7 as a function of radius, are in very good agreement with the transition from H-to-E derived by Lee *et al.* [66] from Equation 4.1.

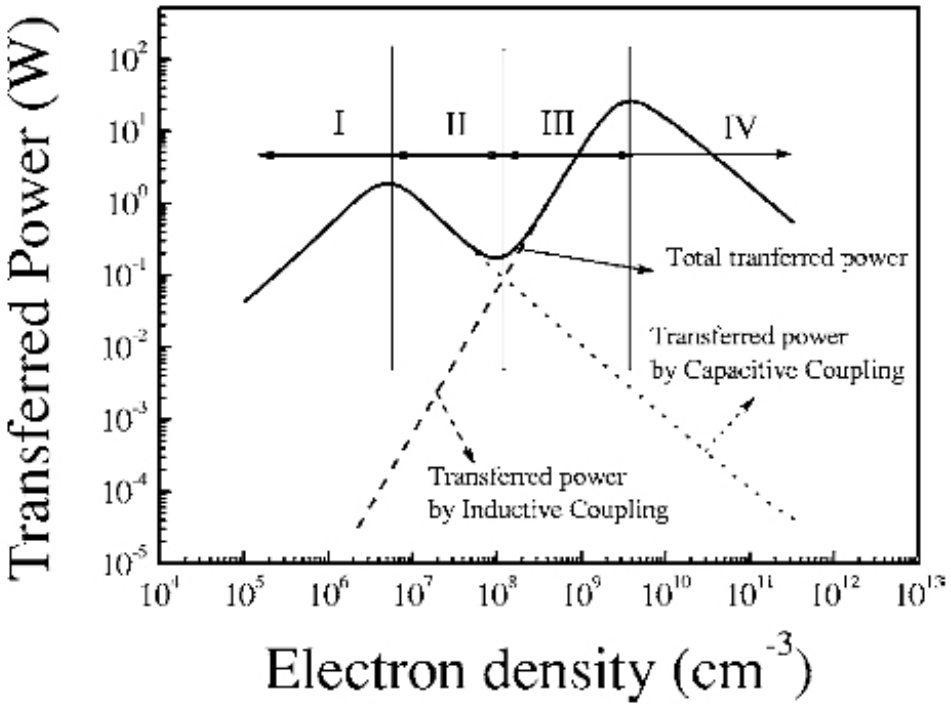

Figure 4.5. Calculated transferred power by capacitive and inductive coupling by Lee *et al.* [66].

4.3.3 E-to-H transition

The E-to-H transition is determined by equating the transferred power by inductive coupling to the transferred power by capacitive coupling [66]. The power transferred by capacitive coupling can be written as

$$P_{\text{cap}} \approx \frac{\pi R^2 l}{2} |J^2| \left(\frac{m\nu\omega_{pe}^4}{n_e e^2 \omega^4} \right) \left(\frac{\omega_{pe}^4}{\omega^4} + \frac{\nu^2}{\omega^2} \right)^{-1}, \tag{4.2}$$

and the inductive power is given by

$$P_{\text{ind}} \approx \frac{\pi \omega^2 \mu_0^2 \mathcal{N}^4 R^4 I^2}{16 l} \sigma_p^2, \tag{4.3}$$

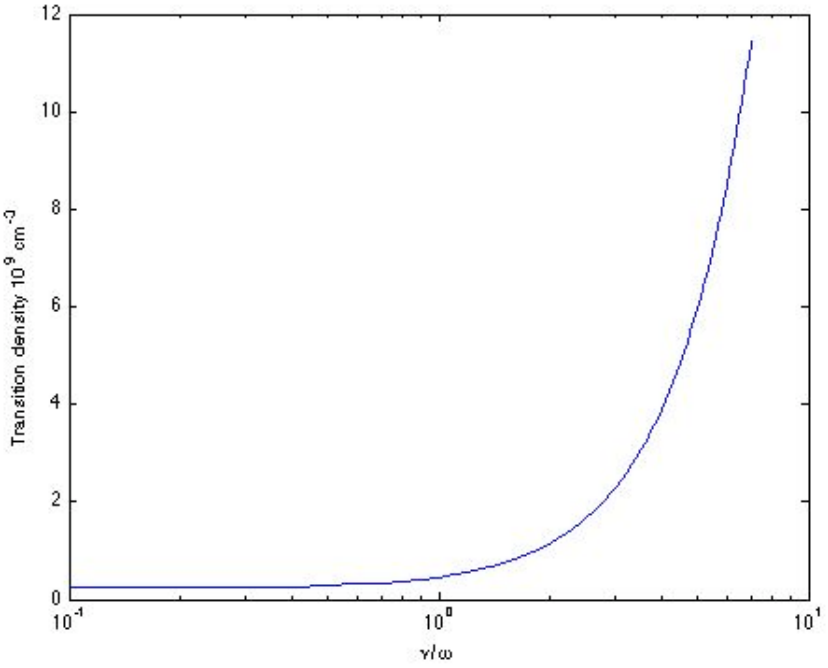

Figure 4.6. H-to-E transition density and power as a function of the pressure.

which gives us

$$n_e = \frac{A + \nu^2}{\omega^2(A - \omega^2)B^{1/2}}, \tag{4.4}$$

with $A = (8l^2|J^2|) / (\mu_0 \mathcal{N}^4 R^2 I^2 \epsilon_0^2)$, and $B = e^2/\epsilon_0^2$. Figure 4.8 shows the E-to-H transition density as a function of pressure for the same conditions as Lee *et al.* [66].

Figure 4.9 shows the E-to-H transition density as a function of radius for the same conditions as Lee *et al.* [66].

Our results in the E-to-H transition simulation differ approximately by a factor ten from the ones from Lee *et al.* [66]. However, they have provided no clear expression of the transition density from E-to-H mode used for their simulation.

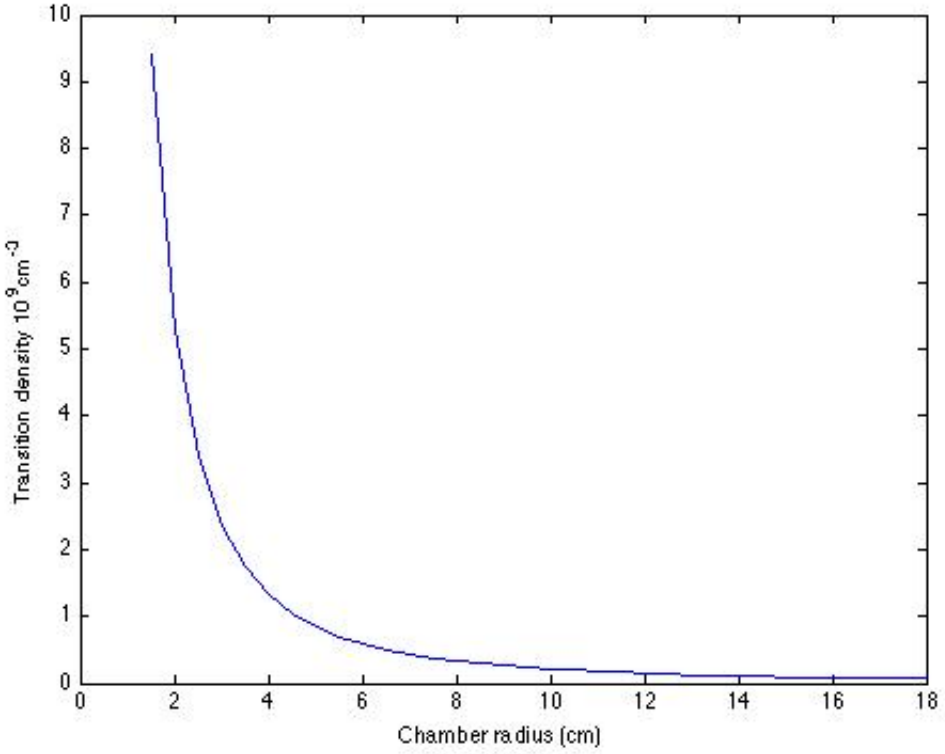

Figure 4.7. H-to-E transition density and power as a function of the chamber radius at a pressure $p = 50$ mTorr.

4.4 Non-Local Approach: Kinetic Modeling

4.4.1 System of Equations

As provided in greater detail in Chapter 3, a self-consistent set of equations for the description of the kinetic behavior of the plasma can be summarized as follows:

- The total current density equation

$$j = -\frac{em^{3/2}}{4\pi\sqrt{2}} \int f_{1s} v_y d^3 v, \tag{4.5}$$

where f_{1s} is the symmetric part of the EVDF given in Equation 3.79.

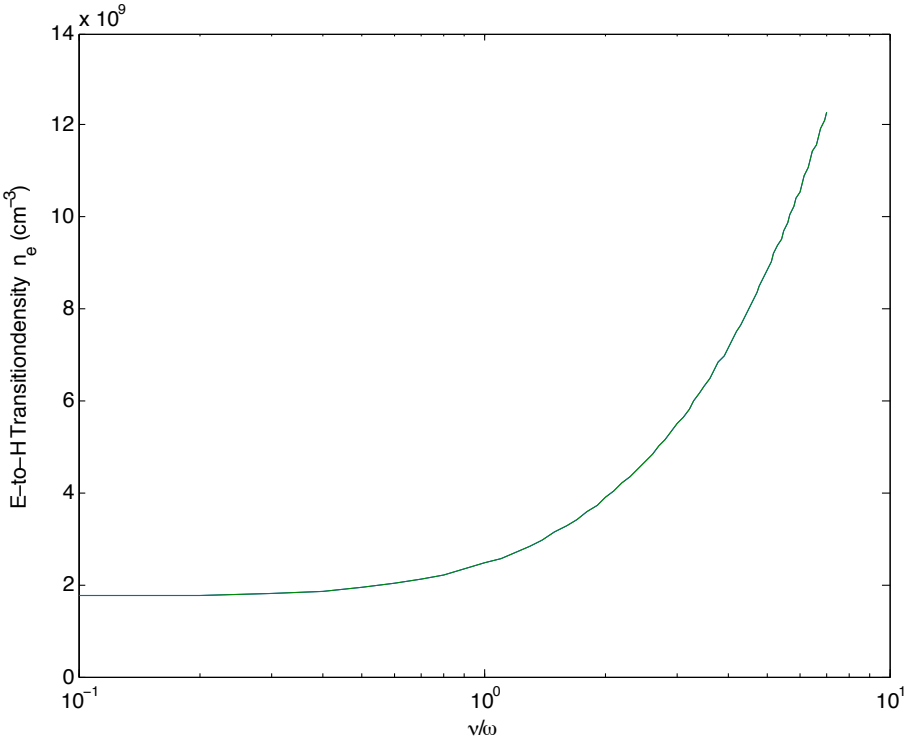

Figure 4.8. E-to-H transition density and power as a function of pressure.

- The equation in Kaganovich *et al.* [8] (their Equation 23) to be followed by the transverse rf electric field:

$$\frac{d^2E_y}{dx^2} + \frac{\omega^2}{c^2}E_y = -\frac{4\pi j\omega}{c^2}\left[j(x) + I\delta(x) - I\delta(x-L)\right] \tag{4.6}$$

  where I is the current in the coil at $x = 0$.

- The quasineutrality condition for the electrostatic potential in the form of a

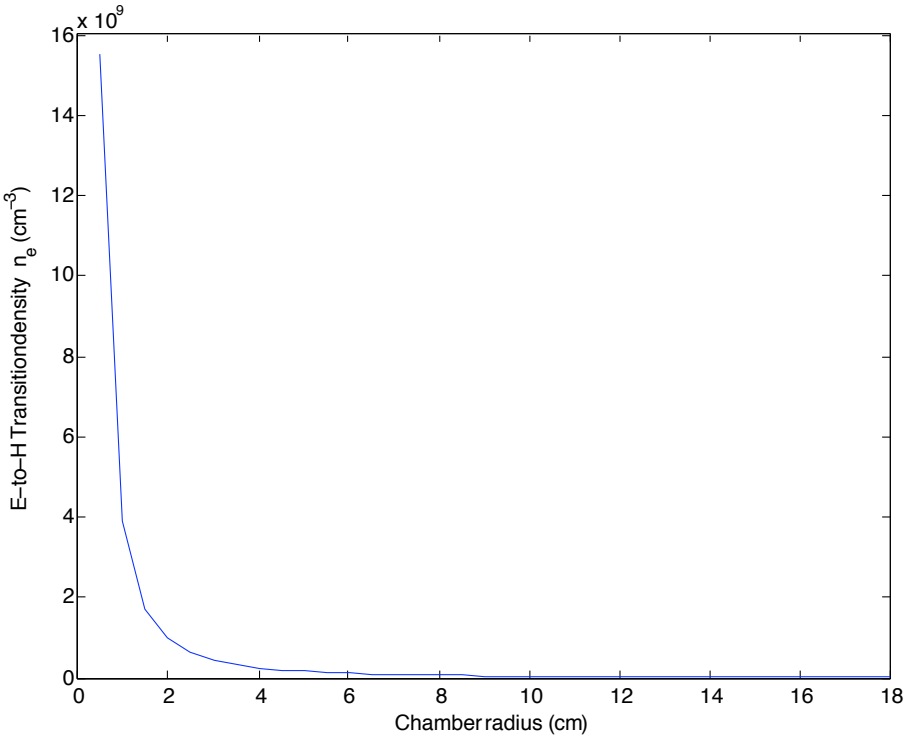

Figure 4.9. E-to-H transition density and power as a function of the chamber radius at pressure $p = 50$ mTorr.

differential equation:

$$\frac{d\phi}{dx} = -\mathrm{T}_e^{\mathrm{scr}}(x)\frac{d\ln[n_i(x)]}{dx}, \tag{4.7}$$

where $n_i(x)$ is the ion density profile. $\mathrm{T}_e^{\mathrm{scr}}(x)$ is the electron screening temperature given by

$$\mathrm{T}_e^{\mathrm{scr}}(x) = \left[\frac{1}{2n(x)}\int_{\phi(x)}^{\infty} f_0(\epsilon)\frac{d\epsilon}{\sqrt{\epsilon - \phi(x)}}\right]^{-1} \tag{4.8}$$

4.4.2 Method of for Solving Equations

4.4.2.1 Use of Fourier series

Assuming that the electric field can be described by a Fourier distribution, it can be written as:

$$E_y(x) = \sum \Xi_s \cos(k_s x), \tag{4.9}$$

where s is an integer and $k_s = (2s+1)\pi/L$ in our case of a cylindrical discharge.

The current density is given by the following:

$$j(x) = \frac{e^2}{2m} \sum \int \frac{\Gamma(\epsilon)}{\sqrt{\epsilon - \phi(x)}} \frac{E_{yn} \cos[n\theta(x)]}{jn\Omega_b - j\omega + \nu} d\epsilon. \tag{4.10}$$

Substituting Equation 4.9 into 4.6, integrating with the weight $2\cos(k_s x)/L$ over the region [0,L] and substituting the Equation 4.10 for the current density gives

$$j_s = \frac{e^2}{m} \frac{1}{(2s+1)\Omega_{bT}} \sum_{l=0}^{\infty} \Xi_l Z_{s,l}^{\text{gen}} \left(\frac{\omega + j\nu}{(2s+1)\Omega_{bT}} \right), \tag{4.11}$$

where $\Omega_{bT} = V_T \pi/L$ and the generalized plasma dielectric function, $Z_{s,l}^{\text{gen}}$, is given by:

$$Z_{s,l}^{\text{gen}}(\xi) = \sqrt{\frac{2}{m}} \frac{(2s+1)\pi\Omega_{bT}}{L} \sum_{n=-\infty}^{\infty} \int_0^{\infty} \frac{\Gamma(\epsilon)}{n\Omega_b(\epsilon) - (2s+1)\Omega_{bT}\xi} \frac{G_{s,n}(\epsilon) G_{l,n}(\epsilon)}{\Omega_b(\epsilon)} d\epsilon. \tag{4.12}$$

$G_{l,n}(\epsilon)$ is the temporal Fourier transform of $\cos(k_l x)$ given by

$$G_{l,n}(\epsilon) = \frac{1}{T} \left[\int_0^T \cos[k_l x(\tau)] \cos\left(\frac{\pi n \tau}{T} \right) d\tau \right]. \tag{4.13}$$

4.4.2.2 Implications of Maxwellian distribution asssumption

In cylindrical geometry, the temporal Fourier transform of $\cos(k_l x)$ becomes

$$G_{l,n}(\epsilon) = \frac{1}{2}\delta_{(2l+1),|n|}. \tag{4.14}$$

Assuming a Maxwellian distribution for the EEDF, the generalized plasma dielectric function can be simplified to

$$Z_{s,l}^{\text{gen}}(\xi) = \delta_{s,l} Z(\xi), \tag{4.15}$$

where $Z(\xi)$ is the standard plasma dielectric function given by

$$Z(\xi) = \pi^{-1/2} \int_{-\infty}^{\infty} \frac{\exp(-t^2)}{t-\xi} dt. \tag{4.16}$$

4.4.3 1-D Kinetic Modeling

4.4.3.1 Testing of model

As an initial step in the resolution of the complete system of equations, assuming a Maxwellian EEDF, the electromagnetic field is derived. In order to check this part of the code, geometry and electromagnetic parameters were set to match the ones from Kaganovich *et al.* [8] and Blevin *et al.* [77]. Figure 4.10 shows the comparative results for $\omega/\Omega_{bT} = 1.5$, $\nu/\Omega_{bT} = 0.3$, and $R\omega_p/c = 4.5$. Figure 4.12 shows the comparative results for $\omega/\Omega_{bT} = 1.5$, $\nu/\Omega_{bT} = 0.3$, and $R\omega_p/c = 3$. The electron temperature is $\mathrm{T}_e = 2.5$ eV and the electron density is $n_0 = 10^{12}$ cm^{-3}.

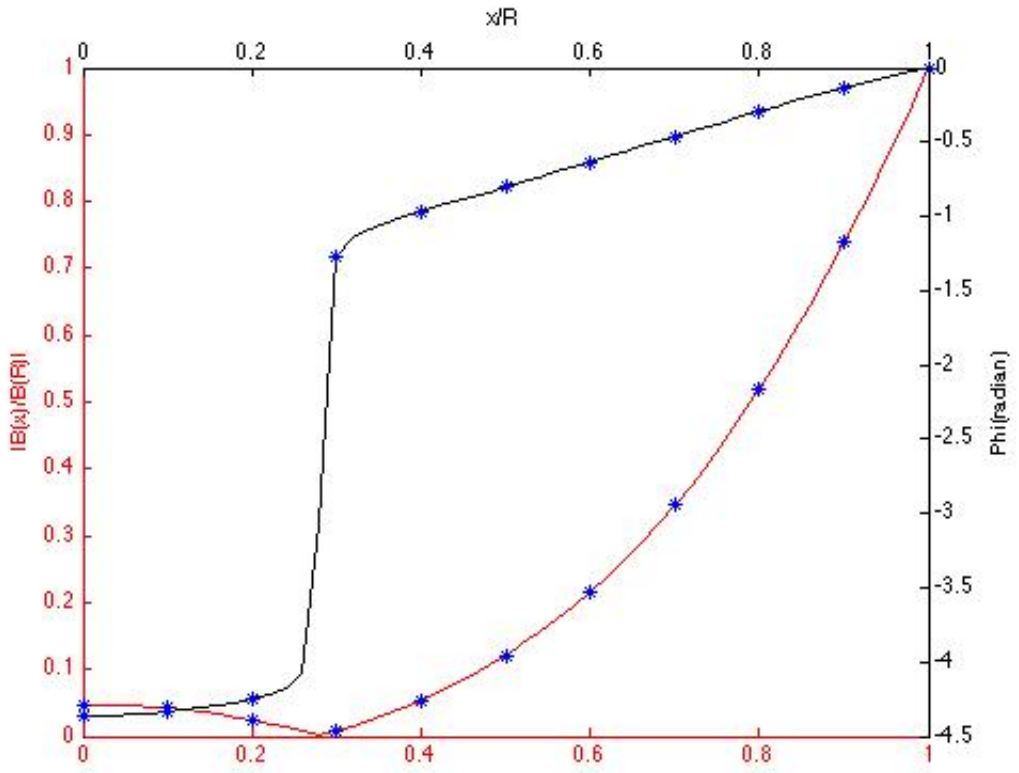

Figure 4.10. The normalized magnetic field amplitude for the case of a cylindrical-like geometry as function of the normalized coordinates x/R, where $R = L/2$, with $R\omega_p/c = 4.5$. Lines show the results from the present simulation and symbols are for results from [8] and [77].

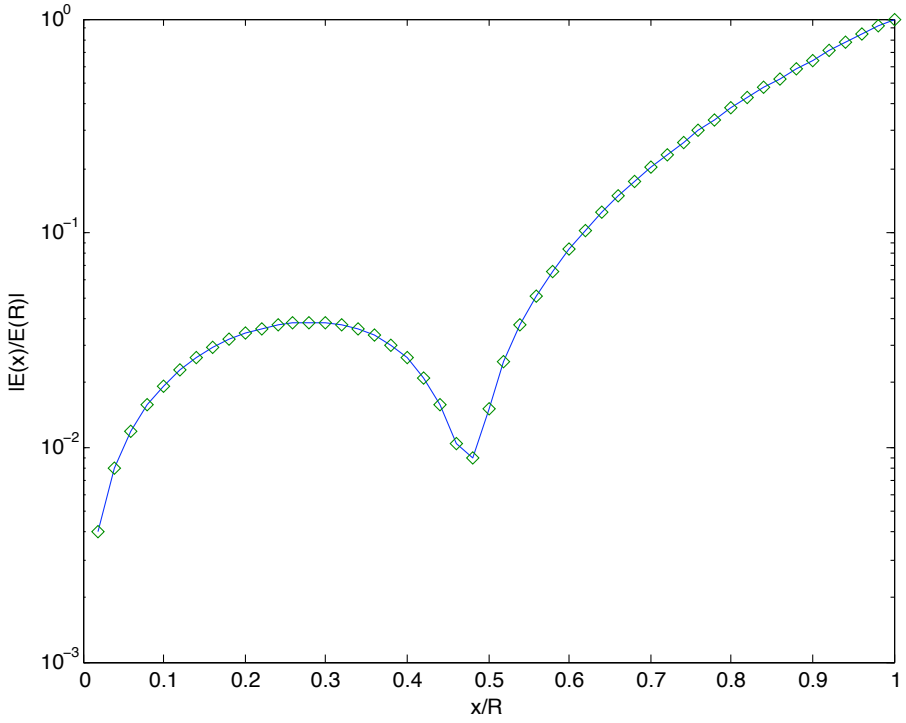

Figure 4.11. The normalized electric field amplitude for the case of a cylindrical-like geometry as function of the normalized coordinates x/R, where $R = L/2$, with $R\omega_p/c = 4.5$. Line shows the results from the present simulation and symbols are for results from [8].

Comparison between the normalized electric field results from Kaganovich *et al.* [8] with $R\omega_p/c = 4.5$ and our model are shown in Figure 4.11. In this particular case, we can observe a decrease of the rf field within the skin layer, as expected from normal skin effect concept, followed by a second decrease of the field amplitude expression of its anomalous behavior. This second field decay is the result of the superposition of the electric field induced by the coil and the electric field induced by the plasma discharge currents [52].

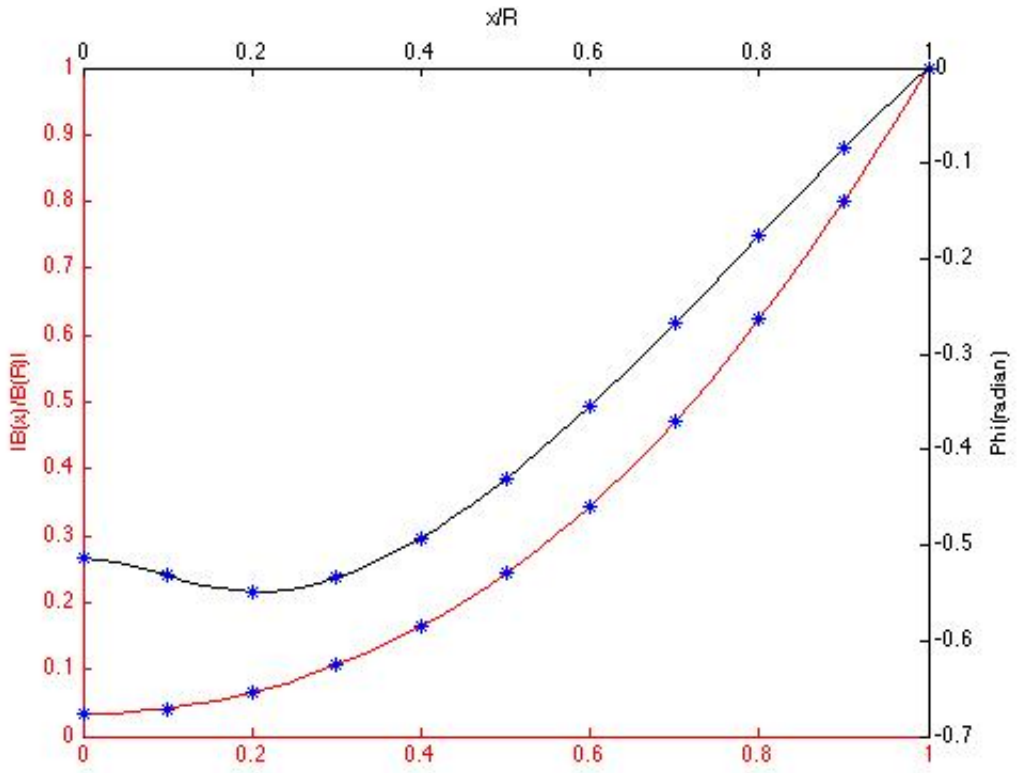

Figure 4.12. The normalized magnetic field amplitude for the case of a cylindrical-like geometry as function of the normalized coordinates x/R, where $R = L/2$, with $R\omega_p/c = 3$. Lines shows the results from the present simulation and symbols are for results from [77].

4.5 Summary

The main results presented in this chapter are:

- For a discharge chamber of the dimensions equal to those of the MRIT, a method to evaluate the collisional regimes as a function of pressure and frequency is presented. Applications of it are shown in Chapter 5. This is of particular interest given that the optimal pressures and frequencies for these types of thrusters have been so far only determined in an empirical manner.

- In the transition analysis, the conditions in which the E-to-H and H-to-E transitions occur are derived as a function of electron density. Results from this model are compared to published data [66]. The knowledge of the conditions of existence of the different coupling modes allows us, as shown in Chapter 5, to interpret the MRIT functioning mode.

- The 1-D kinetic model developed is validated on the data available in literature [8, 77].

Chapter 5

Application to Miniature Rf Ion Thrusters

In this chapter, the discharge within the MRIT is analyzed using either a local or a non-local approach depending on the discharge pressure conditions. From Figure 4.1 in Chapter 4, above 5×10^{-3} Torr the MRIT falls into the intermediate pressure regime, for which a local approach is sufficient to describe the discharge. We use a classic transformer model to represent the plasma, for which the fields and currents are coupled through Ohm's law. However, below 5×10^{-3} Torr, the use of a non-local approach becomes necessary [8, 49]. Thrust calculations are also performed for different parameters as well as estimates of the performance of the thruster.

5.1 Transformer Model

5.1.1 Matching Network Calculations

The values of the capacitors C_1 and C_2 for different source powers are calculated from the matching network model described in Chapter 3. C_1 is derived from

$$C_1 = -\frac{1}{\omega X_1}, \tag{5.1}$$

with

$$X_1 = (R_s R_T - R_s^2)^{1/2} - X_s. \tag{5.2}$$

Figure 5.1 shows the capacitor C_1 as a function of the electron temperature and, therefore, the pressure, for a 15-W-absorbed-power discharge at 13.56 MHz and at 1.5 MHz. R_T is the Thévenin equivalent source resistance equal to 50 Ω and ω is the coil operating frequency. The source resistance, R_s, is derived from Equation 3.56. C_2 is derived from:

$$C_2 = \frac{1}{\omega}\frac{X_1 + X_s}{R_s^2 + (X_1 + X_s)^2}. \tag{5.3}$$

The C_2 values for a 15-W-absorbed-power discharge were derived for two different operating frequencies, 13.56 MHz, and 1.5 MHz ,and are shown in Figure 5.2.

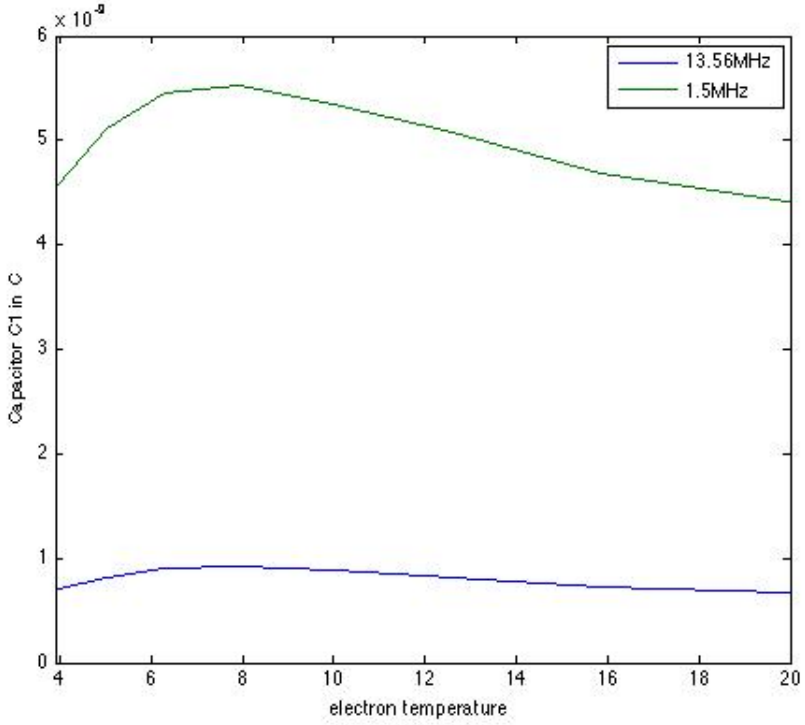

Figure 5.1. Calculated values of C_1 as a function of T_e for a 15-W discharge at 13.56 MHz and 1.5 MHz.

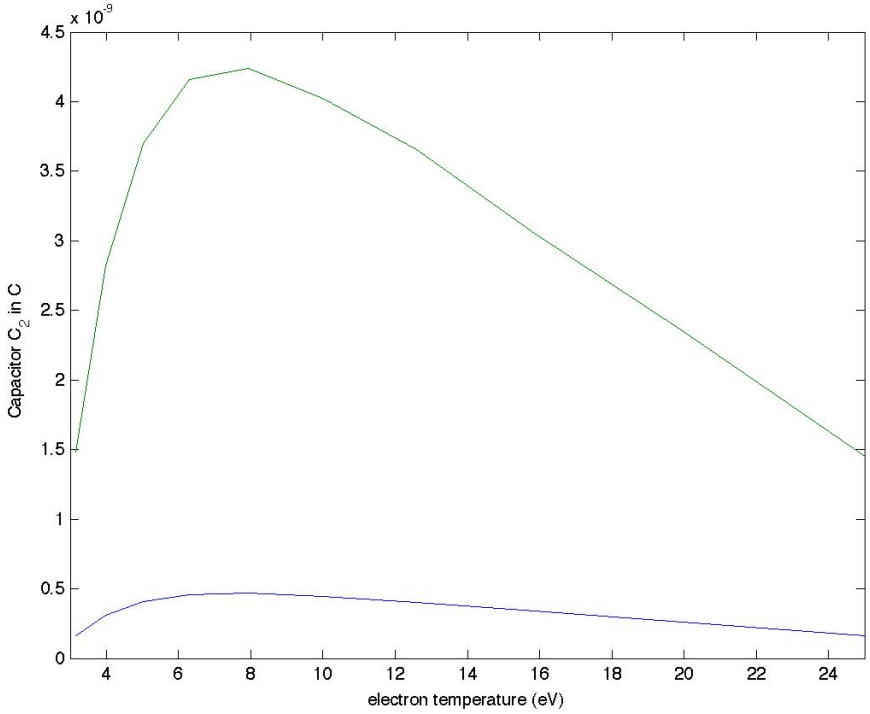

Figure 5.2. Calculated values of C_2 as a function of T_e for a 15-W discharge at 13.56 MHz and 1.5 MHz.

5.1.2 Transformer Model

From the equivalent transformer model, described in detail in Chapter 3, calculations of the plasma resitance and plasma inductance are performed, as well as an estimate of the source inductance and resistance. These calculations are used in the next section in order to determine values of the capacitors needed for the matching network. The plasma inductor is given by

$$L_s \approx \frac{\mu_0 \pi R^2 \mathcal{N}^2}{l} \left(\frac{b^2}{R^2} - 1 \right). \tag{5.4}$$

For a dielectric thickness of 2 mm, with a discharge radius of 5 mm and a discharge length of 1 cm, the calculated value of L_s for a 3-turn coil is 17.3 µH. The plasma resistance is given by

$$R_s \approx \mathcal{N}^2 \frac{\pi R}{\sigma_{\text{eff}} l \delta_p}. \tag{5.5}$$

Figure 5.3 and Figure 5.4 show the results of the transformer model in terms of sheath density and plasma resistance as a function of the absorbed power for different pressures. Figure 5.5 shows the collisional skin depth calculated for the MRIT dimensions. We can see that the skin depth is always larger or on the order of the MRIT size. Figure 5.6 and Figure 5.7 show that above 7×10^9 cm^{-3} density the discharge is mainly inductively driven in the MRIT.

5.2 Transition Model Results for the MRIT

Figure 5.8 shows the transition from a H-mode to the E-mode for a 13.56-MHz discharge and Figure 5.9 shows a similar transition for a 1.5-MHz discharge.

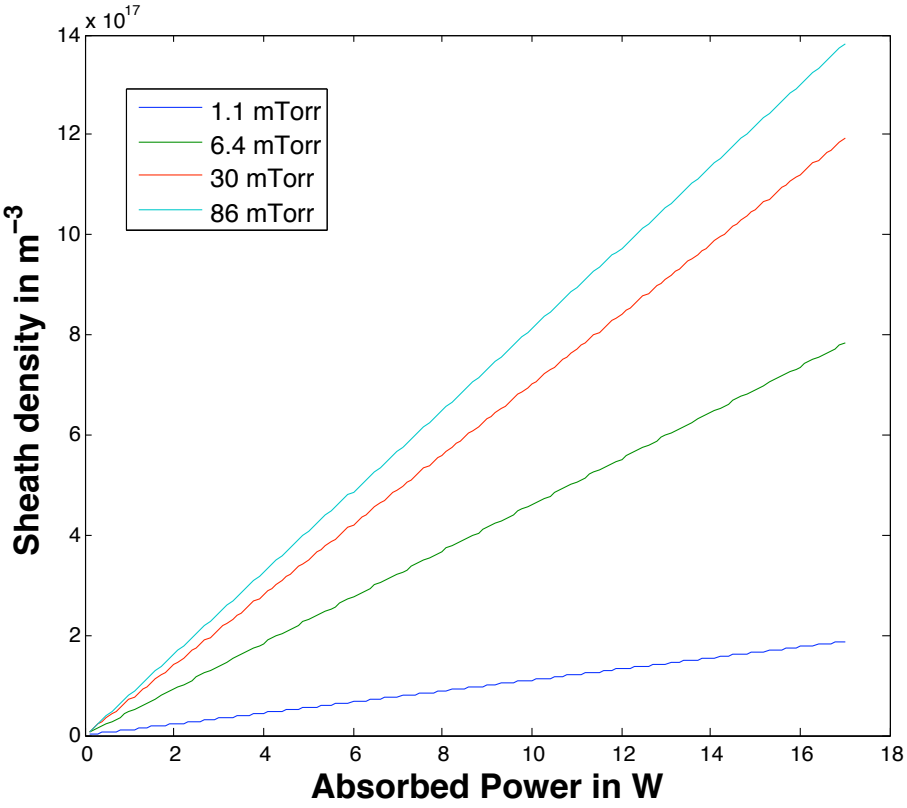

Figure 5.3. Sheath density as a function of absorbed power for different pressures.

5.3 Non-Local Model of the MRIT

The non-locality parameter, Λ, was calculated as a function of pressure for a 1.5-MHz discharge. Figure 5.10 shows the results of this derivation. In the pressure range were the MRIT was experimentally tested and run, the non-locality approximation is always valid ($\Lambda \gg 1$) at such a frequency. Λ was also derived for a pressure of 3 mTorr as a function of frequency and results are shown in Figure 5.11. It can be seen in this figure that, when the discharge frequency is about 1.5 MHz, $\omega/\nu \sim 0.35$ and $\Lambda \sim 14$, whereas for a 13.56-MHz discharge, $\omega/\nu \sim 3$ and $\Lambda \sim 4$. We can then conclude that the non-locality effect is much less pronounced

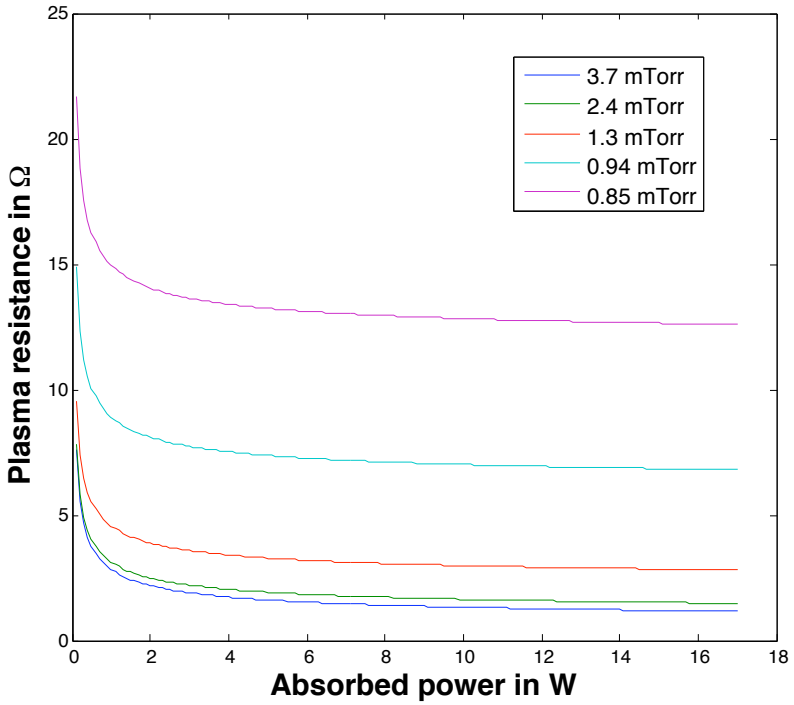

Figure 5.4. Discharge resistance as a function of absorbed power for different pressures.

at 13.56 MHz than at 1.5 MHz.

5.4 Non-Locality Parameter Derivation for the MRIT

The magnetic fields in the MRIT were calculated using the kinetic model described in Chapter 3 and validated in Chapter 4 using results from Blevin [77] and Kaganovich *et al.* [8]. The total current density was derived via

$$j_d(x) = \frac{n_e e^2}{m v_e} \sum_n \frac{\alpha_n}{n\pi/(2R)} \cos\left(\frac{n\pi x}{2R}\right) Z(\xi), \tag{5.6}$$

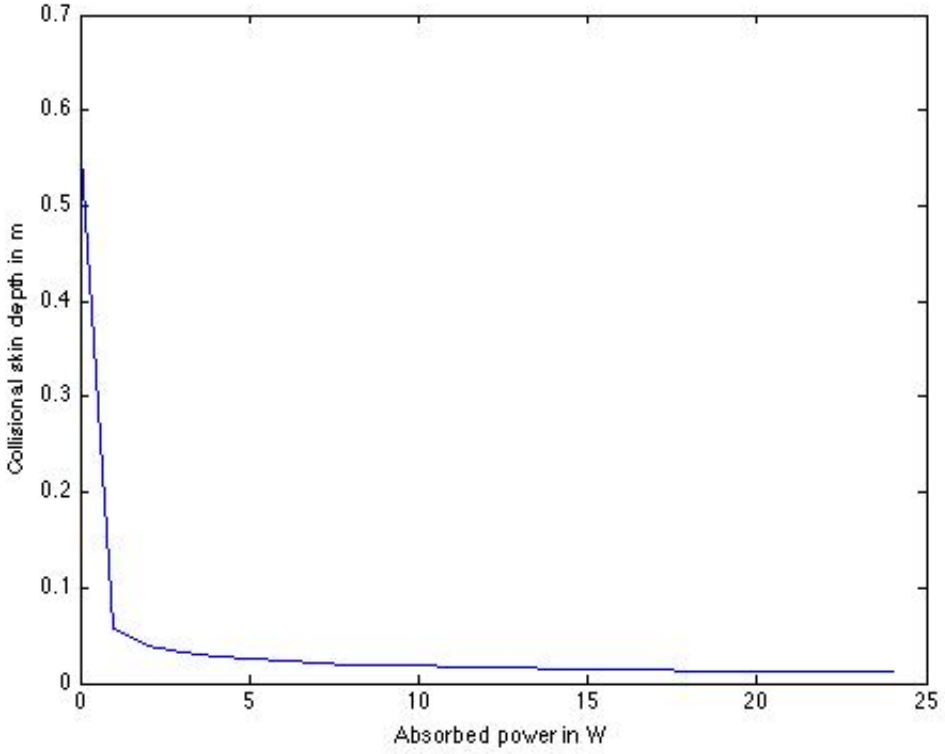

Figure 5.5. Collisional skin depth.

where $Z(\xi)$ is the plasma dispersion function given by

$$Z(\xi) = -\frac{2\xi}{\pi^{1/2}} \int_0^\infty \frac{\exp(-\beta^2)}{\xi^2 - \beta^2} d\beta, \tag{5.7}$$

where β is the ratio of the electron velocity over the most probable electron speed, $(2k\mathrm{T}_e/m)^{1/2}$.

The total electron current, I_a, was then determined by integration of the ionization chamber exit surface. Equating the electron current leaving the volume to the ion current leaving the volume (not taking electron backstreaming into account), I_a is then equal to sum of the screen current, I_s, the Bohm current to the wall, I_w,

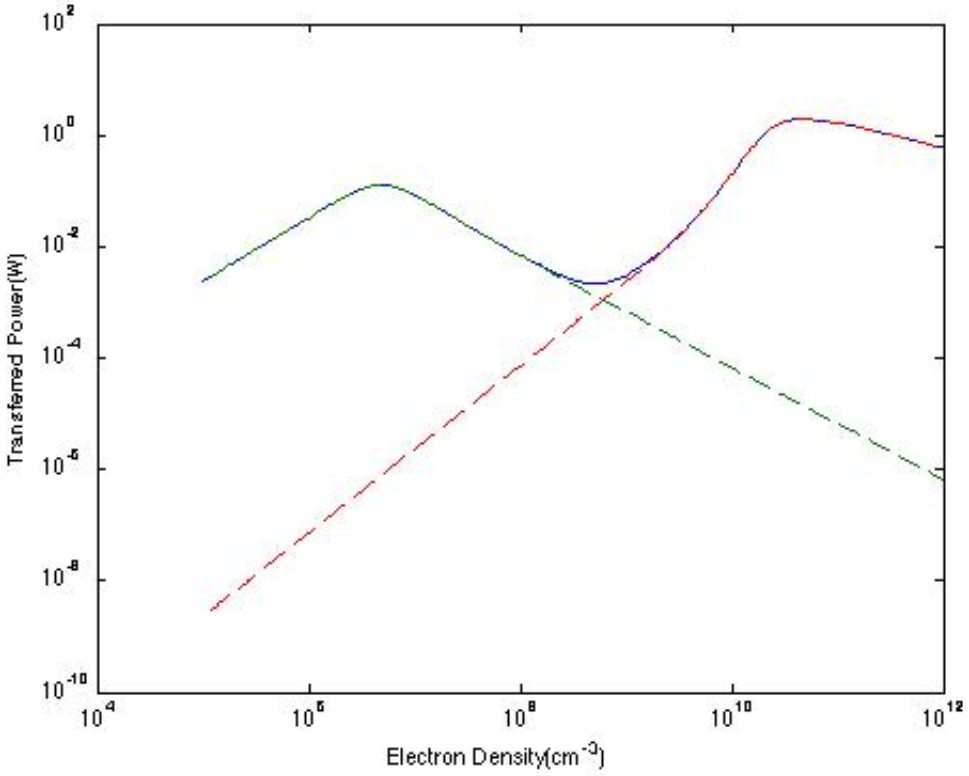

Figure 5.6. Calculated transferred power by capacitive and inductive coupling for the MRIT.

and the ion beam current, I_b [12], i.e.,

$$I_a = I_s + I_w + I_b. \tag{5.8}$$

The screen current is related to the ion beam current as follow

$$I_s = \frac{1 - T_s}{T_s} I_b, \tag{5.9}$$

where T_s is the screen transparency. The Bohm current to the wall area, I_w, is also related to I_b as

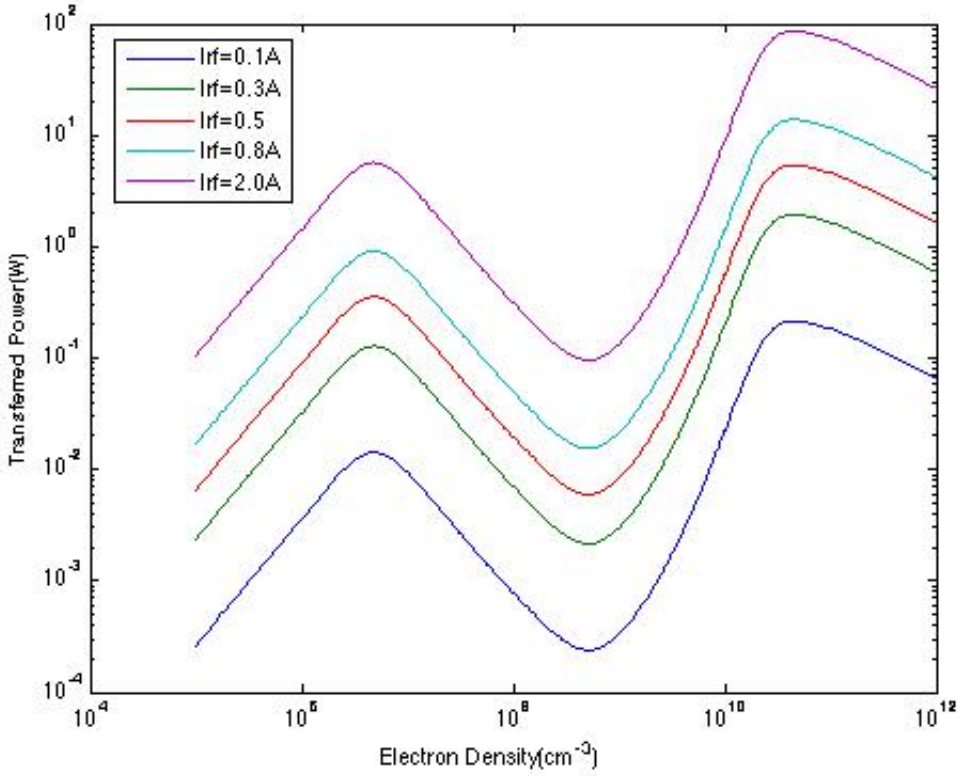

Figure 5.7. Calculated transferred power by capacitive and inductive coupling for different coil currents.

$$I_w = I_b \frac{A_w f_c}{A_s T_s}, \tag{5.10}$$

where A_w is the wall area, f_c is the confinement factor to the wall, and A_s is the screen area.

5.4.1 Total current density and ion beam current density for different frequencies

Figure 5.12 shows the magnetic field for a 2-W absorbed power discharge. The field fully penetrates the plasma, as expected with calculation results of the skin

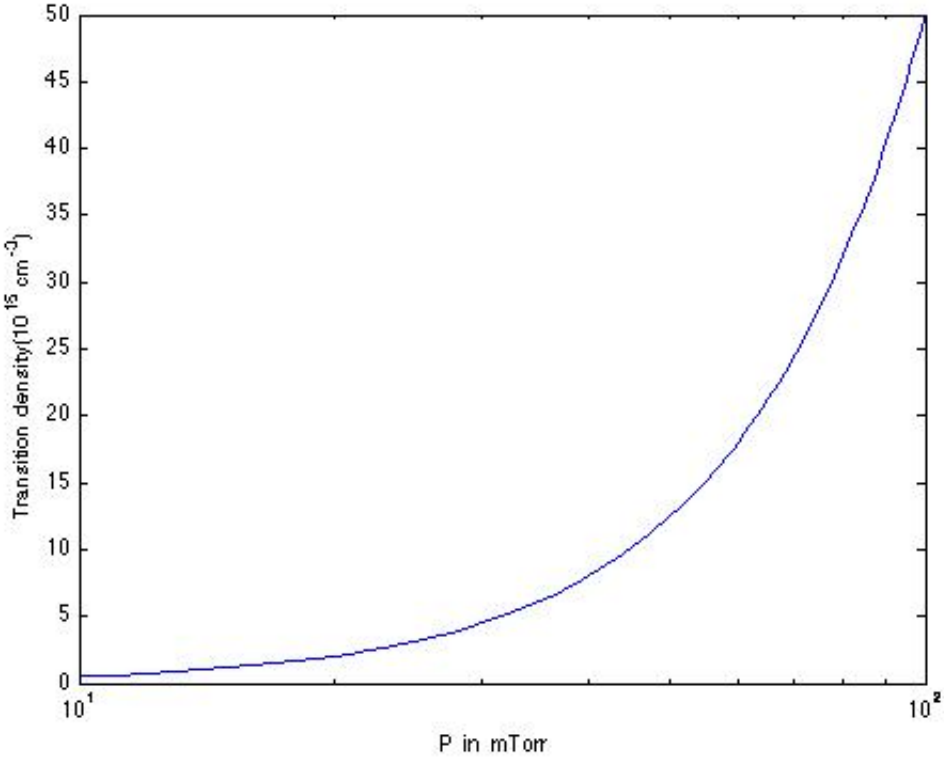

Figure 5.8. H-to-E transition density and power as a function of the pressure for a 13.56-MHz discharge in the MRIT.

depth (greater than the size of the thruster).

Figure 5.13 shows the total current density coming out of the discharge for different absorbed powers. Figure 5.14 shows the ion current density coming out of the discharge. As previously seen for the case of the 13.56-MHz discharge, the magnetic field, shown in Figure 5.15, does not seem to be affected by the presence of the plasma, contrary to the results we obtained in Chapter 4 (Figure 4.11) while testing our code. This is consistent with the fact that the skin depth is much greater than the size of the thruster, 1 cm, and therefore the field fully penetrates the plasma.

Figure 5.16 and Figure 5.17 show the total current density coming out of the

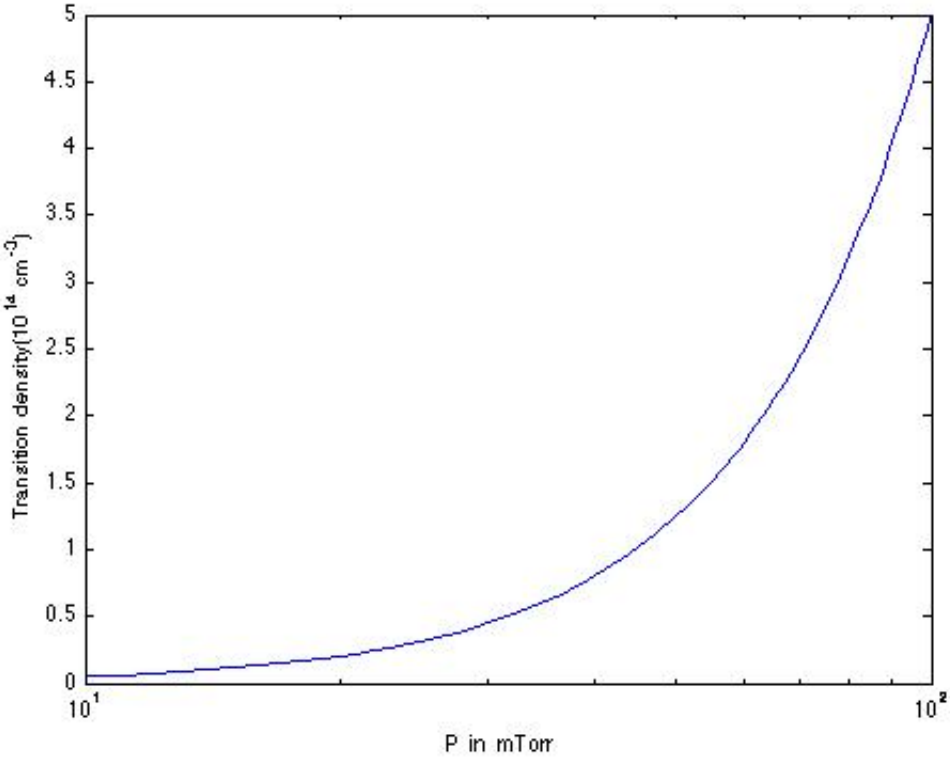

Figure 5.9. H-to-E transition density and power as a function of the pressure for a 1.5-MHz discharge in the MRIT.

discharge for an 8-MHz discharge and an 1.5-MHz discharge, respectively, for different absorbed powers.

Figure 5.18 and Figure 5.19 show the ion current density coming out of the discharge for an 8-MHz discharge, and a 1.5-MHZ discharge, respectively.

The values of the beam current obtained are of the order of the experimental ones obtain for the MRIT [58]. Figure 5.20 shows the measured beam current in the MRIT for a 15-W discharge at 1.5 MHz and the non-local model results for a 15-W-absorbed-power discharge at 1.5 MHz for a screen transparency, T_s, of 0.9 and a confinement factor, f, of 0.1.

Figure 5.22 shows the total beam current as a function of the absorbed power

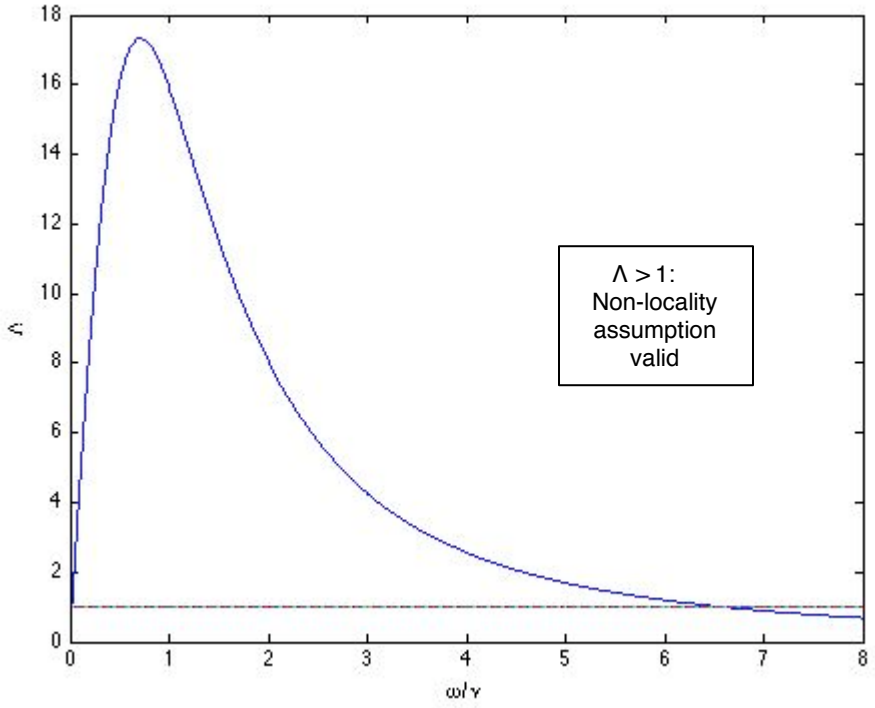

Figure 5.10. Non-locality parameter for the MRIT at 3 mTorr versus ω/ν.

for different frequencies. Figure 5.22 shows the ion beam current as a function of the absorbed power for different frequencies.

5.5 Space Propulsion Applications

5.5.1 Thrust Calculations

The thrust is determined using the following equation

$$T = \gamma \sqrt{\frac{2M}{q}} I_b \sqrt{V_b}, \tag{5.11}$$

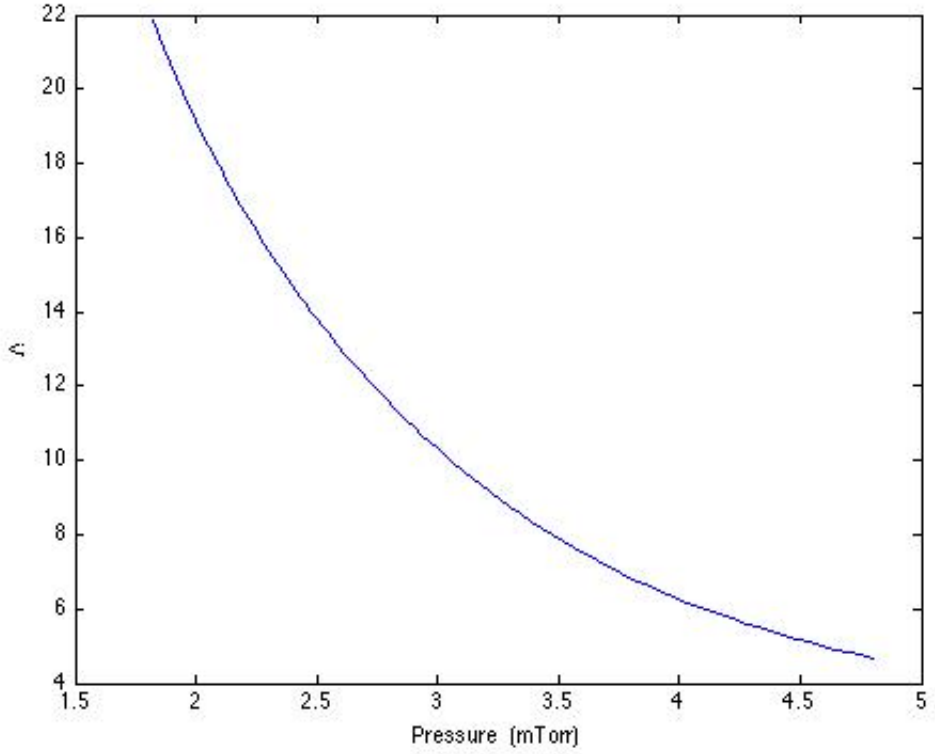

Figure 5.11. Non-locality parameter for a 1.5-MHz discharge in the MRIT versus pressure.

where γ is the total thrust correction given by Equation 3.87 and q is the mean ion charge, which, assuming 1% of the ionized ions are Xe^{++} ion, is equal to $1.02e$ [1]. The parameter α_T is the thrust correction factor for thrust in the presence of doubly ionized atoms and F_t is the correction to the force due to the effective thrust-vector angle given by Equation 3.88.

Thrust is shown in Figures 5.23, 5.24, and 5.25. As expected, the values of thrust decrease as the screen transparency decreases. The MRIT was found experimentally to have a maximum thrust of 50 mN for a 1.5-MHz discharge and a maximum power of 15 W. This would imply a high screen transparency (between 0.7 and 0.9), which in turn implies a low confinement factor. Also higher thrust

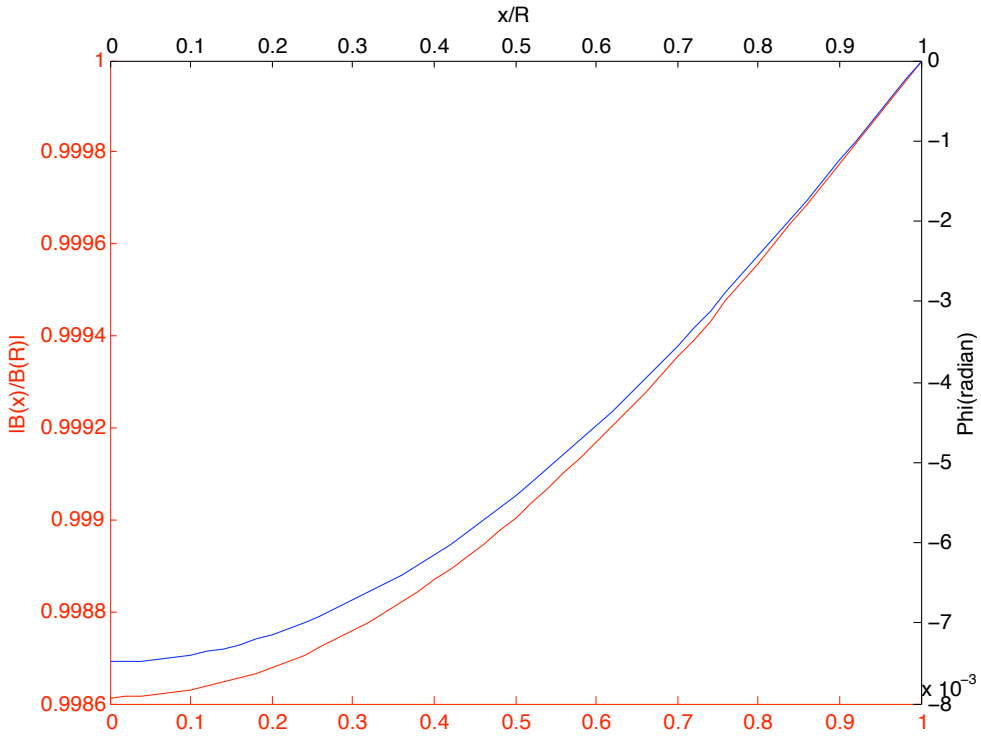

Figure 5.12. *B* field as a function of radius as in an argon discharge in the MRIT for 13.56 MHz and 2-W absorbed power.

levels are obtained at frequency of 1.5 MHz versus 13.56 MHz, as seen experimentally with the MRIT. However, contrary to the empirical predictions from Loeb *et al.* [1], an 8-MHz discharge does not seem to be more efficient. Derivations, using this non-local model, at several other frequencies would be the next step to predict a optimum discharge frequency for the MRIT.

It can be seen in Figure 5.23 that, for a 1.5-MHz discharge at 15 W absorbed, the calculated thrust from our model is approximately 60 µN, which gives an I_{sp} of approximately 5700 s. The value determined from experimental results for the same frequency and power is 5480 s, with which our model is in good agreement.

In order to analyze the "plateau" that seems to occur in the beam current plots

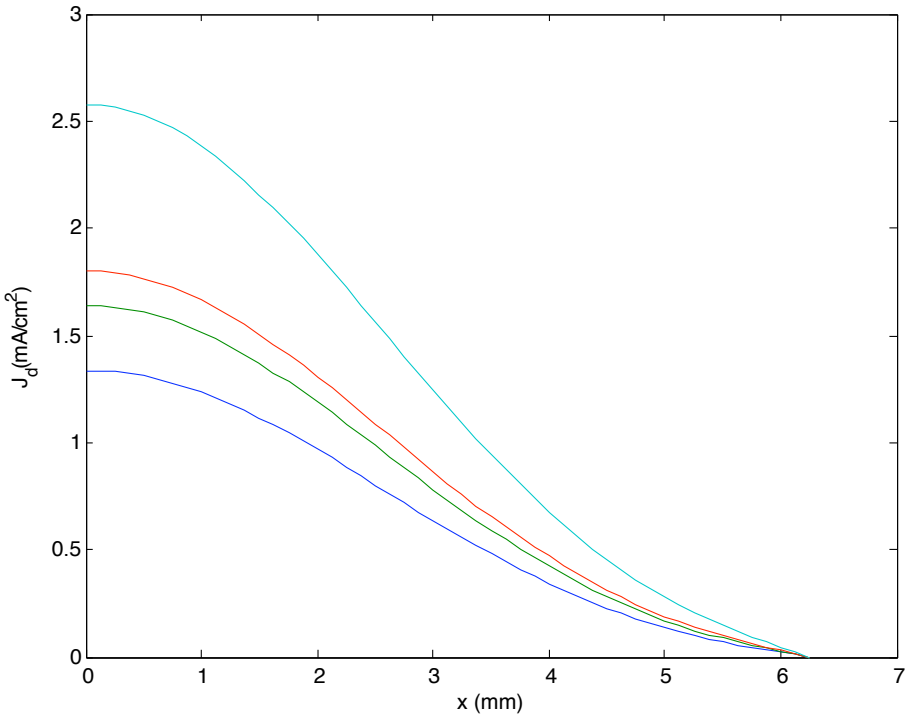

Figure 5.13. Total current density as a function of radius in an argon discharge in the MRIT for 13.56-MHz for different absorbed powers.

as a function of power, more absorbed power points were used to derive Figure 5.26 for a 13.56-MHz discharge. In this plot, there is still a plateau in the beam current and another sharp increase as a function of the absorbed power. In order to evaluate the effect of non-locality on this stagnation, the non-locality parameter as a function of the absorbed power for the same conditions was derived and shown here in Figure 5.27. In this plot, Λ reaches a maximum around 4 W, then decreases sharply until about 10 W, at which point the slope of the decrease changes and lessens. On the beam current plot (Figure 5.26), it is also approximately between 4 and 10 W that the slowing down in the current production rate occurs.

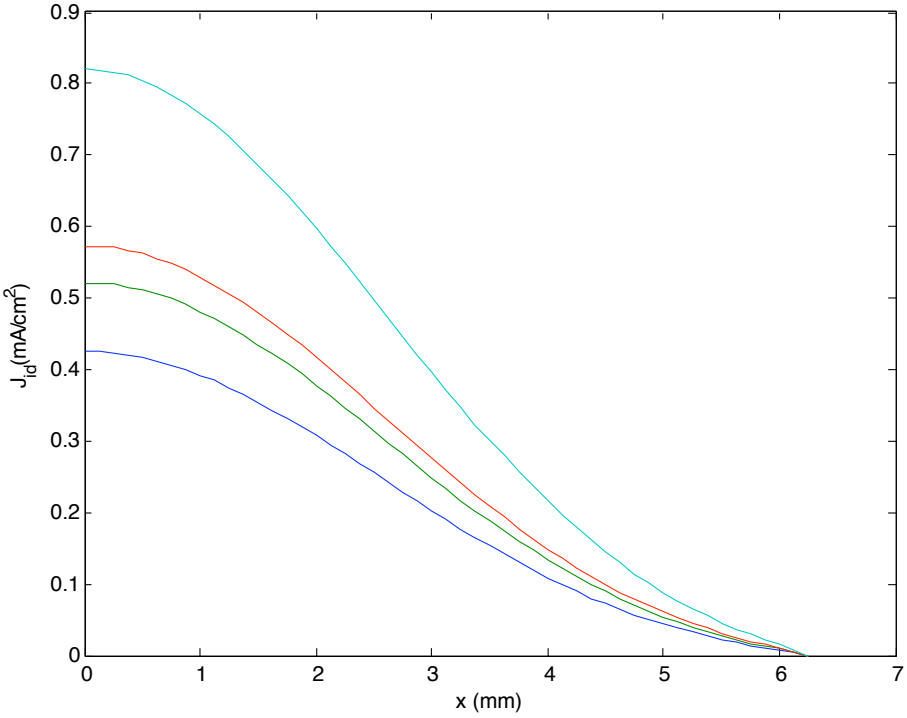

Figure 5.14. Ion current density as a function of radius in an argon discharge in the MRIT for 13.56-MHz for different absorbed powers.

5.5.2 Comparison with RIT-series estimates

Table 5.1 presents some of the thruster operational characteristics predicted from the larger scale rf ion thruster RIT–10 results by Feili *et al.* using empirical scaling laws [1] and experimental values for the MRIT [57].

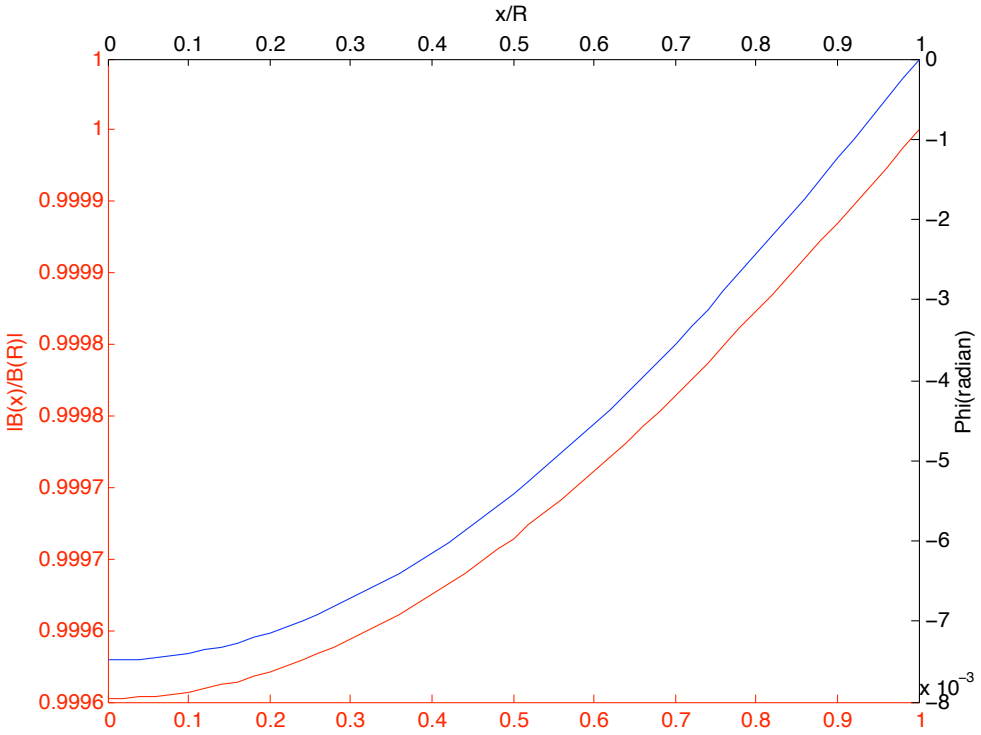

Figure 5.15. B field as a function of radius as in an argon discharge in the MRIT for 8 MHz and 2-W absorbed power.

Table 5.1. Discharge characteristics predictions based on empirical scaling laws [1].

	RIT-4	**RIT-2**	**RIT-1**	**MRIT**
ionizer diameter (cm)	4	1.9	1.25	1
extraction system diameter (cm)	3.1	1.2	0.65	1
number of beamlet holes	151	19	7	7
discharge vessel length (cm)	2.9	1.9	1.5	1.25
number of rf-coil turns	6	4	3	4
rf-frequency (MHz)	2.5	5	8	1.5
discharge pressure (mTorr)	1	2.1	3.2	3
nominal thrust (mN)	2.5	0.35	0.1	0.022
ion beam current (mA)	44.4	6.2	1.8	0.75
discharge power (W)	26	5.9	2.15	N/A
total thruster input power (W)	81.9	13.7	4.41	10–15

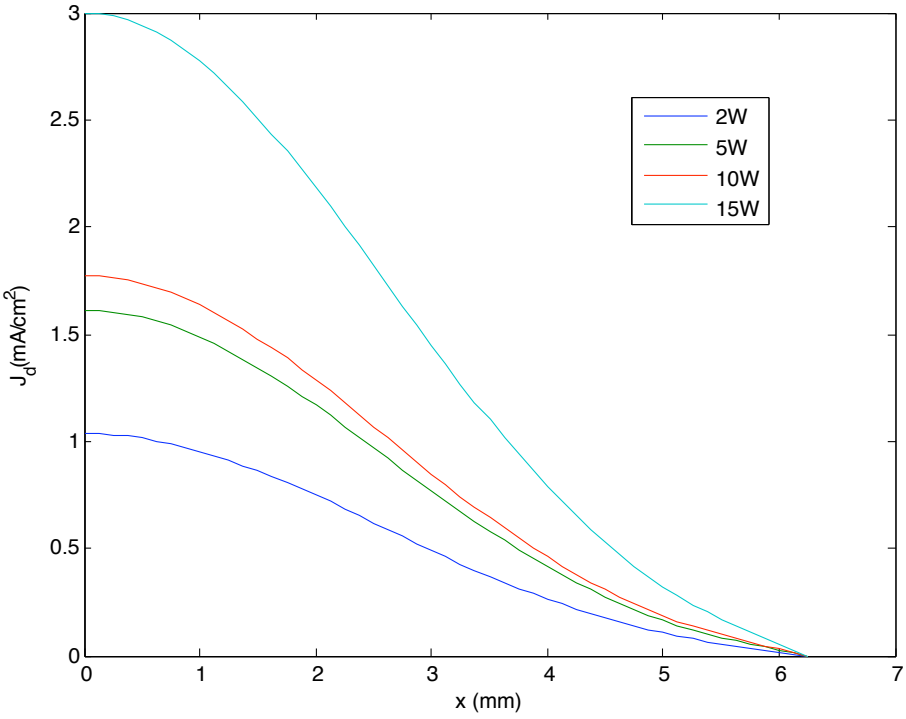

Figure 5.16. Total current density as a function of radius in an argon discharge in the MRIT for 8 MHz for different absorbed powers.

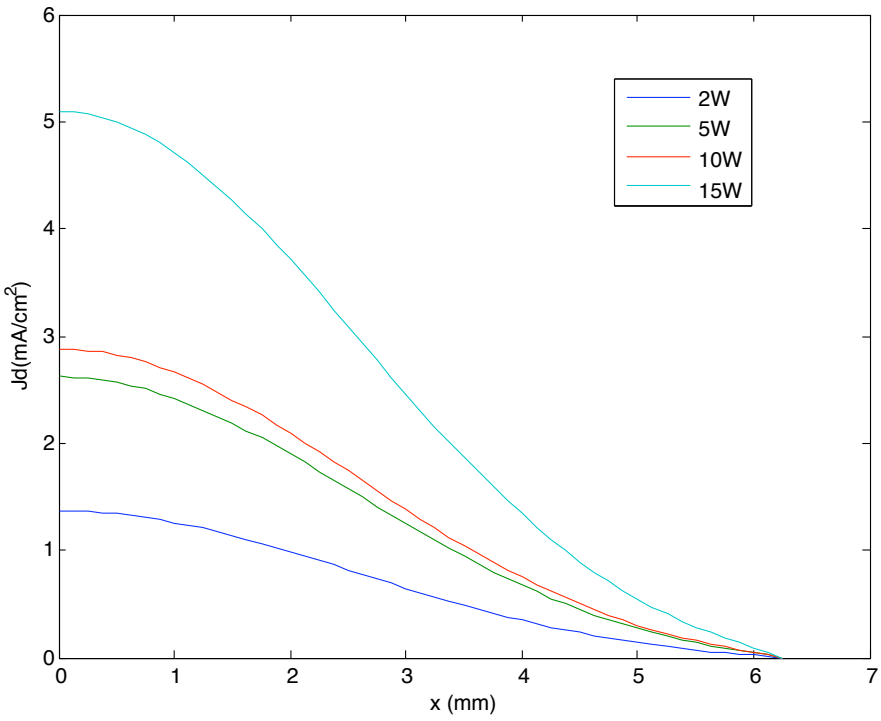

Figure 5.17. Total current density as a function of radius in an argon discharge in the MRIT for 1.5 MHz for different absorbed powers.

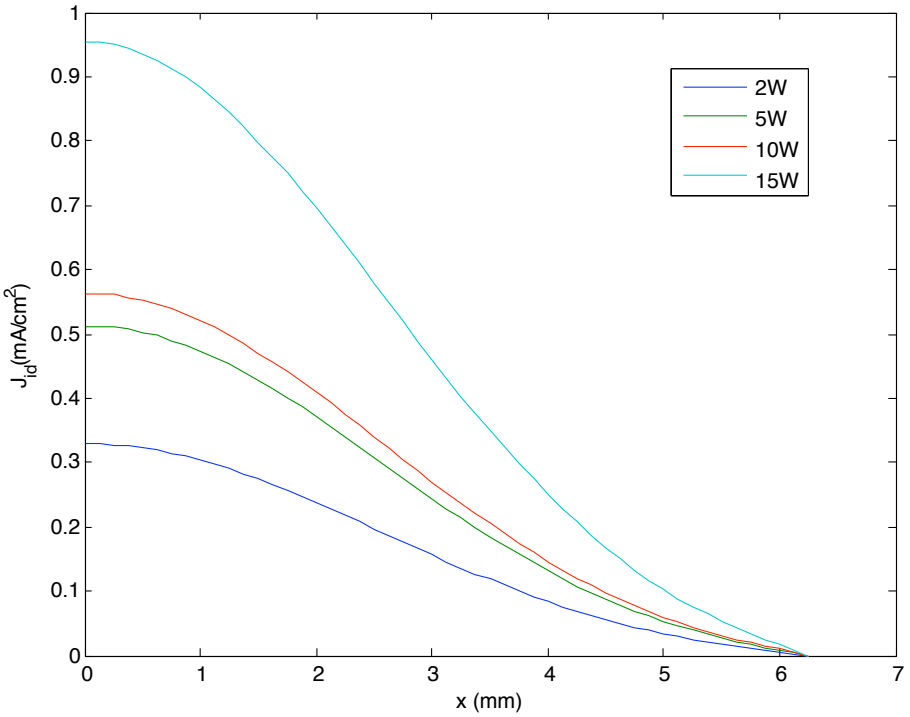

Figure 5.18. Ion current density as a function of radius in an argon discharge in the MRIT for 8 MHz for different absorbed powers.

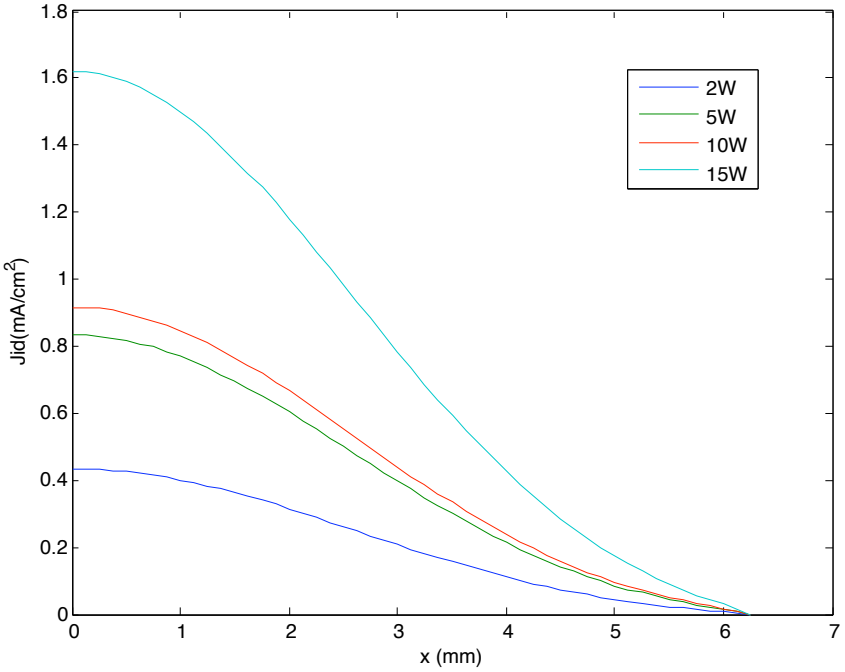

Figure 5.19. Ion current density as a function of radius in an argon discharge in the MRIT for 1.5 MHz for different absorbed powers

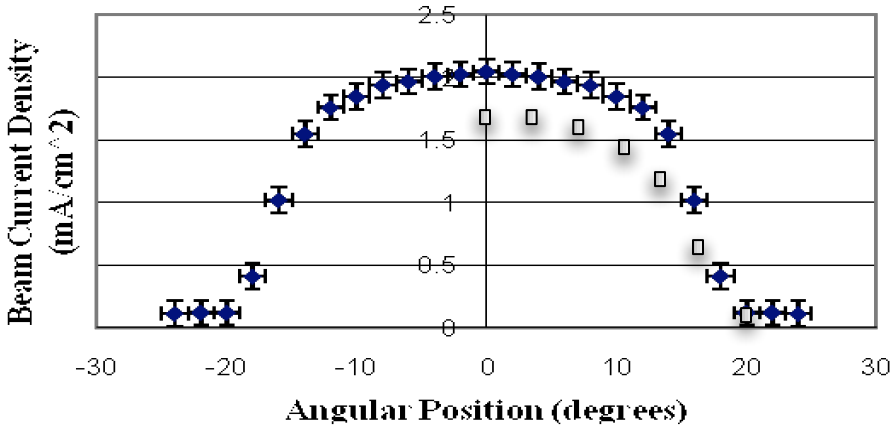

Figure 5.20. Example of measured ion beam current [58] (circles) and results of the non-local model (rectangles) for a 15-W absorbed power discharge.

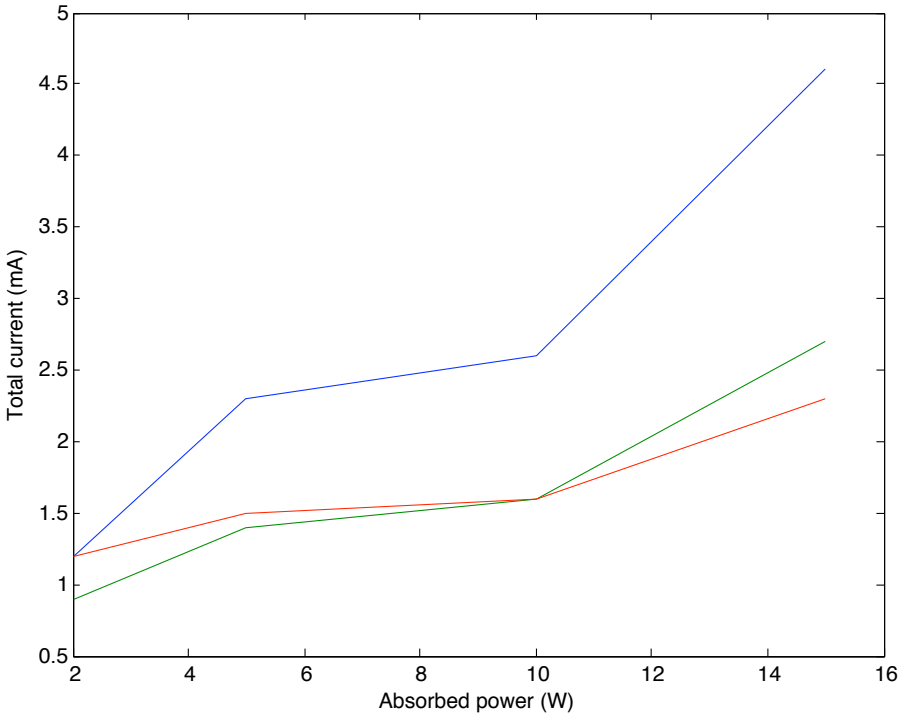

Figure 5.21. Total current as a function of absorbed power for different frequencies.

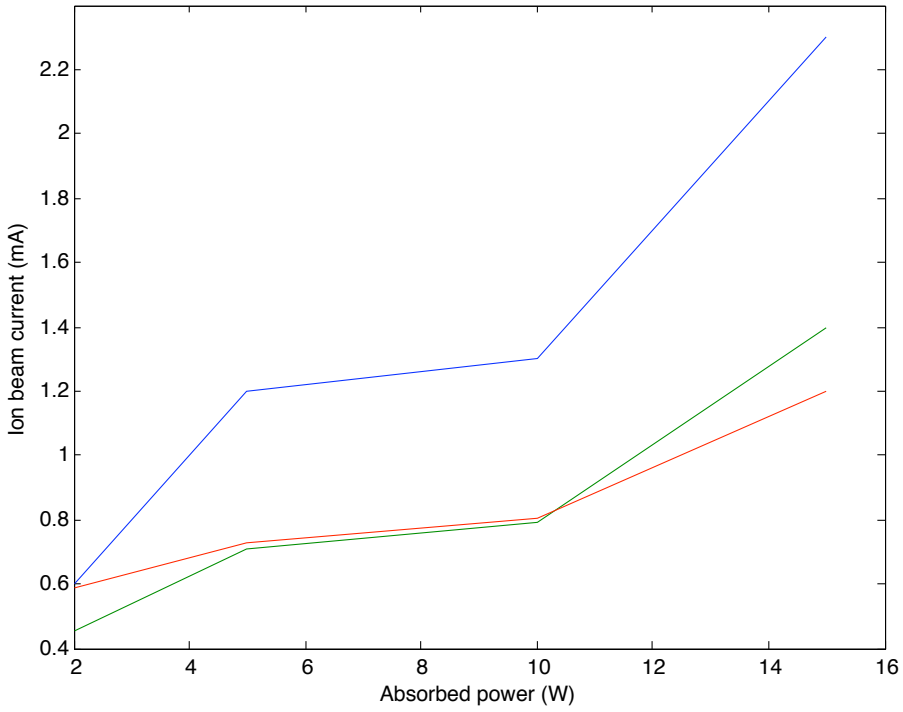

Figure 5.22. Ion beam current as a function of absorbed power for different frequencies.

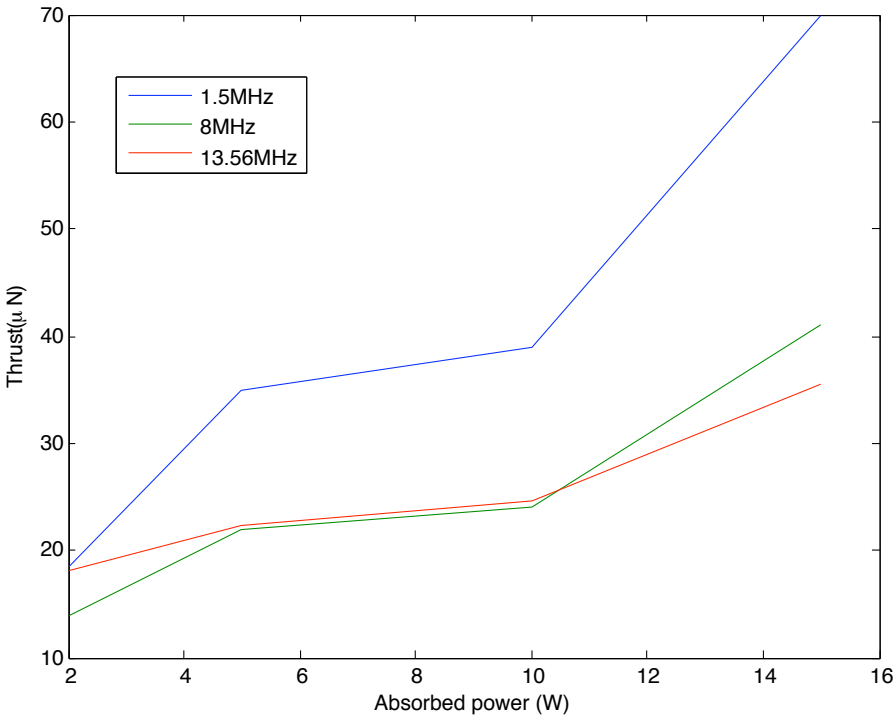

Figure 5.23. Thrust as a function of absorbed power for different frequencies with $T_s = 0.9$ and $f = 0.1$.

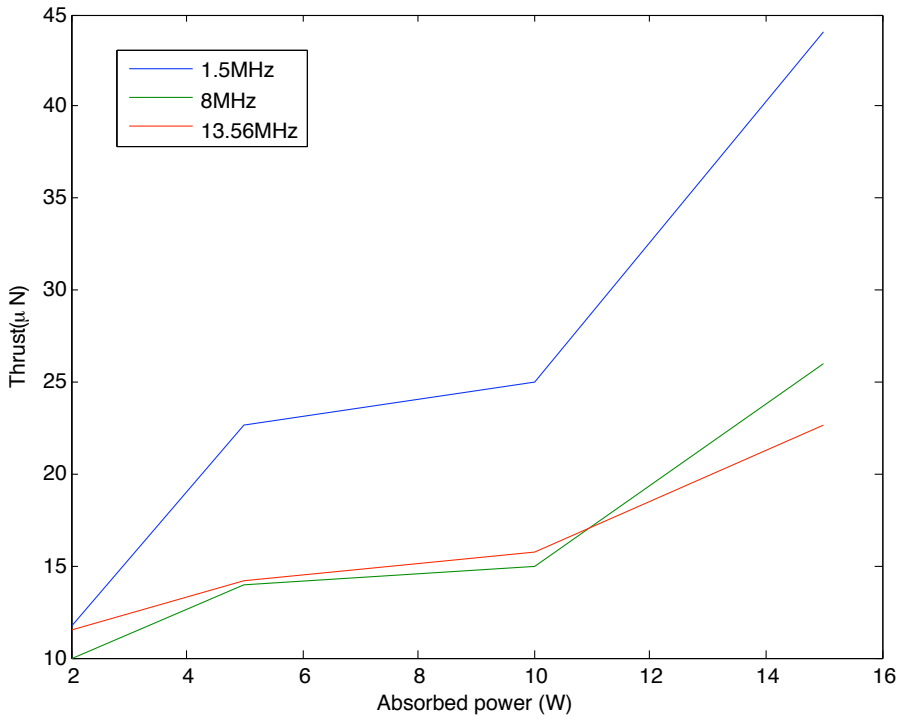

Figure 5.24. Thrust as a function of absorbed power for different frequencies with $T_s = 0.7$ and $f = 0.3$.

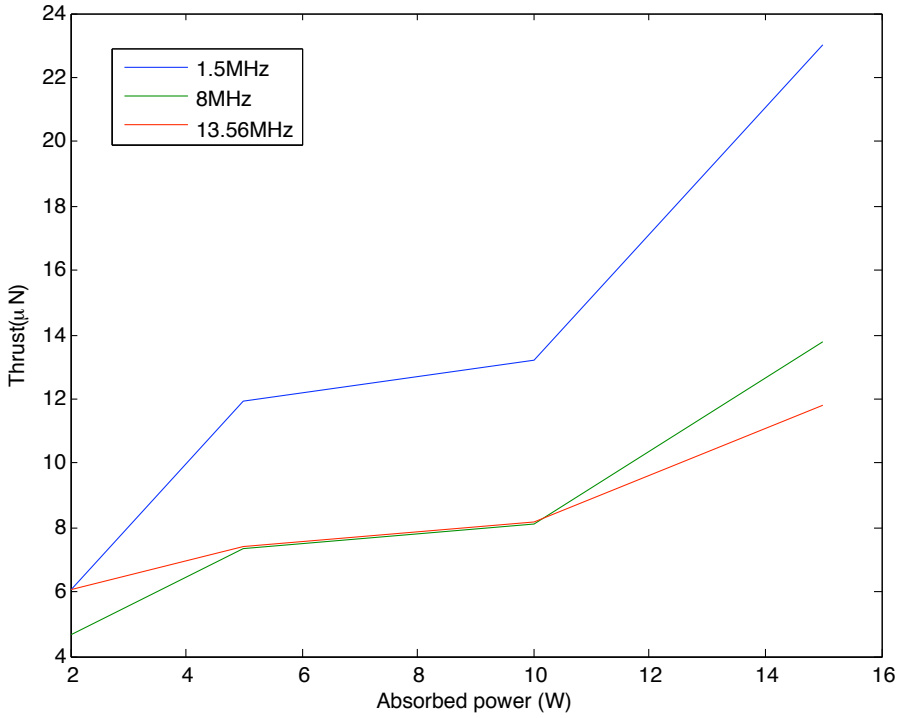

Figure 5.25. Thrust as a function of absorbed power for different frequencies with $T_s = 0.5$ and $f = 0.5$.

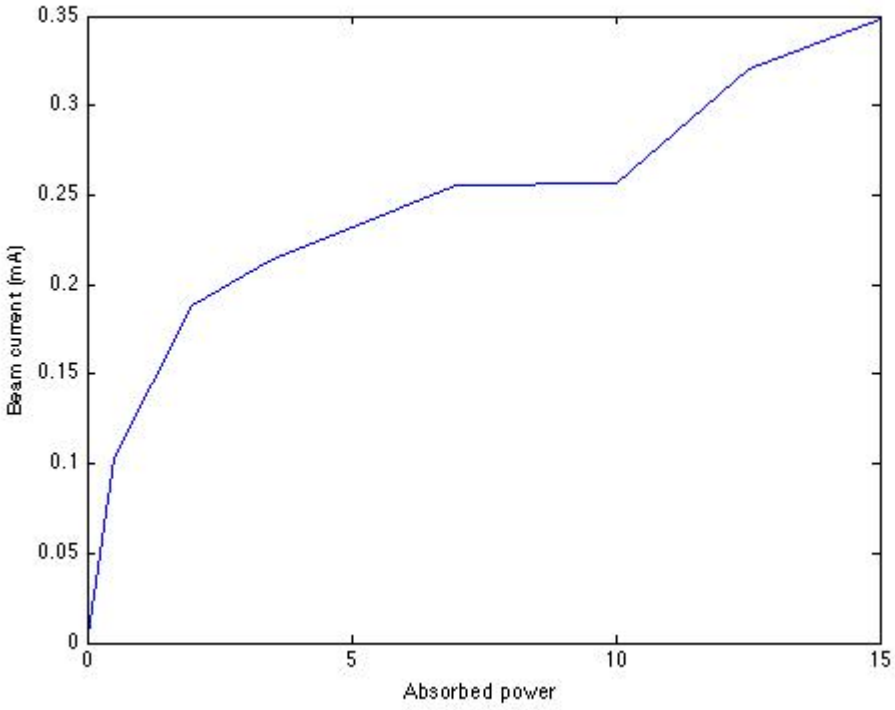

Figure 5.26. Ion beam for a 13.56-MHz discharge in the MRIT as a function of absorbed power.

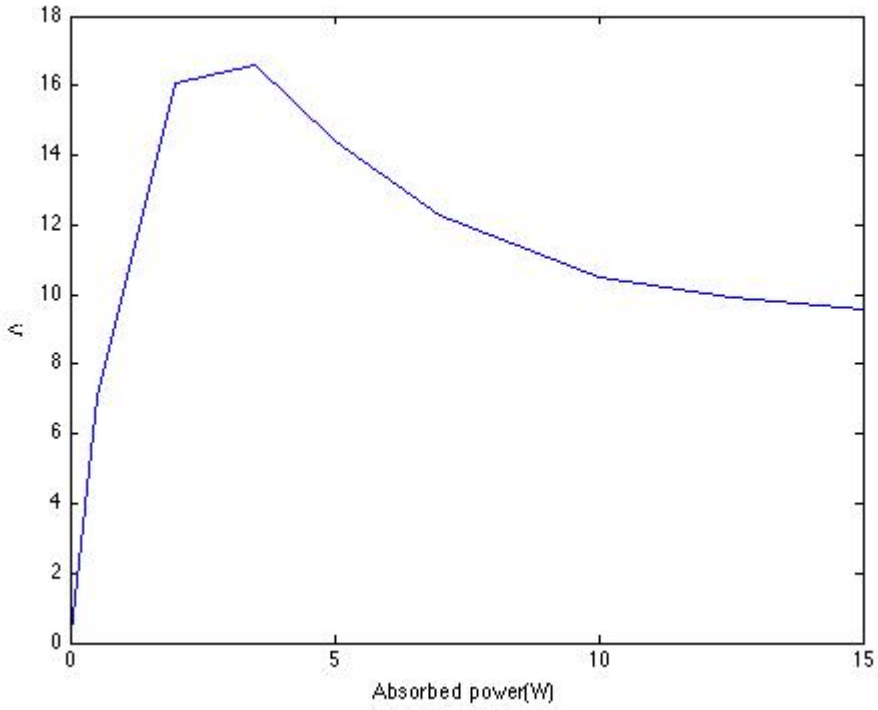

Figure 5.27. Ion beam for a 13.56-MHz discharge in the MRIT as a function of absorbed power.

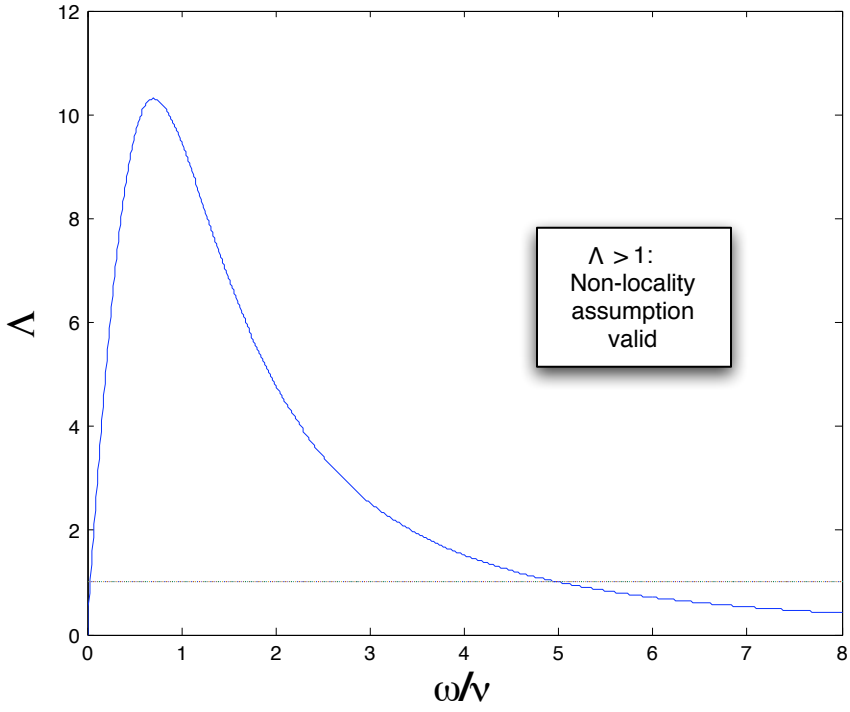

Figure 5.28. Non-locality parameter derived for the RIT-1 geometry.

Using the input data from Table 5.1 relative to the RIT-1, the non-locality parameter is found to be equal to 7.5, which makes the non-locality effects in the RIT-1 non-negligible. The derivated thrust from the non-local kinetic model is approximately 1.5 µN, which is much lower than their predicted thrust. It is to be noticed that this result from the non-locality model is for an absorbed power of 2.15 W. The power used in the MRIT is higher, 10 W, as is the number of turns of the ionization coil (4 for the MRIT). Also, the extraction grid diameter of the RIT-1 is smaller than the one of the MRIT. All of these differences contribute to the fact that, even if the RIT-1 uses xenon gas, which has a larger mass than argon, the MRIT produces more thrust (from our nonlocal calculations and experimental measurements) than the non-local simulation results of the RIT-1.

5.6 Summary

The main accomplishments presented in this chapter are the following:

- An estimate of the transition density between capacitive and inductive discharge allowing the determination of whether or not the MRIT is functioning as an inductive or capacitive discharge;
- The transformer model, applicable in the inductive coupling mode, which provides us with the various plasma parameters as a function of the absorbed power. It also allows a first estimate of thrust output as a function of power;
- The use of a self-consistent kinetic model to describe a miniature rf inductive discharge to describe the low-pressure discharge mode in the MRIT;
- The estimate of the current exiting the ionization chamber; and

- The derivation of the produced thrust by the MRIT for different input parameters.

Chapter 6

Conclusion

6.1 Contributions and Implications

Even at such small scale and large skin depth, it is possible to operate an inductive coil discharge in inductive mode. One of the initial worries was that such a discharge might only operate in E-mode; however, this work shows that the H-mode can be achieved. Results of the non-local model of the discharge in the MRIT presented here are consistent with the limited experimental data available. The MRIT was shown to be more efficient, in terms of thrust production, at a 1.5-MHz discharge frequency than at 13.56 MHz. This was also shown to be the case experimentally. The first estimates of thrust employing the local approach results in much higher values than the ones encountered experimentally and calculated with the kinetic model, which shows the necessity of taking non-locality effects into account at such small scales. The model presented here can be further used as guidance for the study of small scale cylindrical inductive discharges, in particular, for space propulsion applications.

We present here a solid basis for further numerical analysis of thruster behavior.

However, our modeling contains two main limitations, which are the following:

- the fact that we consider only the radial dimension, the effects of the very short length of the thruster therefore are not investigated;
- we assume that the electrons follow a Maxwellian distribution, which at lower pressures tends not to be the case.

6.2 Directions for Future Work

As future steps, we recommend that, still employing a 1-D description, a non-Maxwellian EVDF be derived from which new E and B fields, current densities, and thrust can be recalculated. Then, this model should be expanded to a 2-D model to further analyze the impact of the short size on the field distribution and the ion production within the plasma. Using previously developed ion optics models [12], the screen transparency should also be calculated.

In terms of experimental work, in order to further ground this model for future thruster designs and thrust production predictions, we recommend that more tests and measurements be performed on the MRIT:

- at different frequencies, in order to experimentally derive the most efficient one;
- at different applied powers, once an optimum frequency is determined; and
- again at different frequencies with the optimum power derived, until convergence, i.e., both optimum frequency and power are found.

The MRIT numerical model should be evaluated against the new experimental conditions to ascertain its efficiency.

6.3 Summary of Results

For a discharge chamber of the dimensions equal to those of the MRIT, a method to evaluate the collisional regimes as a function of pressure and frequency is presented. In the transition analysis, the conditions under which the E-to-H and H-to-E transitions occur are derived as a function of electron density. The knowledge of the conditions of existence of the various coupling modes allows us, as shown in Chapter 5, to interpret the MRIT functioning modes. The transformer model, applicable in the inductive coupling mode, provides us with the various plasma parameters as a function of the absorbed power. It also allows a first estimate of thrust output as a function of power (as described in Chapter 5). For low-pressure discharge applications, we developed a self-consistent kinetic model to describe a miniature rf inductive discharge for different collisional regimes. The calculation of the current exiting the ionization chamber allows the determination of the thrust produced by the MRIT from the current calculations shown in Chapter 5. This model can be further applied to different experimental conditions (thruster dimensions, rf frequency, coil current, etc.) to help establish the most efficient configuration, in terms of thrust production, for the MRIT.

Bibliography

[1] Loeb, H. W., Feili, D., Schartner, K. H., Weis, S., and Meyer, B. K., *Development of RIT-microthrusters*, IAC-04-S.4.04, 2005.

[2] Mistoco, V. F., Siegel, R. D., Surrusco, B. S., Mendoza, E., and Bilén, S. G.,"Design of the Local Ionospheric Measurements Satellite," 17th Annual AIAA/Utah State University Conference on Small Satellites, 11–14 August 2003.

[3] Groh, K. H., and Loeb, H. W., "State of the Art of Radiofrequency Ion Sources for Space Propulsion," *Review of Scientific Instruments*, Vol. 65, No. 5, p. 1741, May 1994.

[4] Cross, M. F., "Results from Numerical Modelling of RF Ion Thrusters," AIAA-2000-3274, 2000.

[5] Kumar, H., and Roy, S.,"Two-dimensional Fluid Model of DC and RF Plasma Discharges in Magnetic Field," 36th AIAA Plasmadynamics and Lasers Conference, Toronto, Ontario, Canada, 6–9 June 2005.

[6] Lieberman, M. A., and Lichtenberg, A. J., *Principles of Plasma Discharges and Materials Processing*, Wiley Interscience, Second Edition, 2005.

[7] Kortshagen, U., Pukropski, I., and Tsendin, L. D., "Experimental Investigation and Fast Two-Dimensional Self-Consistent Modeling of a Low-Pressure Inductively Coupled Rf Discharge," *Physical Review E*, Vol. 51, No. 5, p. 6063, 1995.

[8] Kaganovich, I. D., and Polomarov, O., "Self-Consistent System of Equations for a Kinetic Description of the Low-Pressure Discharges Accounting for the Nonlocal and Collisionless Electron Dynamics," *Physical Review E*, Vol. 68, No. 2, p. 6411, 2003.

[9] Jahn, R. G., *Physics of Electric Propulsion*, McGraw-Hill Series in Missile and Space Technology, 1968.

[10] Sutton, G. P., and Biblarz, O., *Rocket Propulsion Elements*, John Wiley & Sons Inc., 2001.

[11] Choueiri, E. Y., "A Critical History of Electric Propulsion: The First 50 Years (1906–1956)," *Journal of Propulsion and Power*, Vol. 20, No. 2, p. 193, March–April 2004.

[12] Goebel, D. H., and Katz, I., *Fundamentals of Electric Propulsion: Ion and Hall Thrusters*, JPL Space Science and Technology Series, 2008.

[13] `http://meyweb.physik.uni-giessen.de/rit/bilder/rits/big/rit10_hg1.jpg`

[14] `http://www.wtec.org/loyola/satcom/c2_s5a.htm`

[15] Leiter, H. J., Loeb, H. W., and Schartner, K. H.,"The RIT-15 Ion Engines: A Survey of the Present State of Radio Frequency Ion Thruster Technology and Its Future Potentiality," International Electric Propulsion Conference, September 7, 2000.

[16] Leiter, H. J., Killinger, R., Bassner, H., Muller, J., Kukies, R., and Frohlic, T., "Evaluation of the Performance of the Advanced 200 mN Radio Frequency Ion Thruster RIT-XT," AIAA-2002-3836, 38th AIAA/ASME/SAE/ASEE Joint Propulsion Conference and Exhibit, Indianapolis, Indiana, 2002.

[17] Killinger, R., Bassner, H., Muller, J., Kukies, R., Leiter, H. J., "High Performance RF-Ion Thruster Development (RIT XT): Performance and Durability Test Results," AIAA 2001-3488, 37th AIAA/ASME/SAE/ASEE Joint Propulsion Conference and Exhibit, Salt Lake City, Utah, 2001.

[18] Leiter, H. J., "RIT-15: A Radio Frequency Ion Thruster Engine for High Specific Impulse Operation,"AIAA-2001-3491, 37th AIAA/ASME/SAE/ASEE Joint Propulsion Conference and Exhibit, Salt Lake City, Utah, 2001.

[19] Thompson, J. J.,"The Electrodeless Ring Discharge," *Phil. Mag.*, Vol. 4, p. 1128, 1927.

[20] Eckert, H. U., "Diffusion Theory of the Electrodeless Ring Discharge," *Journal of Applied Physics*, Vol. 33, No. 9, p. 2780, Sept. 1962.

[21] Chandrakar, K., "The Starting Mechanism of the First Stage of the Ring Discharge," *Proc. of the Royal Society of London, Series A, Math. and Phys. Sciences*, Vol. 284, No. 1398, p. 442, Mar. 1965.

[22] Lister, G. G., and Cox, M., "Modelling of Inductively Coupled Discharges with Internal and External Coils," *Plasma Sources Sci. Technol.*, Vol. 1, p. 67, 1992.

[23] Gudmunsson, J .T., and Lieberman, M. A.,"Magnetic Induction and Plasma Impedance in a Cylindrical Inductive Discharge," *Plasma Sources Sci. Technol.*, Vol. 6, p. 540, 1997.

[24] Piejak, R. B., Godyak, V. A., and Alexandrovich, B. M., "A Simple Analysis of an Rf Inductive Discharge," *Plasma Sources Sci. Technol.*, Vol. 1, p. 179, 1992.

[25] Boulos, M. I., "The Inductively Coupled R.F. (Radio Frequency) Plasma," *Pure and Applied Chem.*, Vol. 57, No. 9, p. 1321, 1985.

[26] Mostaghini, J., and Boulos, M. I., "Two-Dimensional Electromagnetic Field Effects in Induction Plasma Modelling," *Plasma Chem. and Plasma Proc.*, Vol. 9, No. 1, p. 25, 1989.

[27] Hopwood, J., "Review of Inductively Coupled Plasmas for Plasma Processing," *Plasma Sources Sci. Technol.*, Vol. 1, p. 109, 1992.

[28] Yin, Y., Messier, J., and Hopwood, J., "Miniaturization of Inductively Coupled Plasma Sources," *IEEE Transactions on Plasma Science*, Vol. 27, No. 25, p. 1516, Oct. 1999.

[29] Chandrakar, K.,"The Transition from the First to the Second Stage of the Ring Discharge," *Journal Phys. D: Appl. Phys.*, Vol. 11, p. 1809, 1978.

[30] Turner, M. M., and Lieberman, M. A., "Hysteresis and the E-to-H transition in Radio-Frequency Inductive Discharges," *Plasma Sources Sci. Technol.*, Vol. 8, p. 313, 1999.

[31] Kortshagen, U., Gibson, N. D., and Lawler, J. E., "On the E-H Mode Transition in RF Inductive Discharges," *Journal Phys. D: Appl. Phys.*, Vol. 29, p. 1224, 1996.

[32] Miyoshi, Y., Petrovic, Z. L., and Makabe, T., "Transition Between Capacitive and Inductive Mode in Inductively Coupled Plasma Observed by Emission Computerized Tomography," *IEEE Transactions on Plasma Science*, Vol. 30, No. 1, p. 130, Feb. 2002.

[33] Ostrikov, K., Tsakadze, E., Ning, J., Tsakadze, Z., Jidong, L., Storer, R., and Xu, S.,"Dynamics of Mode Transitions in Inductively-Coupled Plasmas," *IEEE Transactions on Plasma Science*, Vol. 30, No. 1, p. 128, Feb. 2002.

[34] Czerwiec, T., and Graves, D. B.,"Mode Transitions in Low Pressure Rare Gas Cylindrical ICP Discharge Studied by Optical Emission Spectroscopy," *J. Phys. D: Appl. Phys.*, Vol. 37, p. 2827, 2004.

[35] Amorim, J., Maciel, H. S., and Sudano, J. P., "High-Density Plasma Mode of an Inductively Coupled Radio-Frequency Discharge," *J. Vac. Sci. Technol. B*, Vol. 9, No. 2, Apr .1991.

[36] Razzak, M. A., Kondo, K., Uesugi, Y., Ohno, N., and Takamura, S., "Transition from Electrostatic-to-Electromagnetic Mode in a Radio-Frequency Ar Inductively Coupled Plasma in Atmospheric Pressure," *Journal of Applied Physics*, Vol. 95, No. 2, p. 427, Jan. 2004.

[37] Razzak, M. A., Takamura, S., and Uesugi, Y.,"Dynamics of E-H Mode Transition in High-Pressure RF Inductively Coupled Plasmas," *IEEE Transactions on Plasma Science*, Vol. 33, No. 2, p. 284, Apr. 2005.

[38] Brophy, J. R., Katz, I., Polk, J. E., and Anderson, J. R., "Numerical Simulations of Ion Thruster Accelerator Grid Erosion," AIAA Paper 2002-4261, 38th Joint Propulsion Conference, July 7–10, 2002.

[39] Whealton, J. H., McGaffey, R. W., and Meszaros, P. S., "A Finite Difference 3-D Poisson-Vlasov Algorithm for Ions Extracted from a Plasma," *Journal of Computational Physics*, Vol. 63, p. 20, 1986.

[40] Arakawa, Y., and Nakano, M., "An Efficient Three Dimensional Optics Code for Ion Thruster Research," AIAA-96-3198, 32nd Joint Propulsion Conference, Lake Buena Vista, Florida, July 1–3, 1996.

[41] Farnell, C. C., Williams, J. D., and Wilbur, P. J.,"Numerical Simulation of Ion Thruster Optics," NASA/CR–2003–212305, 2003.

[42] Nakayama, Y., and Wilbur, P., "Numerical Simulation of High Specific Impulse Ion Thruster Optics," IEPC-01-099, 27th International Electric Propulsion Conference, Pasadena, California, October 15–19, 2001.

[43] Nakano, M., and Arakawa, Y., "Ion Thruster Lifetime Estimation and Modeling Using Computer Simulation," IEPC-99-145, 27th International Electric Propulsion Conference, Pasadena, California, October 15–19, 2001.

[44] Boyd, I., and Crofton, M., "Grid Erosion Analysis of the T5 Ion Thruster," AIAA-2001-3781, 37th Joint Propulsion Conference, Salt Lake City, Utah, July 8–11, 2001.

[45] Okawa, Y., Takegahara, H., and Tachibana, T., "Numerical Analysis of Ion Beam Extraction Phenomena in an Ion Thruster," IEPC-01-097, 27th International Electric Propulsion Conference, Pasadena, California, October 15–19, 2001.

[46] Wang, J., Polk, J. E., Brophy, J. R., and Katz, I., "Three-Dimensional Particle Simulations of NSTAR Ion Optics," IEPC-01-085, 27th International Electric Propulsion Conference, Pasadena, California, October 15–19, 2001.

[47] Anderson, J. J., Katz, I., and Goebel, D., "Numerical Simulation of Two-Grid Ion Optics Using a 3D Code," AIAA-2004-3782, 40th Joint Propulsion Conference, Ft. Lauderdale, Florida, July 11–14, 2004.

[48] El Fayoumi, M., Jonesy, I. R., and Turner, M. M., "Hysteresis in the E- to-H Mode Transition in a Planar Coil, Inductively Coupled Rf Argon Discharge," *J. Phys. D: Appl. Phys.*, Vol. 31, p. 3082, 1998.

[49] Godyak, V., Piejak, R. B., Alexandrovich, B. M., and Kolobov, V. I., "Experimental Evidence of Collisionless Power Absorption in Inductively Coupled Plasmas," *Phys. Rev. Lett.*, Vol. 80, p. 3264, 1998.

[50] Kolobov, V. I., and Godyak, V. A., "Nonlocal Electron Heating Kinetics in Collisional Gas Discharge Plasma," *IEEE Transactions Plasma Science*, Vol. 23, No. 4, p. 503, Aug. 1995.

[51] Kolobov, V. I., and Economou, D. J.,"The Anomalous Skin Effect in Gas Discharge Plasmas," *Plasma Sources Sci. Technol.*, Vol. 6, R1, 1997.

[52] Godyak, V., "Plasma Phenomena in Inductive Discharges," *Plasma Phys. Control Fusion*, Vol. 45, p. A399, 2003.

[53] Godyak, V., and Sternberg, N.,"Smooth Plasma-Sheath Transition in a Hydrodynamic Model," *IEEE Transactions on Plasma Science*, Vol. 18. No. 1, p. 159, Feb. 1990.

[54] Kim, D., and Economou, D. J., "Simulation of a Two-Dimensional Sheath over a Flat Wall with an Insulator/Conductor Interface Exposed to a High Density Plasma," *Journal of Applied Physics*, Vol. 94, No. 5, p. 2852, 2003.

[55] Miller, P. A., and Riley, M. E., "Dynamics of Collisionless Rf Plasma Sheaths," *J. Appl. Phys.*, Vol. 82, No. 8, p. 3689, Oct. 1997.

[56] Nitschke, T. E., and Graves, D. B., "Matching an RF Sheath Model to a Bulk Plasma Model," *IEEE Transactions on Plasma Science*, Vol. 23, No. 4, p. 717, Aug. 1995.

[57] Trudel, T. A., Bilén, S. G., and Micci, M. M., "Design and Performance Testing of a 1-cm Miniature Radio Frequency Ion Thruster," 31st International Electric Propulsion Conference, IEPC 2009-167, Ann Arbor, Michigan, USA, Sept. 20–24, 2009.

[58] Trudel, T. A., Bilén, S. G., and Micci, M. M., "Design and Performance Testing of a 1-cm Miniature Radio-Frequency Ion Thruster," submitted to *J. Prop. Power*, 2011.

[59] MacKinnon, K. A., "On the Origin of the Electrodeless Discharge," *Phil.. Mag.*, Vol. 8, p. 605, 1929.

[60] Frost, L. S., and Phelps, A. V., "Momentum-Transfer Cross Sections for Slow Electrons in He, Ar, Kr, and Xe from Transport Coefficients," *Phys. Rev.*,Vol. 136, p. A1538, 1964.

[61] Koizumi, T., Shirakawa, E., and Ogawa, I., "Momentum Transfer Cross Sections for Low-Energy Electrons in Krypton and Xenon from Characteristic Energies," *J. Phys. B: At. Mol. Phys.*, Vol. 19, p. 233, 1986.

[62] Hayashi, M., "Determination of Electron-Xenon Total Excitation Cross-Sections, from Threshold to 100 eV, from Experimental Values of Townsend's α," *J. Phys. D: Appl. Phys.*, Vol. 16, p. 581, 1983.

[63] Vahedi, V., "Modeling and Simulation of Rf Discharges used for Plasma Processing," Ph. D.Thesis, University of California, Berkeley, 1993.

[64] Berstein, I. B., and Holstein, T., "Electron Energy Distribution in Stationary Discharges," *Phys. Rev.*, Vol. 94, No. 6, p. 1475, June 1954.

[65] Tsendin, L. D., "Electron Energy Distribution in Transversely Inhomogeneous Current-Carrying Plasma," *Sov. Phys. JETP*, Vol. 39, p. 805, 1974.

[66] Lee, M. H., and Chung, C.-W., "On the E to H and H to E Transition Mechanisms in Inductively Coupled Plasma," *Physics of Plasmas*, Vol. 13, 063510, 2006.

[67] Ramamurthi, B., Economou, D. J., and Kaganovich, I. D., "Effect of Electron Energy Distribution Function on Power Deposition and Plasma Density in an Inductively Coupled Discharge at Very Low Pressures," *Plasma Sources Sci. Technol.*, Vol. 12, p. 302, 2003.

[68] Stiel, L. I., and Thodos, G., "The Viscosity of Nonpolar Gases at Normal Pressures," *Am. Inst. Chem. Eng. J.*, Vol. 7, p. 611, 1961.

[69] Auday, G., Guillot, P., Galy, J., and Brunet, H., "Experimental Study of the Effective Secondary Emission Coefficient for Rare Gases and Copper Electrodes," *J. Appl. Phys.*, Vol. 83, No. 11, p. 5917, 1988.

[70] Kruithof, A. A., "Townsend's Ionization Coefficients for Neon, Argon, Krypton and Xenon," *Physica VII*, Vol. 7, No. 6, p. 519, June 1940.

[71] Fairchild, M., *Radio Frequency Ion Microthruster Chamber Development*, M.S. Thesis, The Pennsylvania State University, 2003.

[72] Huetz, A., Selles, P., Waymel, D., and Mazeau, J., "Wannier Theory for Double Photoionization of Noble Gases," *J. Phys. B: At. Mol. Opt. Phys.*, Vol. 24, p. 1917, 1991.

[73] Rapp, D., and Englander-Golden, P.,"Total Cross Section for Ionization and Attachment in Gases by Electron Impact," *The Journal of Chemical Physics*, Vol. 43, No. 5, p. 1464, September 1965.

[74] Roy, S., "Flow Actuation Using Radio Frequency in Partially Ionized Collisional Plasmas," *Applied Physics Letters*, Vol. 86, 101502, 2005.

[75] Wu, Y., and Lieberman, M. A., "The Influence of Antenna Configuration and Standing Wave Effects on Density Profile in a Large-Area Inductive Plasma Source," *Plasma Sources Sci. Technol.*, Vol. 9, p. 210, 2000.

[76] Knipp, C. T., and Knipp, J. K., "Electrodeless Discharge: Method of Measuring Induced Current, Variation of Current with Pressure for Various Gases," *Physical Review*, Vol. 38, p. 948, 1931.

[77] Blevin, H. A., Reynolds, J. A., and Thonemann, P. C., "Penetration of an Electromagnetic Wave into a Hot Plasma Slab," *The Physics of Fluids*, Vol. 13, No. 5, p. 1259, May 1970.

[78] Cubbin, E. A., Ziemer, J. K., Choueiri, E. Y., and Jahn, R. G., "Pulsed Thrust Measurements Using Laser Interferometry," AIAA-1996-2985, 1996.

[79] Jamison, A. J., Ketsdever, A. D., and Muntz, E. P., "Gas Dynamic Calibration of a Nano-Newton Thrust Stand," *Review of Scientific Instruments*, Vol. 73, No. 10, p. 3629, Oct. 1992.

[80] Ketsdever, A. D., "Facility Effects on Performance Measurements of Micropropulsion Systems that Utilize Gas Expansion," *Journal of Propulsion and Power*, Vol. 18, No. 4, p. 797, July–August 2002.

[81] Alexandrov, A. F., Bogdankevich, L. S., and Rukhadze, A. A., *Principles of Plasma Electrodynamics*, Springer Series in Electrophysics, 1984.

[82] Raizer, Y. P., *Gas Discharges Physics*, Springer, 1991.

[83] Wu, H.-M., Yu, B. W., Li , M., and Yang, Y., "Two-Dimensional Fluid Model Simulation of Bell Jar Top Inductively Coupled Plasma," *IEEE Transactions on Plasma Science*, Vol. 25, No. 1, p. 1, 1997.

[84] Kortshagen, U., Puproski, I., and Tsendin, L. D., "Experimental Investigation and Fast 2-Dimensional Self-Consistent Kinetic Modeling of a Low Pressure Inductively Coupled RF-Discharge," *Phys. Rev. E*, Vol. 51, No. 6, p. 6063, 1995.

[85] Smolyakov, A., Godyak, V., and Duffy, A., "On Nonlinear Effects in ICPs," *Physics of Plasmas*, Vol. 7, No. 11, p. 4755, 2000.

[86] Wirz, R., Gale, M., Mueller, J., and Marrese, S., "Miniature Ion thrusters for Precision Formation Flying," AIAA–4115, 40$^{\text{th}}$ AIAA/ASME/SAE/ASEE Joint Propulsion Conference and Exhibit, 11–14 July 2004, Fort Lauderdale, FL.

[87] Wirz, R., Polk, J., Marrese, C., and Mueller, J., "Experimental and Computational Investigation of the Performance of a Micro-Ion Thruster," AIAA-2002–3835, 38$^{\text{th}}$ AIAA/ASME/SAE/ASEE, Joint Propulsion Conference, 7–10 July 2002, Indianapolis, IN.

[88] Lieberman, M. A., "Spherical Shell Model of an Asymmetric RF Discharge," *J. Appl. Phys.*, Vol. 65, No. 11, p. 4186, 1989.

[89] Kawamura, E., Vahedi, V., Lieberman, M. A., and Birdsall, C. K., "Ion Energy Distributions in Rf Sheaths; Review, Analysis and Simulation," *Plasma Sources Sci. Technol.*, Vol. 8, R45, 1999.

[90] Haas, F. A., and Braithwaite, N. S. J., "Simple Analysis of a Capacitive Discharge with a Bi-Maxwellian Electron Distribution," *Plasma Sources Sci. Technol.*, Vol. 9, No. 1, p. 77, 2000.

[91] Sommerer, T. J., Hitchon, W. N. G., Harvey, R. E. P., and Lawler, J. E., "Self-Consistent Kinetic Calculations of Helium RF Glow Discharges," *Phys. Rev. A*, Vol. 43, p. 4452, 1991.

[92] Surendra, M., and Graves, D., "Particle Simulations of Radio-Frequency Glow Discharges," *IEEE Trans. Plasma Science*, Vol. 19, No. 2, p. 144, 1991.

[93] Yan, M., and Goedheer, W. J., "A PIC-MC Simulation of the Effect of Frequency on the Characteristics of VHF SiH_4/H_2 Discharges," *Plasma Sources Sci. Technol.*, Vol. 8, p. 349, 1999.

[94] Boeuf, J. P., and Pitchford, L., "Two-Dimensional Model of a Capacitively Coupled Rf Discharge and Comparisons with Experiments in the Gaseous Electronics Conference Reference Reactor," *Phys. Rev. E*, Vol. 51, p. 1376, 1995.

[95] Young, F. F., and Wu, C. H., "Two-dimensional, Self-Consistent, Three-Moment Simulation of RF Glow Discharge," *IEEE Trans. Plasma Sci.*, Vol. 21, No. 3, p. 312, 1993.

[96] Gogolides, E., and Sawin, H., "Continuum Modeling of Radio-Frequency Glow Discharges. I. Theory and Results for Electropositive and Electronegative Gases," *J. Appl. Phys.*, Vol. 72, p. 3971, 1992.

[97] Sommerer, T. J., and Kushner, M. J., "Numerical Investigation of the Kinetics and Chemistry of Rf Glow Discharge Plasmas Sustained in He, N_2, O_2, $He/N_2/O_2$, $He/CF_4/O_2$, and SiH_4/NH_3 using a Monte Carlo Fluid Hybrid Model," *J. Appl. Phys.*, Vol. 71, p. 1654, 1992.

[98] Sommerer, T. J., and Kushner, M. J., "Monte Carlo Fluid Model of Chlorine Atom Production in Cl_2, HCl, and CCl_4 Radio-Frequency Discharges for Plasma Etching," *J. Vac. Sci. Technol. B*, Vol. 10, p. 2179, 1992.

[99] Ventzek, P. L. G., Grapperhaus, M., and Kushner, M. J., "Investigation of Electron Source and Ion Flux Uniformity in High Plasma Density Inductively Coupled Etching Tools Using Two-Dimensional Modeling," *J. Vac. Sci. Technol. B*, Vol. 12, p. 3118, 1995.

Vita

Valérie F. M. Mistoco

Valérie Mistoco was born in Les Abymes in Guadeloupe in 1979. After passing the French Baccaulaureat in Science with honors in 1996 and receiving the Prize of Excellence in Guadeloupe, she entered the Classes Préparatoires aux Grandes Écoles in Chartres, France, in September 1996. In September 2001, she graduated with a Master's degree in Physics from the University of Orléans, France. She worked as a research assistant on a pulsed detonation engine from February 2002 to August 2002 at the Propulsion Engineering Research Center (PERC) at the Pennsylvania State University. She received a preparatory degree for doctoral studies (diplome d'études approffondies) in Physics, Atmosphere and Plasma from the University of Orléans in September 2002. She served as a student project manager, deputy student project manager and propulsion engineer student lead on the Penn State student satellite project LionSat from February 2003 to July 2006. In August 2003 she started a doctoral in Electrical Engineering at Penn State University under the direction of Prof. Sven Bilén. Valérie is a member of the American Institute of Aeronautics and Astronatutics (AIAA) and the Institute of Electrical and Electronics Engineers (IEEE).